VISUALIZING WELLBORE INSTABILITY AND FRACTURE DIRECTION BY APPLICATION OF PRINCIPAL STRESS TRAJECTORY ANALYSIS

A Thesis

by

NED C THOMAS

Submitted to the Office of Graduate and Professional Studies of
Texas A&M University
in partial fulfillment of the requirements for the degree of

MASTER OF SCIENCE

Chair of Committee, Ruud Weijermars

Committee Members, Thomas Blasingame

Fred Dupriest

Head of Department, Dan Hill

August 2017

Major Subject: Petroleum Engineering

Copyright 2017 Ned Thomas

ABSTRACT

This study furthers our understanding of the causes of wellbore failure by thoroughly analyzing key properties (e.g., in-situ stress regime, formation and pore pressures, and rock properties) associated with wellbore instability. Regardless of whether a wellbore is planned to be drilled underbalanced or overbalanced, local formation pressures, and even operational practices (e.g., shutting off the pumps while drilling) can quickly render a wellbore locally unstable. Near-borehole stress mechanics associated with stress cages (overbalanced holes) and with fracture cages (underbalanced holes) are further studied, including an analysis showing the impact tangential and radial stress magnitudes have on principal stress trajectory patterns. With a deeper understanding of stress cages and fracture cages, wellbore failure can, consequently, be quantified and visually evaluated to a greater extent. Stress trajectory analytical solutions can be rapidly applied for a wide range of in-situ stress and pressure conditions, which enable us to better predict, and therefore mitigate, wellbore instabilities associate with tensional and shear failure, and also estimate more assuredly unknown parameters that drive wellbore instability. The wellbore stress model in this study accounts for different in-situ stress regimes, borehole net fluid pressures, and poroelastic effects. Drilling software equipped with these tools may help reduce the occurrence of failure, saving drillers from countless hours of non-productive time and other associated costs.

DEDICATION

I dedicate this thesis to my family, for their unwavering love and support.

ACKNOWLEDGEMENTS

I would like to thank my committee chair, Dr. Ruud Weijermars, for his patience and leadership throughout my studies. I would also like to thank my committee members, Dr. Thomas Blasingame and Mr. Fred Dupriest, for their guidance and support throughout the course of this research.

Thanks also to my friends at Texas A&M University who made my time in College Station memorable.

CONTRIBUTORS AND FUNDING SOURCES

This work was supported by a thesis committee consisting of Professors Ruud Weijermars, Thomas Blasingame, and Fred Dupriest of the Department of Petroleum Engineering.

Graduate study was sponsored by start-up funds from the Texas A&M Engineering Experiment Station (TEES) provided to Thesis adviser, Dr. R. Weijermars. The Texas Oil and Gas Institute provided well data used in this study.

No collaboration with any students took place for the work presented in this thesis.

TABLE OF CONTENTS

LIST OF FIGURES

Page

1. INTRODUCTION

Wellbore instability continues to be an important concern for the oil and gas industry. Local underbalance from unexpected high-pressure formations can lead to shear or compressive failure, resulting in breakout and potential blowout. Local overbalance of mud weight relative to formation strength leads to tensional failure and lost circulation. As wells continue to be drilled in more complex orientations and at deeper depths, particularly offshore, the monetary impact and dangers related to these challenges will compound and become increasingly important to mitigate. A greater understanding of the principal stress trajectories and related stress magnitudes around cylindrical holes in loaded rock formations significantly aids the design of safer and more stable wellbores, advances our capacities in hydraulic fracturing, and provides additional geoscientific insights into the nature and stability of volcanoes and salt domes (Thomas and Weijermars, 2017; *Submitted Earth-Science Reviews).

This study applies the adapted static analytical Kirsch (1898) equations which account for borehole net fluid pressure. The system of equations is systematically non-dimensionalized using two critical parameters to scale the variable boundary conditions: the Frac Number, F (Section 2.4), and the Bi-axial Stress Scalar, χ (Section 2.5). The Frac Number controls the net pressure in the borehole as it relates to the natural background stress in the host rock and the pressure in the penetrated formation at each depth. The Bi-axial Stress Scalar describes the local in-situ stresses at each depth and for each formation penetrated by a wellbore by describing the anisotropy of the two far-field principal

stresses. Manipulation of these two governing parameters (χ, F) enables us to view and monitor the stress trajectories in the host rock around a borehole at any given depth.

Depending on stress boundary conditions, principal stress orientations near the wellbore can alter drastically. At neutral points – regions where the two deviatoric principal stresses in the plane of view are equal in magnitude – the principal stress orientations are reversed. The neutral points and their effects on the principal stress orientations near a borehole have been more thoroughly investigated in this study. The neutral points form the boundaries for the 'stress cage' in overbalanced (F>0) boreholes, and the complementary 'fracture cage' in underbalanced (F<0) boreholes. Understanding the perturbation induced by stresses around cylindrical holes in rock formations is paramount in geotechnical analyses and stability appraisals of manmade cylindrical holes (e.g., wellbores, tunnels, storage caverns, etc.), as well as for the geoscientific interpretation of piercing by cylindrical, fluid-filled pipes.

The term 'fracture cage' (for definition, see Section 6), first introduced by Weijermars et al. (2012), is different from the term 'stress cage' (Section 5). The latter term has been used to describe the rise in tangential stresses around a wellbore due to dilation and propping of early fractures (Alberty and McLean 2004; Wang et al. 2008; Tovar and Bhat 2011). Obviously, the two mechanisms relate, but fracture cages and stress cages each require their own specific analysis. This study analyzes in greater detail the mechanisms of stress cages and fracture cages, including analysis of the distribution of radial, tangential, and principal stresses inside the caged regions, and analysis of the unique stress orientation reversals that occur during each phenomenon. Static analytical

stress solutions predict the conditions leading to fracture cages, and this phenomenon was confirmed by a separate independent study that employed an advanced dynamic numerical model (Section 4.2) to arrive at nearly identical results. This study will identify the two models—static analytical and dynamic numerical—and highlight the practical implications of both regarding prudent well management.

With a knowledge of the principal stress trajectories and magnitudes, an appropriate failure criterion can be applied which allows us to visualize the direction and severity of failure (size of breakout angle for underbalanced wells and distance of intrusion of tensile failure for overbalanced wells). For wellbores oriented in the direction of one of the principal stresses, a 2-dimensional system of failure solutions is appropriate. However, to account for deviated wellbores oblique to a principal stress direction, a 3D failure criterion is pertinent. For simplicity in first gaining a detailed understanding of the stress cage and fracture cage mechanics, deviated wellbores have not been included in this study. Additionally, the effects of stress cages and fracture cages on hydraulic fracture propagation are realized. Stress cages and fracture cages can both cause tortuosity, which remains one of the biggest challenges faced by shale and tight gas hydraulic-fracturing treatments. Tortuosities lead to high near-wellbore frictional pressure loss, premature screenouts, reduced treating rates, and poor production results (Denney). Tortuosity effects, and therefore appropriate measures to mitigate those effects, are different for the two systems of cages, however.

Poroelastic effects are summarized in Section 7. The pore pressure can alter the effective stress magnitudes by several MPa, which could prove critical in determining an

appropriate mud weight while drilling or in calculating the pressure needed to induce a fracture during completions. The pore pressure does not affect principal stress orientations, however, and so the breakout direction and angle based on slip line orientations will be unaffected by changes in pore pressure. Pore pressure changes can be due an unexpected overpressured formation, or even looking at the pressure response over the life of the reservoir as it transitions from preproduction stage to depletion. Only the far-field stress orientations, magnitudes, and the borehole net fluid pressure affects the principal stress directions.

The increase in world energy demand and recent success with unconventional reservoirs is leading to other challenges in engineering. Unconventional reservoirs often encounter complex geomechanics problems that require more and better understanding of rock mechanics, formation evaluation, and production and development strategies. The low and ultra-low permeabilities lead to the requirement of fracture stimulation in all cases. This requires understanding of pressure variations in the reservoir, as this is directly related to stresses acting on the rocks. Stress is a critical parameter for designing successful drilling and hydraulic fracturing programs and for understanding reservoir production and depletion. A geomechanical model requires a great deal of input information, including measurements of vertical and minimum stress magnitudes, pore pressures, rock properties, and drilling operational logistics, all of which are oriented to determining the magnitude and direction of maximum horizontal stress.

2. BACKGROUND AND REVIEW

A recent study (Thomas and Weijermars, 2017; *Submitted to Earth-Science Reviews) has shown that the analysis of stressed cylindrical cavities has vast application to numerous geoscientific fields (e.g., magmatic volcanoes, mud volcanoes, salt diapirs) and geotechnical fields (e.g., drilling and hydraulic fracturing operations, tunnel excavations, gas storage caverns). Many of these studies provided additional insight into the mechanisms that lead to borehole instability. The previous study focused on a general overview of stress perturbations around cylindrical formations (both geoscientific and geotechnical), and showed the overlap between each unique study, gleaning important information from each subsection that could be adapted and applied to the rest. This study intends to explore in further detail the mechanics of borehole instabilities, and in particular, the role that principal stress trajectories and magnitude concentrations play in them.

Thomas and Weijermars (2017; *Submitted to Earth-Science Reviews) summarized in depth the rationale and justification for using a static analytical modeling approach. These justifications will be briefly reiterated below (Section 2.1), followed by the basic assumptions behind the model (Section 2.2).

2.1 Rationale

The analytical Kirsch (1898) equations, introduced over a century ago, have been adapted in our study to account for bi-axial far-field stress conditions and borehole net

pressure contributions; and they have been systematically non-dimensionalized to allow for quick and easy scaling. Returning to and augmenting the analytical solutions is merited for several major reasons.

First, the closed-form solutions allow for rapid calculation of the curvilinear line-integrals which represent continuous stress trajectories. Discrete element methods would require extremely narrow grid sizing to achieve the same results as the analytical solutions. Such narrow grid-sizing makes finite-element solutions more time-consuming to produce and henceforth are costlier, while not necessarily more accurate.

Second, due to the finite grid-size, the neutral points, which are a crucial aspect of the near-wellbore stress state, have been overlooked by discrete solution methods. The non-dimensional form of the Kirsch equations used in this study can quickly locate the neutral points near a borehole. The location of these points varies with the boundary conditions.

Third, when drilling a wellbore, the magnitude and orientation of the in-situ stress field can be locally altered as the stresses redistribute due to the excavation of rock. Large stress concentrations can result from these induced stresses (see Eqs. 7a-c in Section 4.6). The approach used within this study supersedes the use of stress concentration factors by providing full spatial solutions for both the radial and tangential stress magnitudes, as well as the principal stresses in every location around the stressed borehole. The results are illustrated in stress magnitude contour maps (Sections 5 and 6), further clarified by strategically chosen cross-sections showing how the various stresses change with direction and distance from the borehole rim.

Fourth, the systematic shift of all key elements (neutral points, principal stress magnitudes, radial and tangential stress magnitudes, stress trajectories, consequent slip lines and predicted mode of imminent failure based on tensile strength and shear failure criteria) can be mapped out relatively easily when analytical expressions are used as demonstrated in this study. The full potential of the Kirsch equations has still not been utilized even in concurrent wellbore stability analysis methods, because the stress trajectories, slip lines and neutral points have all been overlooked as key elements for interpreting critical regions of failure. Therefore, emphasis is placed on the difference between overbalanced and underbalanced wellbores, which display the phenomena of stress caging and fracture caging, respectively, each having distinct modes of failure (Sections 5-6).

Fifth, Although the analytical Kirsch equations still have additional strengths that this study intends to highlight, it is also important to acknowledge the limitations of this static analytical model. First, all solutions are static and do not account for dynamic effects such as stress re-orientation upon failure. Additionally, for underbalanced wellbores, only the direction of the principal stresses can accurately be predicted based on the breakout, and accurate measurements of stress magnitudes in relation to breakout width and depth would require not only considerations of the geometrical effects and the failure mechanisms of the material but also considerations of such processes as borehole wall erosion by the drilling fluids. However, many natural applications (Thomas and Weijermars, 2017; *Submitted to Earth-Science Reviews) exist where static analysis provides excellent templates for predicting modes of failure. Additionally, a more detailed

integration of analytical and advanced numerical solutions (Weijermars et al., 2013a) provides excellent validation for the model used in this study in predicting fracture propagation and borehole instabilities, even though a static approach is used (Section 4.2).

A clever modeling strategy makes use of all principal tools available to improve our understanding of a particular physical system (Fig. 1). A conceptual model needs to be supported by a computational model that simulates the natural process using a combination of analytical and numerical methods (Winsberg, 2001; Frigg and Hartmann, 2009) – geomechanical studies are no exception. The most accurate results are achieved by combining the mutual strengths of each method. The static analytical solutions, which occupy a fundamental place in the modeling procedure (Fig. 1), are employed in this study, showing how such models can explain a variety of field observations and provide estimates of native stress conditions. The left half of Figure 1 (green box) covers static solutions which commonly have a wide generic application field (this study), and the right half (red box) represents advanced dynamic studies commonly developed for projects with a specific scope and tolerance. In all geomechanical models, the material properties of rocks measured in the laboratory under controlled initial state and boundary conditions are indispensable (Section 9). Integration of all nodes of the modeling strategy will prompt for improvement of the conceptual model and corresponding adjustments to the mathematical formulation.

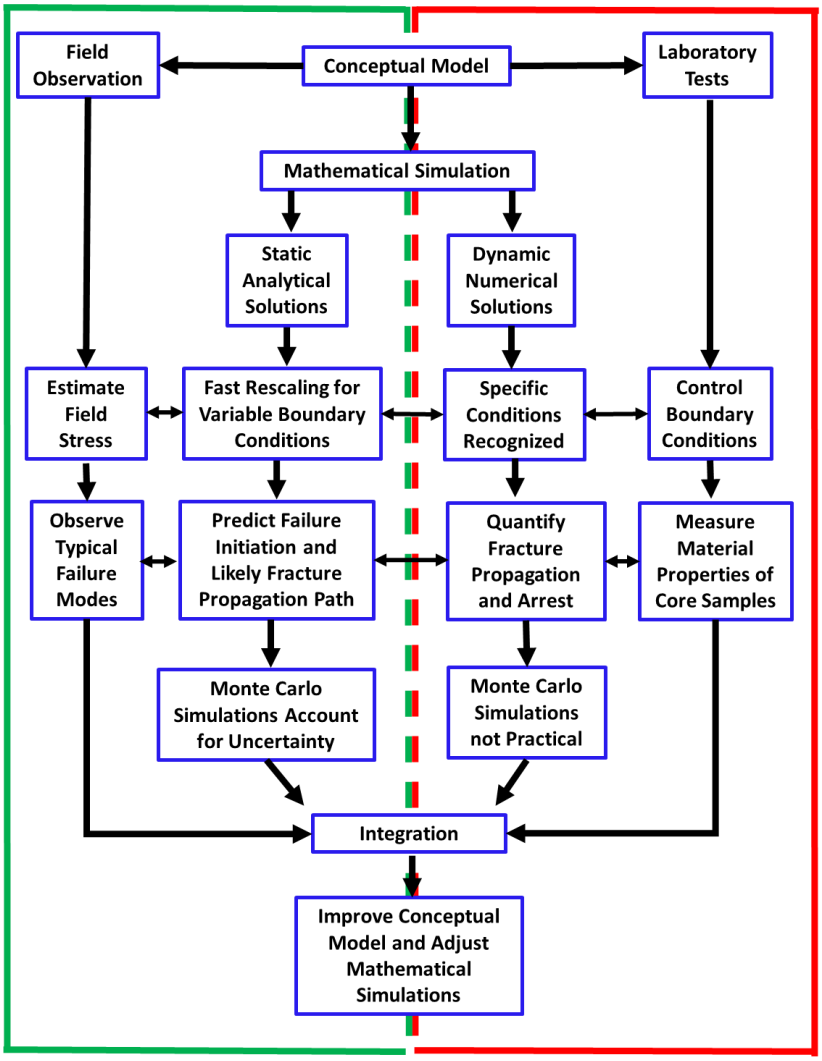

Figure 1: The physical process of failure around a cylindrical rock cavity can be studied by integrating into a workflow the observations and measurements from field operations, laboratory tests, and mathematical simulations (both static and dynamic) to improve the conceptual model for stability and failure analysis. Our study provides an improved, generalized analytical model of static stress quantification and predicts the likely failure locations and failure modes based on simple 2D failure criteria with scalable boundary conditions.

2.2 Fundamental assumptions

Throughout this study, total stress is denoted as σ and deviatoric stress as τ. Deviatoric stresses differ from the total stress in that isotropic stresses (pressure components) cause volumetric deformation in isotropic material and deviatoric stresses cause shape deformation. The deviatoric stresses around a wellbore result from the dynamic superposition of (1) far-field tectonic stress, (2) near-wellbore stress due to lithostatic pressure near the open hole, (3) pore overpressure or underpressure in the host rock, and (4) hydraulic pressure applied on the wellbore. Although uniform volumetric deformation may give rise to deviatoric stresses, the isotropic stress components in the rock do not cause failure, which is why deviatoric stresses are the main focus in this analysis. The deviatoric stress can be represented in both a tensor and a principal form. There are three principal deviatoric stresses τ_1, τ_2 and τ_3, of which—in our analysis—the intermediate stress (τ_2) is assumed to be aligned with the drilling direction and the two other principal stresses are in the transverse direction. In Section 10, however, a field example is provided in which the borehole is aligned with τ_3. In reality, the borehole can be in the direction of any of the far-field principal stresses, or none of them, and the orientations used in this thesis are for sake of simplicity in understanding and illustration. Note that in the Andersonian stress regimes, one of the three deviatoric principal stresses is assumed to be zero. The in-plane far-field stresses τ_1 and τ_3 will determine the stress trajectory the same as that determined by total stress. There is also no difference in determining the principal stress from far-field deviatoric stresses τ_1 and τ_3, and from total

stresses with symbols σ_1 and σ_3, except for an isotropic term. This notation follows common practice in structural geology literature (Weijermars, 1998; Fossen, 2010).

The analytical solutions used in this study, derived from the classical expressions of Kirsch (1898; based on the contemporary textbooks by Bach, 1898 and Föppl, 1897), consider pressure loaded cylindrical cavities with variable amounts of formation pressure and native far-field stress. These equations assume homogeneous elastic response and have vast applications in engineering involving stressed elastic plates with holes (e.g., Muskhelisvili, 1954; Savin, 1961; Malvern, 1969; Timoshenko and Goodier, 1970; Jaeger and Cook, 1979; Delale, 1984). Such applications include modeling the state of stress around geological intrusions, wellbores, caverns, and tunnels. The Kirsch equations have additionally been used in momentous studies showing geological and geotechnical applications (e.g., Jaeger et al., 2007; Zoback, 2007; Fjaer et al., 2008; Zang and Stephansson, 2010).

Recent studies have shown that the principal stresses around cylindrical cavities and wellbores with a uniaxial stress field and variable wellbore pressures scaled by the Frac Number show a large range of stress trajectory patterns (Weijermars, 2011, 2013; Weijermars and Schultz-Ela, 2012; Weijermars et al., 2013a; Weijermars, 2016; Weijermars and Thomas, 2017*). The present study expands that analysis by including systematic near borehole stress solutions for general bi-axial far-field stress states by use of the Bi-axial Stress Scalar (χ). The derivation of the non-dimensional form of the Kirsch equations for a general bi-axial far-field stress state is detailed in Section 3.1.

2.3 Stress nomenclature

Understanding stresses can be a very difficult business. This is due in part to their complex tensor nature of having both direction and magnitude components. The other confusions come from different notations amongst different fields of study; throughout this study, the rock mechanics notation is adopted where positive stresses are understood to be compressional and negative stresses are tensional. A third confusion arrives when considering that there are indeed two types of principal stresses: total stresses and deviatoric stresses. Throughout this study, total stresses will be denoted by σ and deviatoric stresses by τ, unless otherwise explicitly stated. Deviatoric stresses will be used, primarily. Normal and shear stresses will be denoted by either single subscripts, σ_N and σ_s, respectively, or double subscripts (e.g., σ_{xx} and σ_{xy}) when using tensor notation.

The total stress, σ, is made up of both a pressure component and the deviatoric stress. The pressure acts equally in all directions and therefore can cause only a potential volume change, whereas the deviatoric stress is free from any pressure contribution and causes distortions of shape. For this reason, equations governing elastic deformation or ductile creep apply the deviatoric stresses into the calculations. Pressures and stresses can be related by

$$\tau_{1,2,3} = \sigma_{1,2,3} - P \tag{1}$$

where

$$P = \sigma_{mean} = (\sigma_1 + \sigma_2 + \sigma_3)/3 \tag{2}$$

or in two dimensions:

$$P = \sigma_{mean} = (\sigma_1 + \sigma_3)/2 \tag{3}$$

2.4 Frac Number (F)

The Frac Number (*F*) was introduced by Weijermars et al. (2013) to characterize and identify the full-range of non-dimensional net-pressures in cylindrical wellbores.

$$F = \frac{P_{NET}}{|\tau_1|} \tag{4}$$

In drilling, the wellbore differential fluid pressure (P_{NET}) balances the elastic stresses on the rim of the borehole due to the lithostatic load of the mud in the column and from the formation fluid pressures. Balancing P_{NET} is crucial for well-control; this is done by pumping mud of an appropriate density downhole. The borehole fluid must have a density that balances that of the wall rock in order to prevent blowouts. During drilling, the net radial pressure due to elastic expansion or compression of the wellbore rim is given by

$$P_{NET} = P_{mud} - P_{ffp} \tag{5}$$

where P_{mud} is the hydrostatic pressure exerted on the bottom of the hole and P_{ffp} is the formation fluid pressure. This assumes a reasonably efficient mud cake, and can be modified to account for its absence. If the mud weight is increased, it results in an increase in radial stress and a decrease in tangential stress, which usually inhibits breakout formation. On the other hand, elevated mud pressures increase the likelihood of drilling-induced tensile wall fractures.

When $P_{NET} > 0$ (i.e., when $P_{mud} > P_{ffp}$; Fig. 2 Top row), the rock at the edge of the cylindrical hole dilates causing compressional radial stress to develop (Alberty and McClean, 2004). Overpressured rocks pose a potential hazard for drillers because accounting for the fluid pressure can be problematic in calculations compensating for mud

density. Overpressure may be related to the dehydration of montmorillonite to illite during non-equilibrium compaction (i.e., expulsion of lattice-locked water and the resulting rise of fluid pressure), rapid burial, thermal expansion of pore fluid, or hydrocarbon gas generation during subsidence.

Conversely, when $P_{NET} < 0$ (i.e., when $P_{mud} < P_{fp}$; Fig. 2 Bottom row), radial tension stress occurs (fracture cage, as radial fractures cannot form, only concentric fractures may develop). This study normalizes P_{NET} by dividing through by $|\tau_1|$, which allows for non-dimensional comparisons. For example, the likelihood of radial tension failure increases, and the range of possible failure orientations increases, as F becomes larger positively, leading to a loss of circulation and lost returns. Conversely, the larger F becomes negatively, the risk of concentric tensional failure and/or shear failure increases. These two cases (F being either positive or negative) help explain the intricate relationship between P_{NET} and τ_1, and show the potential risks of failure associated when the ratio of the two is large: Tensional failure when $F >> 0$ and shear failure when $F << 0$.

A demonstration of the Frac Number effects on stress trajectory patterns, and by extension, failure modes and orientations, is presented in Fig. 2. **The top row** shows that for overbalanced boreholes (F>0), the maximum principal stress trajectories (blue lines) direct radially towards the borehole (**Left**). Accordingly, if the rock meets the criteria for tensional failure to occur, fractures will propagate radially out from the hole as indicated by the red lines. The red lines purposefully correspond to the preferred fracture paths seen in the **right-hand-image** which shows a bullet making impact with bulletproof glass, creating a compressive shockwave as $F \rightarrow +\infty$. **The middle row** represents a balanced

borehole (F=0). **On the left,** the compressive τ_1 (blue) trajectories balance the tensional τ_3 (green) trajectories. The red dots indicate neutral point regions. Accordingly, in the glass plate example (**Right**), we expect a balance of stresses, with an uncompromised glass pane. In **the bottom row**, underbalanced borehole conditions prevail (F<0). **On the left,** maximum principal stress (τ_1) trajectories redirect and form closed elliptical rings around the hole. In the glass plate example (**Right**), circumferential fractures occur as a bullet makes vacuum as it passes through a pane of glass sending $F \rightarrow -\infty$. Recall that tensional fractures propagate perpendicular to the least principal stress. Under such conditions, shear failure is likely due to favorable shear stress orientations (Section 6 for further detail).

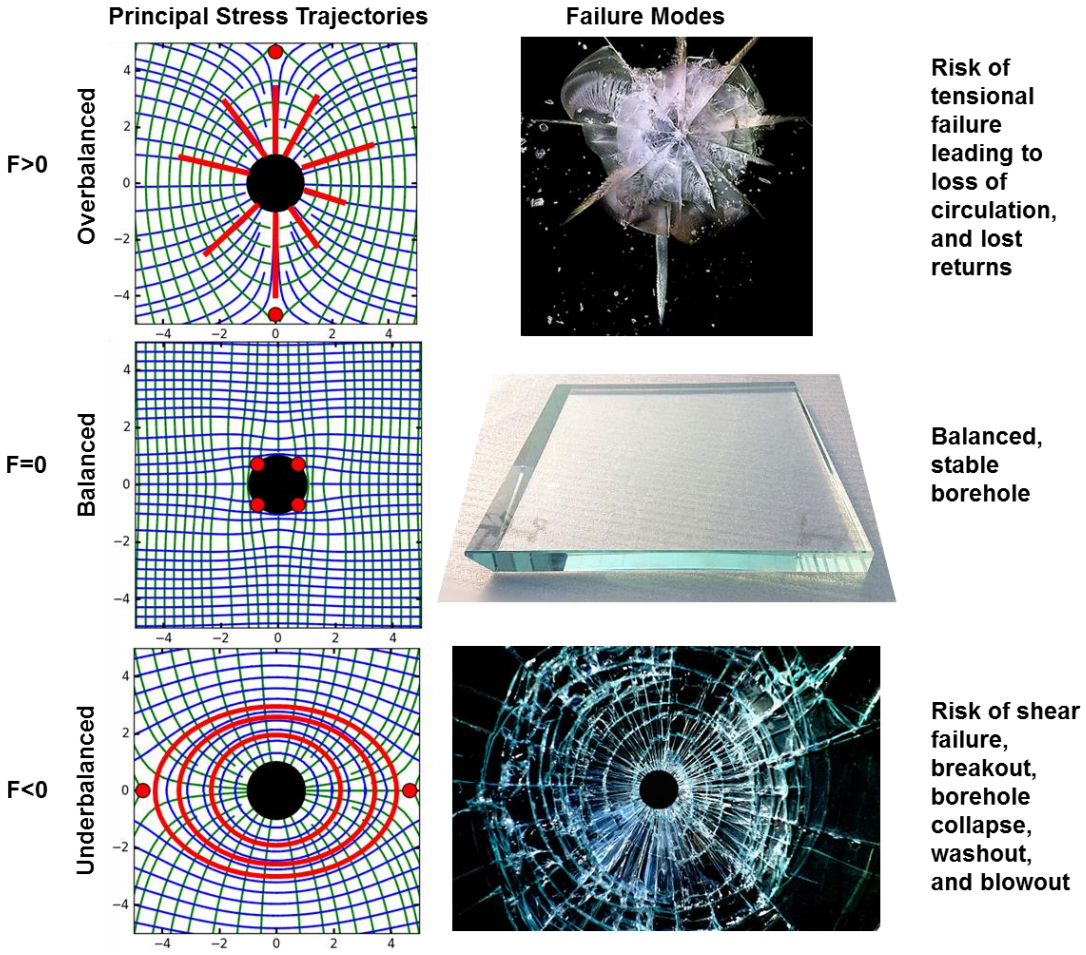

Figure 2: Glass plate representation used analogous to principal stress trajectory paths for different Frac Number: Overbalanced (Top), Balanced (Middle), and Underbalanced (Bottom). Adapted from Weijermars (2016).

2.5 Bi-axial Stress Scalar (χ)

The degree of anisotropy in the bi-axial stress field can be characterized by the Bi-axial Stress Scalar (χ):

$$\chi = -\tau_3/|\tau_1| \tag{6}$$

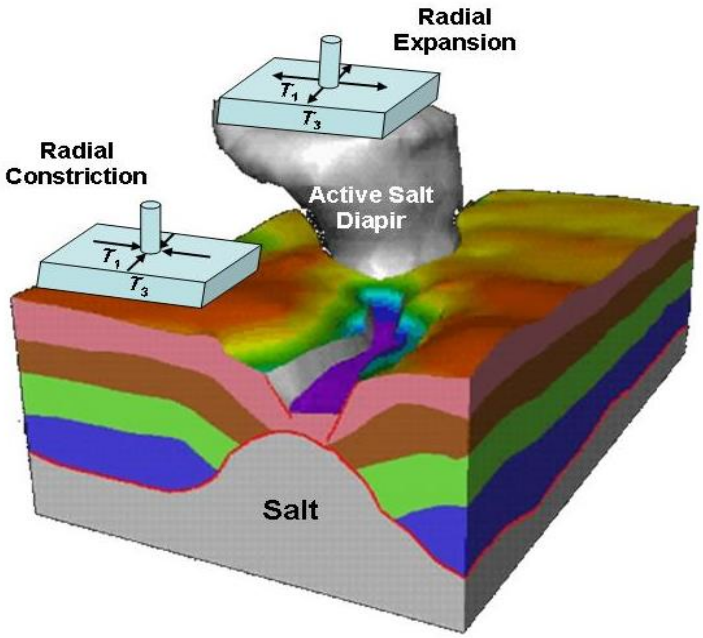

Figure 3: Principal deviatoric stresses in the sedimentary overburden around an active salt diapir. Radial expansion occurs above and around the widest part of the diapir. In the adjacent minibasin, radial constrictional stresses occur. Sediment slabs penetrated by a wellbore sketch the principal stress orientations for each case. Reprinted from Thomas and Weijermars (2017; *Submitted ESR).

Rather than assuming the far-field plane stress case ($\tau_1 = -\tau_3$), which is only one special case of the far-field bi-axial stress state, use of the Bi-axial Stress Scalar expands the solution range to cover the full range of possible bi-axial stress fields ($-1 \leq \chi \leq 1$), from far-field plane stress ($\chi=1$) to uniaxial stress ($\chi=0$), and can even account for radial constriction or radial expansion ($\chi=-1$; Fig. 3) states of the far-field stress. This study primarily focuses on far-field stress conditions ranging from uniaxial to bi-axial plane ($0 \leq \chi \leq 1$) because situations where radial constriction or expansion occur are far less common.

2.6 Poroelastic effects

Poroelasticity, first introduced by Biot (1941) and furthered by Verruijt (1969), Rice and Cleary (1976), and Detournay and Cheng (1993), describes the interaction between fluid flow and solids deformation within a porous medium. Porous materials are solid structures containing pores or voids. Subsurface rocks are naturally filled with cracks and pores that are saturated with one or more fluid phases (water, air, oil, etc.). These pore fluids have a major influence on the mechanical behavior of a rock mass. For example, when a rock is under compression, a pore fluid pressure causes the state of stress to move closer to the Mohr-Coulomb failure envelope (see Fig. 4). In addition to this, pore fluid pressures give rise to macroscopic elastic deformation of the rock. The mechanical deformation of a rock is therefore intrinsically coupled to the pore fluid pressure. Pore fluids flow through the rock in response to gradients in the pore pressure, but can also flow due to changes in the macroscopic stresses as a result of natural causes, such as tectonic forces, and man-made causes, such as the drilling of boreholes. Thus, the mechanical and hydrological behavior of rock is fully coupled (Jaeger and Cook, 2007).

In later presentations of the theory, starting with those of Biot, compression of the pore fluid and compression of the particles has been considered. This generalization has made it possible to also consider the deformations of stiffer materials such as sandstone and other porous rocks, which are very important in the engineering of deep reservoirs of oil or gas. The linear theory of poroelasticity (or consolidation) has now reached a stage where there is practically a general consensus on the fundamental equations (e.g.,

Detournay & Cheng, 1993; De Boer, 2000; Wang, 2000; Rudnicki, 2001; Coussy, 2004; Gambolati, 2006; and Verruijt, 2008).

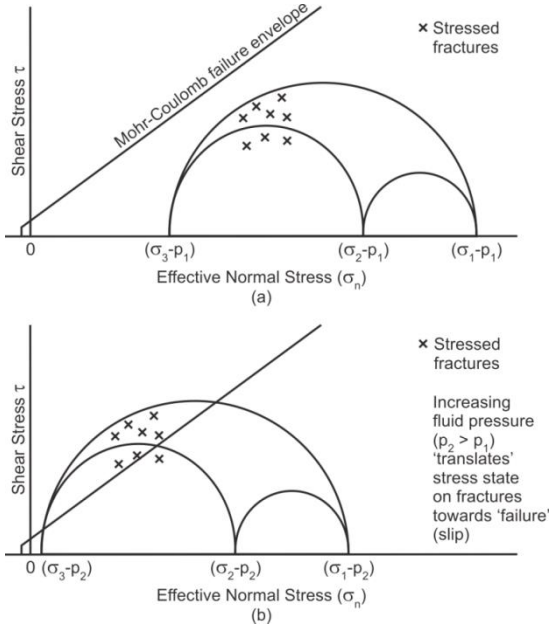

Figure 4: Hydro-shearing — a procedure to generate slip on pre-existing fractures by increasing the fluid pressure to a level below that required to generate a hydraulic fracture. Reprinted from Fairhurst (2013).

The effective stress, introduced by Terzaghi (1923, 1925), is defined as the part of the total stresses which governs the deformation of the soil or rock. It is assumed that the total stresses can be decomposed into the sum of the effective stresses and the pore pressure, by writing

$$\sigma_{ij} = \sigma'_{ij} + \alpha p \delta_{ij} \tag{7}$$

where σ_{ij} are the components of total stress, σ'_{ij} are the components of effective stress, p is the pore pressure (the pressure in the fluid in the pores), δ_{ij} are the Kronecker delta

symbols (δ_{ij} = 1 if i = j and δ_{ij} = 0 otherwise), and α is Biot's coefficient. For the isotropic parts of the stresses it follows from Eq. 7 that

$$\sigma = \sigma' + \alpha p \tag{8}$$

Most analyses of subsurface flow problems (including those related to petroleum engineering) are generally solved under the assumption that the rock mass is porous but rigid. Rock mechanics analyses similarly either ignore pore fluid effects altogether or assume that the pore pressures can be found independently of the mechanical deformation. Although there are many situations in which these assumptions are acceptable, there are instances when poroelasticity must be accounted for. For example, pore pressure effects play an important role in the deformation around a borehole (Detournay and Cheng, 1988), in hydraulic fracturing of boreholes (Detournay et al., 1989), and in slip along active faults (Rudnicki and Hsu, 1988).

Especially note that ***the effective stress should not be confused with the deviatoric stress*** in the particles, which would be obtained by subtracting the average pressure $P = (\sigma_1 + \sigma_2 + \sigma_3)/3$ (Eq. 2) from the total stress σ. It is essential to recognize that the pore pressure, *p*, not only acts in the pores, but also in the particles, which are fully surrounded by pore fluid.

Processes that increase pore pressure include:

- Undercompaction caused by rapid burial of low-permeability sediments (Devine, 2014; Sayers et al., 2005)
- Lateral compression (Kaeng et al., 2015)

- Release of water from clay minerals caused by heating and compression (Van Goten and Choudhary, 1969; Moore et al., 1983)
- Expansion of fluids because of heating (Zhang, C.-L., 2015)
- Fluid density contrasts (centroid and buoyancy effects; Kaeng et al., 2014)
- Fluid injection (e.g., waterflooding; Teklu et al., 2014)

Processes that decrease pore pressure include:

- Fluid shrinkage (Oyarhossein and Dusseault, 2015)
- Unloading (Couzens-Schultz et al., 2013)
- Rock dilation (Wang et al., 2015)
- Reservoir depletion (Ma and Zoback, 2016; Schutjens et al., 2012)

2.7 Thermoelastic effects

Thermoelasticity also plays an important role in understanding rock mass deformation. The theory is developed analogously to poroelasticity with the temperature acting in the role of the pore pressure (Norris, 1992). A significant difference between the two theories occurs in that thermomechanical coupling is unilateral in most situations, meaning that the temperature field influences the mechanical deformation, but the stresses and strains have a negligible effect on the temperature (Boley and Weiner, 1960), whereas on the other hand, the coupling in poroelasticity between mechanical deformation and pore pressures typically cannot be ignored (Fahrenthold and Cheatham, 1986; Zimmerman, 2000). Although a brief description is given here, thermoelastic effects are not explored in this study because they are included into the governing equations the same way that

poroelastic effects are (i.e., an increase in thermoelastic effects would produce the same results as a proportional increase in poroelastic effects, and since the solutions of this study are general, the analysis of this additional component was not warranted). When modeling a specific case, however, thermoelastic effects would be important to consider since they also reduce the effective stress.

3. METHODOLOGY

Drilling causes the stresses around a wellbore to redistribute as the excavated rocks are replaced by drilling fluid. This stress redistribution can lead to either shear failure (breakout) or tensile failure (fracturing). Wellbore instability caused by a mud weight that is less than the shear failure pressure (outside the safe operating envelope) can result in borehole breakouts, hole closure, pack-off or hole collapse (Fig. 5, left-hand-side). On the other hand, if the wellbore mud pressure is too high (exceeds formation pressure), there is a danger of tensile failure, causing the wellbore to balloon, and leading to mud loss and lost circulation (Fig. 5, right-hand- side).

Wellbore instabilities can increase non-productive drilling time and sometimes lead to wells being side-tracked or abandoned. A sound geomechanical model is crucial for the design and execution of a safe, cost-efficient wellbore. The static analytical stress solutions used in this study can readily be applied in place of more advanced numerical models when such complex geomechanical models are either too expensive or too cumbersome (or both), as is often the case.

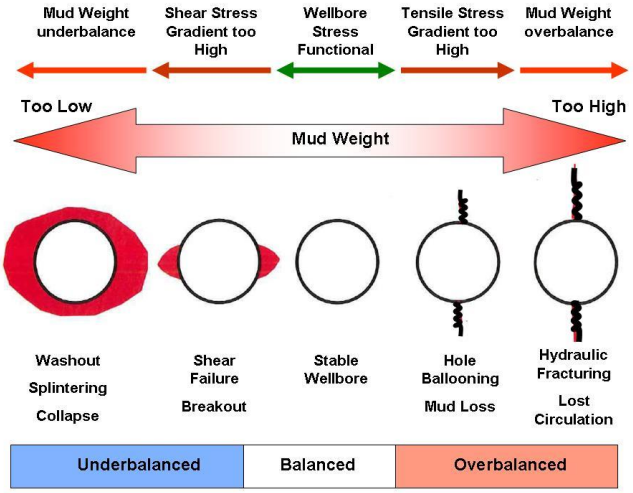

Figure 5: Mud weight is used to balance formation pressures on the wellbore. Due to different formation pressures at different depths, the average mud density may lead to imbalances at specific depths. The aim is to maintain a stable wellbore, but the occurrence of overbalanced and underbalanced sections cannot be excluded to occur. Adapted from Li et al. (2012).

Wellbore stability modeling prior to drilling can improve well design by determining a favorable wellbore trajectory and by identifying potential hazard areas. The well design should focus on optimum placement of the well trajectory in relation to the azimuth of the principal stresses and mud weight. The driving factors concerning wellbore stability are in-situ stress orientations and magnitudes, pore pressure, and rock strength (Peška and Zoback, 1995; Moos et al., 2003). Experts can monitor these parameters as the well is drilled to minimize wellbore stability problems and reduce non-productive time. Without any further guiding information, well-site engineers often use basic trial-and-error methods based on simple mud weight correlations to nearby or analogue wells. They maintain this mud weight until a failure is observed, at which point corrective action is

taken – not necessarily the most cost-efficient strategy. Failure or instability can be recognized by cavings that come up in the shale shaker (Fig. 63), by packoffs, or stuck pipe. The shape of the cavings on the shaker could hold the key to determining the stress state at the time of failure because the angle of failure is indicative of rock properties (angle of internal friction) and the direction of far-field stresses (rotated by a favorable shear orientation to give the slip lines; see Section 8), and the depth or severity of failure is indicative of the stress magnitudes and pore pressures.

Several software products exist which allow for planning the optimal well trajectory and calculating a critical mud weight window. Unfortunately, many of these tools do not provide the user with the detailed mathematics involved for making wellbore design decisions. Also, commercial wellbore stability software packages do not systematically illustrate the principal stress trajectories in the near-wellbore region, even though these stress trajectories comprehensively define some of the key elements of wellbore stability. Instead, it is common practice to show only the mud weight window and the orientations of the maximum and minimum principal stresses at the borehole wall. With this information, however, the principal stress orientations and magnitudes can be quantified everywhere in the plane around the borehole, and not only at its boundary. This additional information is critical in understanding how the stresses redistribute and redirect in the near-wellbore region.

Although commercial numerical methods models do exist (e.g., ABAQUS^{TM}), they require a great deal of input data from the user. This added complexity is often not practical for an operator, especially a smaller one. For the sake of saving time and money,

our simple analytical model can be supplanted for these more sophisticated methods. Consequently, our stress trajectory atlas and methods may provide valuable additional insight and support for wellbore planning. Another potential use of this modeling is to better understand rock strength. Industry practice has a much better handle on stress fields than on rock strengths. If a mud weight model predicts wrong, it is usually due to encountering an unexpected rock strength and not due to an unexpectedly high effective stress. If we can learn to characterize the orientation of stress planes from the shapes of cavings we find on the shaker (Fig. 63), we may be able to do a better job of understanding the in situ confined strength of the failed rock (which is very difficult to know) and perhaps structural directional strength aspects that may have contributed. This could help to assign more realistic values to the rock strength for future well planning.

Additional caution should be observed when drilling infill wells or planning production stimulation by hydraulic fracturing or waterflooding. Producing from a reservoir decreases the pore-fluid pressure and increases the effective stress acting on the load-bearing-grain framework that makes up the reservoir. Consequentially, the reservoir deforms and compacts, which in turn causes deformations and displacements in the host rock. Schutjens et al. (2012) showed that a production-induced stress field (depleted model) resulted in stress changes up to several MPa in magnitude compared to the preproduction stress state. They also note that only minimal changes in the stress orientations occur, congruent with Kirsch equation solutions, which show that pore pressure has no effect on principal stress orientations (Section 7).

The present study focuses on elastic response and possible failure modes around cylindrical boreholes in stressed rock formations, which is an appropriate approximation for the mechanical behavior of most rocks, and expanded with poroelastic behavior when pore volumes become relevant. The unique response of rock salt when drilled includes an instantaneous elastic response, but as rock salt is viscoelastic on longer time-scales (depending on the Maxwell relaxation time), uncased boreholes tend to close by viscous creep (Weijermars et al., 2013b) and cased boreholes may fail due to viscous drag on the casing (Weijermars et al., 2014). A detailed study of the ductile, long-term response of wellbores in salt is not warranted in this study.

3.1 Solutions in 2D

Under the assumption that a borehole is drilled in a homogeneous, isotropic, and linear elastic rock continuum, the analytical Kirsch (1898) equations provide solutions for the stresses around the hole as follows:

$$\tau_r = P_{NET}c^2 + \frac{1}{2}(\tau_1 + \tau_3)(1 - c^2) + \frac{1}{2}(\tau_1 - \tau_3)(1 - 4c^2 + 3c^2)\cos 2\theta \quad (9a)$$

$$\tau_\theta = -P_{NET}c^2 + \frac{1}{2}(\tau_1 + \tau_3)(1 + c^2) - \frac{1}{2}(\tau_1 - \tau_3)(1 + 3c^2)\cos 2\theta \quad (9b)$$

$$\tau_{r\theta} = -\frac{1}{2}(\tau_1 - \tau_3)(1 + 2c^2 - 3c^2)\sin 2\theta \quad (9c)$$

where τ_1 and τ_3 are the magnitudes of the far-field principal deviatoric stress, P_{NET} is the net borehole fluid pressure, θ is the angle measured from the direction of the maximum principal stress, τ_1 (i.e., τ_1 is aligned with $\theta=0^o$), and $c = a/r$, where a is the hole's radius and r is the distance from the center of the hole. In this study, the hole's radius is given unit length (i.e., $a=1$). Additionally, the rock mechanics understanding of stress is being

applied, which agrees that compressive stress is positive and tension is negative. Equations (9a-c) can be made dimensionless by dividing through by the principal stress $|\tau_1|$, which gives a final set of wellbore stress algorithms in compact form, including both the Bi-axial Stress Scalar, χ, and the Frac Number, F:

$$\tau_r^* = Fc^2 + \frac{1}{2}(1-\chi)(1-c^2) + \frac{1}{2}(1+\chi)(1-4c^2+3c^4)\cos 2\theta \qquad (10a)$$

$$\tau_\theta^* = -Fc^2 + \frac{1}{2}(1-\chi)(1+c^2) - \frac{1}{2}(1+\chi)(1+3c^4)\cos 2\theta \qquad (10b)$$

$$\tau_{r\theta}^* = -\frac{1}{2}(1+\chi)(1+2c^2-3c^4)\sin 2\theta \qquad (10c)$$

The expressions derived above allow the visualization and monitoring of the radial and tangential stresses in the plane perpendicular to the wellbore for any bi-axial far-field stress and wellbore net pressure, which can be used in well-pressure management systems to practically improve well control and safety management.

Eqs. (10a-c) quantify the magnitudes of the radial and tangential stresses in any spatial locations around the wellbore. If we additionally want to quantify the magnitude of the principal stresses, we must first find the Cartesian stress elements $\tau_x^*, \tau_y^*,$ and τ_{xy}^* in terms of polar coordinate elements τ_r^*, τ_θ^*, and $\tau_{r\theta}^*$, respectively. The Cartesian stress elements for a particular coordinate system where the x-axis is aligned with θ=0º can be obtained using the following tensor transformation:

$$\begin{bmatrix} \tau_x^* & \tau_{xy}^* \\ \tau_{yx}^* & \tau_y^* \end{bmatrix} = \begin{bmatrix} \cos\theta & -\sin\theta \\ \sin\theta & \cos\theta \end{bmatrix} \begin{bmatrix} \tau_r^* & \tau_{r\theta}^* \\ \tau_{\theta r}^* & \tau_\theta^* \end{bmatrix} \begin{bmatrix} \cos\theta & \sin\theta \\ -\sin\theta & \cos\theta \end{bmatrix} \qquad (11)$$

which simplifies to:

$$\tau_{xx}^* = \tau_r^* \cos^2\theta - 2\tau_{r\theta}^* \sin\theta\cos\theta + \tau_\theta^* \sin^2\theta \qquad (12a)$$

$$\tau_{yy}^{*} = \tau_{r}^{*}\sin^2\theta + 2\tau_{r\theta}^{*}\sin\theta\cos\theta + \tau_{\theta}^{*}\cos^2\theta \quad (12b)$$

$$\tau_{xy}^{*} = (\tau_{r}^{*} - \tau_{\theta}^{*})\sin\theta\cos\theta + \tau_{r\theta}^{*}(\cos^2\theta - \sin^2\theta) \quad (12c)$$

Applying double angle trigonometric substitutions, recalling that

$\sin^2\theta = \frac{1}{2}(1 - \cos2\theta)$, $\cos^2\theta = \frac{1}{2}(1 + \cos2\theta)$, and $2\sin\theta\cos\theta = \sin2\theta$, gives:

$$\tau_{x}^{*} = \frac{1}{2}\tau_{r}^{*}(1 + \cos2\theta) - \tau_{r\theta}^{*}\sin2\theta + \frac{1}{2}\tau_{\theta}^{*}(1 - \cos2\theta) \quad (13a)$$

$$\tau_{y}^{*} = \tfrac{1}{2}\tau_{r}^{*}(1 - \cos2\theta) + \tau_{r\theta}^{*}\sin2\theta + \tfrac{1}{2}\tau_{\theta}^{*}(1 + \cos2\theta) \quad (13b)$$

$$\tau_{xy}^{*} = \tfrac{1}{2}(\tau_{r}^{*} - \tau_{\theta}^{*})\sin2\theta + \tau_{r\theta}^{*}\cos2\theta \quad (13c)$$

The dimensionless magnitudes of the deviatoric principal stresses, τ_1^* and τ_3^*, can be obtained by substituting the derived expressions for τ_x^*, τ_y^*, and τ_{xy}^* into the standard expressions for determining the principal stresses everywhere in the plane of observation:

$$\tau_{1}^{*} = \frac{1}{2}\left(\tau_{x}^{*} + \tau_{y}^{*}\right) + \left[\tau_{xy}^{*2} + \frac{1}{4}\left(\tau_{x}^{*} - \tau_{y}^{*}\right)^2\right]^{\frac{1}{2}} \quad (14a)$$

$$\tau_{3}^{*} = \frac{1}{2}\left(\tau_{x}^{*} + \tau_{y}^{*}\right) - \left[\tau_{xy}^{*2} + \frac{1}{4}\left(\tau_{x}^{*} - \tau_{y}^{*}\right)^2\right]^{\frac{1}{2}} \quad (14b)$$

Principal stresses act on planes where shear stress is equal to zero. Therefore, the principal stress directions in (x^*, y^*)-space are determined by setting the shear stress equal to zero and solving for the directional angle. In doing so, the principal stress trajectories are fully determined by the angle β (Weijermars, 2011):

$$\tan2\beta = \frac{2\tau_{xy}^{*}}{\tau_{x}^{*} - \tau_{y}^{*}} \quad (15)$$

$$\beta = \frac{1}{2}\arctan\left(\frac{2\tau_{xy}^*}{\tau_x^* - \tau_y^*}\right) \tag{16}$$

with the two conjugate solutions for β separated by $\pi/2$. A continuous solution of Eq. (16) outlines the stress trajectories in a spatial plane perpendicular to the wellbore.

The principal stress trajectories and magnitudes derived, respectively, from Eqs. (16) and Eqs. (14a,b) act within the plane perpendicular to the wellbore axis. Additionally, these principal stresses are also the maximum and minimum normal stresses that act on the respective material planes through the point of observation (Jaeger et al., 2007). Dimensional magnitudes of the stresses can be obtained applying basic scaling rules (Weijermars and Schmeling, 1986).

3.2 Stress Concentrations

The non-dimensional magnitudes of principal stresses τ_1 and τ_3 are solved for using Eqs. (14a,b). The principal stress solutions act within the plane perpendicular to the cylindrical cavity's axis and are the maximum and minimum deviatoric stresses that act on the respective material planes through the point of observation (Weijermars, 1998; Jaeger et al., 2007). Dimensional magnitudes of the stresses can be obtained by applying basic scaling rules (Weijermars and Schmeling, 1986). Stress concentrations will be greatest at the borehole wall. The radial, tangential, and shear stress concentrations at the borehole wall can be solved by setting c=1 in Eqs. (9a-c). This gives:

$$\tau_r = P_{NET} \tag{17a}$$

$$\tau_\theta = -P_{NET} + (\tau_1 + \tau_3) - 2(\tau_1 - \tau_3)\cos 2\theta \tag{17b}$$

$$\tau_{r\theta} = 0 \tag{17c}$$

Considering only the directions parallel and perpendicular to the minimum stress direction (i.e., $\theta = 0$ and $\theta = \pi/2$, respectively), the expression for the tangential stress at the borehole wall can be further simplified to:

$$\tau_{\theta\,(\theta=0)} = \tau_{\theta,min} = 3\tau_3 - \tau_1 - P_{NET} \tag{18a}$$

$$\tau_{\theta\left(\theta=\frac{\pi}{2}\right)} = \tau_{\theta,max} = 3\tau_1 - \tau_3 - P_{NET} \tag{18b}$$

From these equations, we can solve for the maximum principal stress concentrations at the wellbore wall, which is common practice since failure is most likely to occur here. The traditional ideal visualization of borehole breakout and tension failure is shown in Fig. 6. The analysis of Weijermars (2016) suggests that such breakouts and tension cracks are unlikely to form simultaneously at the same wellbore level, because tension cracks require overbalancing and breakouts require underbalancing. When $F<0$, breakouts and concentric spalling are likely, but radial tension failure cannot occur; whereas when $F>0$ breakouts are incompatible with shear direction but radial tension failure is likely. Coeval breakouts and tension fractures are therefore less likely at the same level in a wellbore, as was previously noted by Fjaer et al. (2008).

This study goes beyond quantifying the stress concentrations at the wellbore rim and analytically resolves the radial, tangential, and principal stress magnitudes at every point around the hole. This enables the visualization of the entire stress state as it changes in space due to the presence of a pressurized hole with various in situ stresses, formation pressures, and borehole pressures.

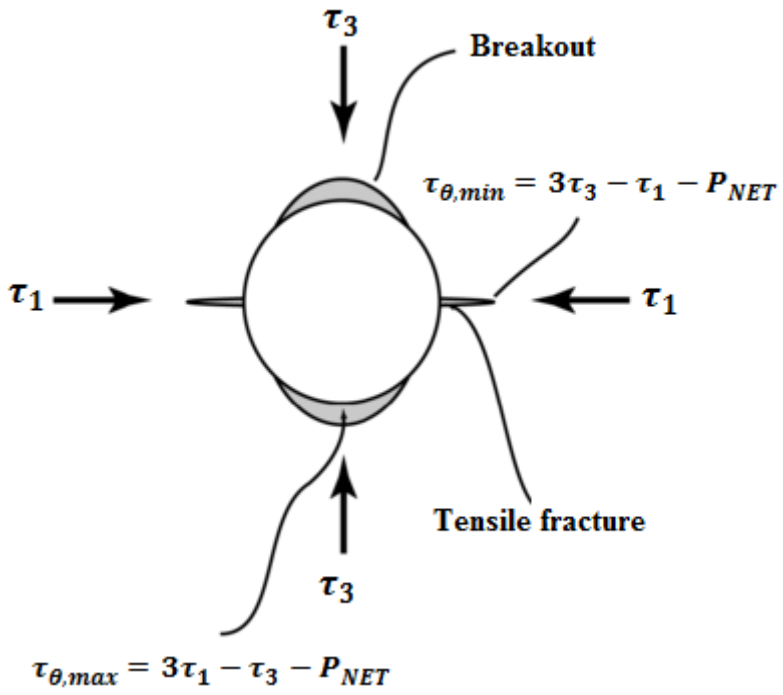

Figure 6: Maximum and minimum stress concentrations occur at the wellbore wall. Breakout occurs in the direction of τ_3 which is where τ_θ is minimum, and tensile failure occurs in the direction of τ_1, which is where τ_θ is maximum. Adapted from Moos (Fig. 1.18; 2006).

4. FUNDAMENTAL APPLICATIONS

4.1 Principal stress trajectories

The principal stress orientations can vary significantly from one point around the borehole to another due to a redistribution of the stresses. The exact orientations at each point in space around the borehole can be systematically resolved and plotted as trajectories (Eq. 16).

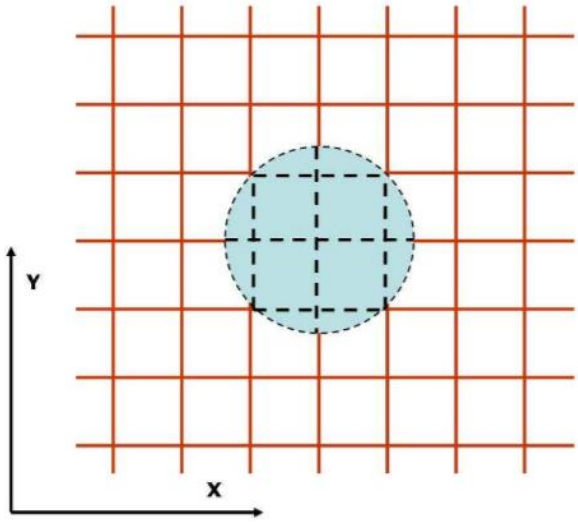

Figure 7: Stress trajectories in an elastic slab subject to a uniform far-field stress perpendicular to the axis of a virtual hole that exhibits no perturbation on the local stresses. Reprinted from Weijermars (2011).

In a uniform stress field (i.e., in the absence of any perturbations, like that from a stressed borehole), the stress trajectories are simply a set of orthogonal straight lines (Fig. 7). The stress trajectories for a non-uniform stress field, however, integrate the principal stress orientations into a set of smooth, curved, orthogonal lines.

The principal stress trajectories characterize many critical features regarding borehole stability and fracture propagation. A tension fracture will always propagate in the direction perpendicular to the least principal stress. Within this study, the compressive and tensile far-field stresses are oriented horizontally and vertically, respectively, in all plots and solutions (as seen in Fig. 8). In other words, τ_1 is aligned with $\theta=0^o$ and τ_3 with $\theta=90^o$. Along the vertical and horizontal axes, the radial and tangential stresses will each be identical to one of the principal stresses; along other directions, principal stresses may differ from radial and tangential stresses. The relationships depend upon the far-field stress anisotropy (χ) and the net hole-pressure (F).

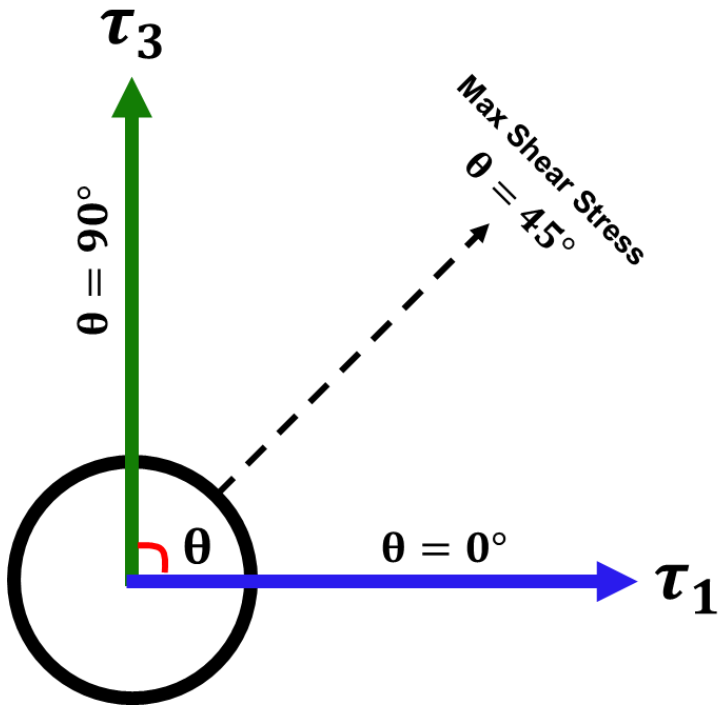

Figure 8: The fundamental stress orientation for subsequent plots throughout this study. The far-field maximum principal stress is aligned across the horizontal of the wellbore ($\theta=0^o$) and the far-field least principal stress is aligned vertically ($\theta=90^o$). Throughout the text, these directions will be referred to as principal axes.

In the absence of any far-field stress, overbalanced (F>0) and underbalanced (F<0) boreholes can be approximated by $F \to +\infty$ ('Starburst' pattern; Fig. 2 Top row) and $F \to -\infty$ (Circumferential faulting; Fig. 2 Bottom row), respectively. Figure 9a shows the overbalanced case and Figure 9b the underbalanced case. The maximum principal stress (blue) is radial in every direction for F>0, whereas when F<0, the maximum principal stress trajectories are tangentially-aligned, forming circular rings around the borehole. If we compared the magnitudes of the principal stresses with the tangential and radial stresses, we would observe that for F<0 (Fig. 9a), the radial stress is in fact the maximum principal stress everywhere and the tangential stress is the least principal stress. Contrarily, for the underbalanced borehole (F<0; Fig. 9b), the tangential stress is the maximum principal stress (τ_1) and the radial stress is the least principal stress (τ_3), everywhere around the borehole.

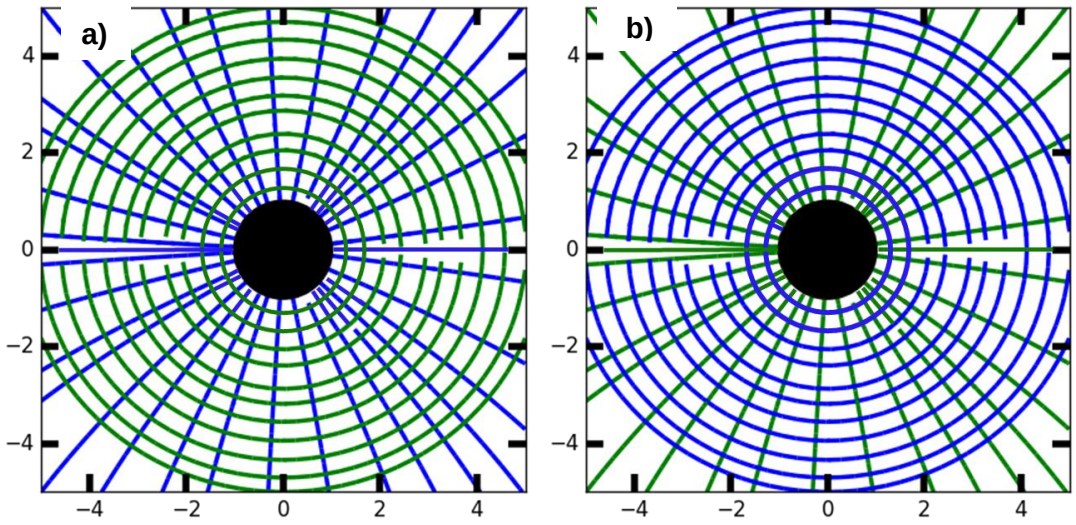

Figure 9: Principal stress trajectory patterns for boreholes with no far-field stress effects. **a:** An overbalanced borehole (F>0) causes τ_1 (blue) trajectories to direct radially into the borehole, with τ_3 (green) forming circular ringed patterns. Tensile failure is likely with fractures propagating radially along τ_1 trajectory, with initial fracture oriented along the τ_1 axis. **b:** Around an underbalanced borehole (F<0), the τ_1 trajectories are circumferentially oriented around the hole, forming closed-circular rings, and the τ_3 trajectories are radially aligned. If tensile failure occurs, fractures will propagate around the borehole along the τ_1 trajectories. Compressive or shear failure is likely, with an excess concentration of compressive tangential stress above the borehole (τ_3 direction).

When far-field stresses are considered, the stress trajectories become much more complex, and the radial and tangential stresses can switch between being the maximum or minimum principal stresses at neutral point locations (points where the magnitudes of τ_1 and τ_3 are equal). Fig. 10a and b illustrate the principal stress trajectories for two wellbores, both subjected to a bi-axial plane stress (χ=1) boundary condition, but with very different net borehole pressures. Fig. 10a shows locally overbalanced conditions where the borehole net fluid pressure is 5 times the magnitude of far-field τ_1. The compressive τ_1 trajectories (blue) are aligned horizontally, with all trajectories within a certain distance curving in

radially towards the borehole. The τ_3 trajectories (green), vertically aligned, elliptical rings around the borehole, with the outermost elliptical ring bounded by the neutral points (red dots). This outermost ring forms the boundary for the stress cage, inside which all radial stress is compression, even in the direction of far-field tension stress τ_3. Fig. 10b shows the stress trajectories around a wellbore subjected to underbalanced borehole conditions, where borehole net fluid pressure is -5 times the magnitude of far-field τ_1.

The solutions are complementary to what we see in Fig. 10a. Again, τ_1 trajectories are aligned across the horizontal; however, they are redirected around the borehole due to the local underbalance. The τ_1 trajectories form closed-elliptical rings around the borehole, with the outermost ring being bounded by the neutral points (red dots). In contrast to the overbalanced case, inside the fracture cage, all tangential stress is compressional. Under these conditions, a fracture, if not initially long enough to extend beyond the fracture cage, would propagate circumferentially around the wellbore, creating tortuosity which can lead to screenout of the proppant. Additionally, as will be shown later (Section 8), the compressive tangential stress (τ_1 is tangentially aligned around the borehole) can lead to compressive failure. Additionally, in underbalanced wellbores, the slip lines are preferentially aligned for shear failure (Section 8).

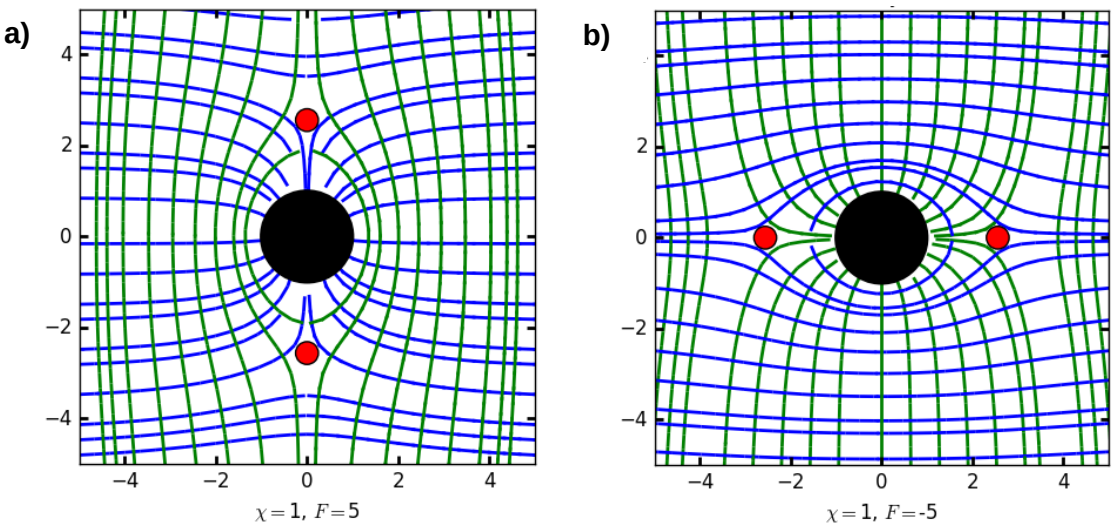

Figure 10: The principal stress trajectory patterns are shown for two wellbores, each with bi-axial plane stress conditions. The horizontal and vertical axes are non-dimensional distances from the center of the borehole, where each unit of length is equal to the borehole radius. Compressive principal (deviatoric) stress trajectories (τ_1) are plotted in blue while tensional principal stress trajectories (τ_3) are shown in green. Neutral points are indicated by red dots. **a:** Overbalanced borehole (F=5) An elliptical τ_3 stress trajectory passes through both neutral points marking the boundary of the stress cage. **b:** Underbalanced borehole (F=-5) The compressive stress, τ_1 (blue), forms concentric rings around the hole. Neutral points contain an elliptical τ_1 stress trajectory that forms the boundary for the fracture cage.

Stress trajectories are useful because they outline the spatial orientation of the minimum, intermediate, and maximum principal deviatoric stresses. An associated quantity is the direction of maximum shear stress. Shear stress orientations can be established from the principal stress directions by adaptation of a shear failure criterion. Shear failure criteria will be discussed in more detail in Section 8, but consider now that shear failure will occur along planes where stress anisotropy is greatest. The differential stress is lower in the direction of the neutral points because neutral points mark the location

where the two principal deviatoric stresses are equal (i.e., neutral points exists where $\tau_1 - \tau_3 = 0$), and is significantly higher in the direction normal to the direction of the neutral points.

4.2 Dynamic numerical solutions

The analytical Kirsch equations assume a static solution, and we are therefore primarily concerned with the principal stress trajectories and magnitudes pre-failure. At the point in time that any failure begins to occur, there will be a redistribution of stress, and other effects, which a time dependent numerical methods model would be needed to consider. Although our solutions are not meant to be applied liberally to describe time-dependent failure, our method has been corroborated by an independent study which used an advanced numerical methods model to simulate fracture growth in an underbalanced wellbore (for details, see Weijermars et al., 2013a).

Hydraulic fracture growth from a wellbore under plane strain conditions has been modelled in earlier numerical studies (Zhang et al., 2011a,b) using a displacement discontinuity boundary element method. The dynamic approach complements the above static analysis. A fully coupled hydraulic fracture model can analyze problems involving a Newtonian fluid injected at constant rate to grow a hydraulic fracture in impermeable rock. The fracture surface contact and frictional sliding are accounted for by a history dependent Coulomb friction law criterion. The numerical code ensures dynamic coupling of the fracture growth and the hydraulically induced stress around the borehole. For more

detailed descriptions of the model assumptions readers are referred to earlier studies (Zhang et al., 2009, 2011a,b; Jeffrey and Zhang 2010).

The static analytical solutions for the fracture cage (see Figs. 10b) are compared here to dynamic numerical solutions using the model explained above. Figures 11(a–c) show the numerical model for a case where two incipient fractures at the wellbore are respectively shorter and longer than the distance to the fracture cage boundary. The hydraulic fluid is injected from a slotted source located where the initial crack meets the wellbore. The short fracture stays trapped in the fracture cage when hydraulically loaded (Fig. 11a–c). The longer fracture extends long enough to have its fracture tip outside the fracture cage propagating further outwards into the rock matrix to align with the far field τ_1 trajectories (Fig. 11a–c). Figure 11d shows the analytical and numerical cases side by side for similar conditions, which confirms the validity of the numerical results; the fracture cage sizes match perfectly. The analytical stress trajectory solution explains why the short fracture curls around the wellbore and the long frac propagates towards the far field stress axis.

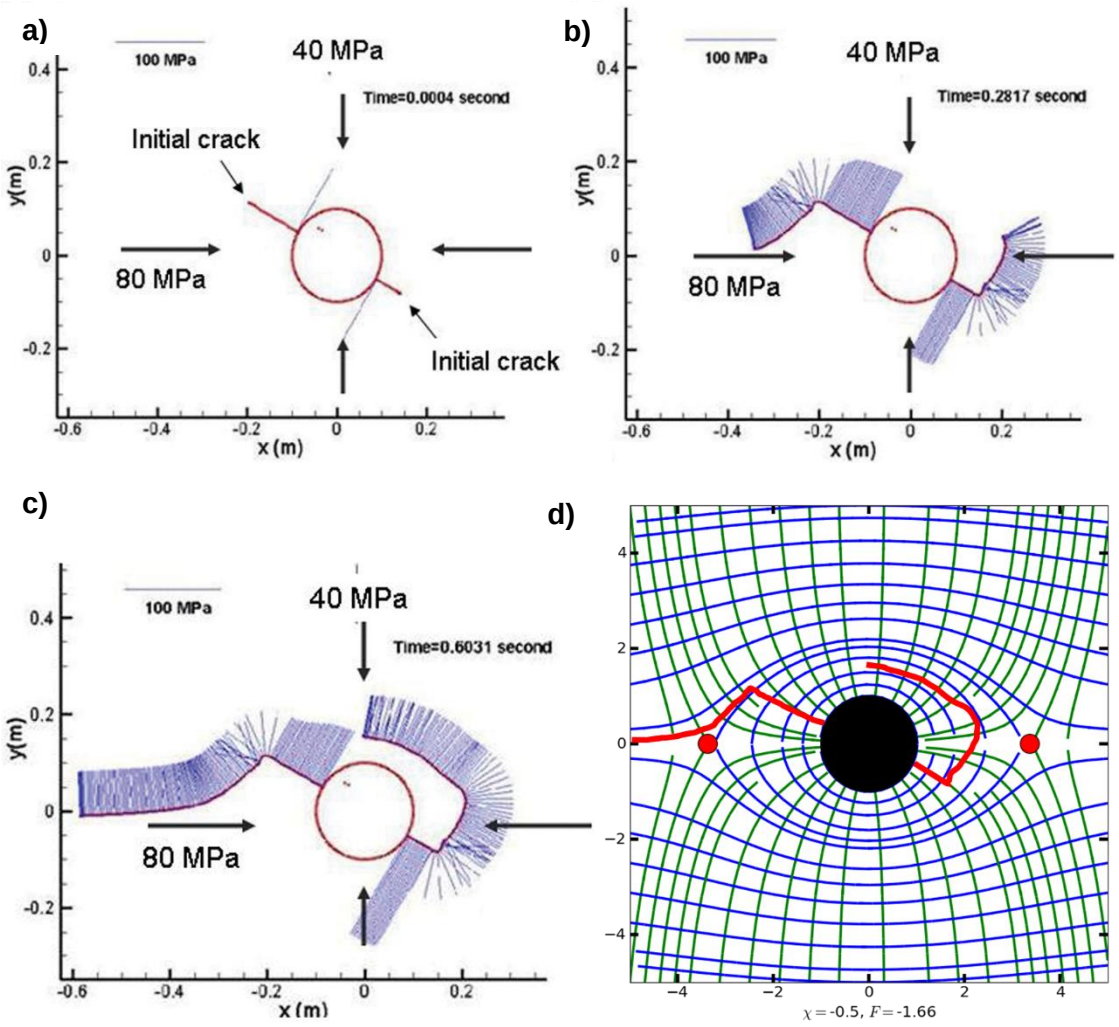

Figure 11: (a)–(c) Numerical simulation with initial cracks near the wellbore, one too short (0.64 times borehole radius, right fracture) and the other long enough (1.28 times borehole radius, left fracture) to escape outwards from the fracture cage (F=−1.66). The in-plane total far field stresses are specified as 40 and 80 MPa, respectively. Wellbore pressure is zero, but the pressure along the hydraulic fracture is not zero and intensity is given by the scaled blue lines. Material parameters for this simulation are: E = 30 GPa, Poisson ratio = 0.25, KIC (Toughness) = 5.62 MPa $m^{-1/2}$ (to slow down crack growth), dynamic viscosity=0.01 Pas, and initial hydraulic injection rate=0.0004 m^2 s^{-1}, fracture friction coefficient=0.5. Time steps are for (a) 0, (b) 0.3 and (c) 0.6 seconds after hydraulic injection. **(d)** Analytical stress trajectory solution for F =−1.66 delineating the fracture cage formed by the τ_1 stress ellipse around the wellbore. Axes are dimensionless distances normalized by the wellbore radius. Reprinted from Weijermars et al. (2013).

Figure 11 shows the analytical solution to exactly match a numerical simulation for a case where an incipient fracture at the wellbore is respectively shorter and longer than the distance to the fracture cage rim. The short fracture stays trapped in the fracture cage when hydraulically loaded (Fracture 1, Fig. 11a). The short fracture of Figure 9a may only propagate further by curling along the τ_1-trajectories, because tensile fractures always form perpendicular to the tensile stress (τ_3) and open in the direction of τ_3. The longer fracture extends long enough to have its fracture tip outside the fracture cage and can propagate further outward into the rock matrix to align with the far field τ_1 trajectories (Fracture 2, Fig. 11a). In fact, a stress cage effect may again occur when the hydraulic fracture escapes the fracture cage (Fig. 11b). However, without hydraulic loading of any such pre-existing cracks, wellbores that are underbalanced ($F<0$) will typically develop breakouts when the critical shear strength is reached (Fig. 6). Concentric spalling is likely to occur in underbalanced wellbores when the critical tensile strength is reached by the tangential tension stress (e.g., Fig. 2 bottom; Fig. 11d).

The reorientation of stresses inside the fracture cage, as illustrated above, is of crucial importance in hydraulic fracture design. Deviation of the trajectory of a horizontal well from the fracture direction, is the principle cause of tortuosity. Horizontal wells drilled parallel to the fracture direction will give the lowest level of stress induced tortuosity, although some tortuosity will still exist due to the nonconformities that exist in the near wellbore area. Drilling of horizontal wells along trajectories that limit tortuosity becomes very restrictive when trying to maximize reservoir drainage, especially in an offshore situation from a centrally located platform. Horizontal wells at an angle other

than parallel to the fracture direction will be subject to tortuosity effects when trying to place proppant (Kogsbøll et al., 1993).

4.3 Stress concentrations along far-field principal axes

Along the far-field principal stress axes (i.e., τ_1 is aligned with $\theta=0^o$ and τ_3 is perpendicularly-aligned, $\theta=90^o$), the principal stresses will be perfectly aligned with the radial and tangential stresses. Outside of these principal axes, there will be some variation between the principal stresses and the radial and tangential stresses. The plots below (Figs. 12-15) attempt to capture the phenomenon of stress reversal found along the principal axes at the neutral point locations, at which points the principal stresses characteristically reverse their relationships with the radial and tangential stresses.

Figures 12-15 plot the non-dimensional stress concentrations (normalized by τ_1) of the principal stresses, τ_1 and τ_3, and the radial and tangential stress, τ_r and τ_θ, along a specified principal stress axis. In each set of figures, the distances are non-dimensional, normalized by the radius of the hole. Figures 12-15 can be understood as follows:

- **(a)** The deviatoric principal stress magnitude concentrations are resolved along a specific far-field principal stress axis (i.e., either along $\theta=0^o$ or along $\theta=90^o$).
- **(b)** Contour plots show the stress magnitude of τ_1 varying in space around the hole, with a single blue line drawn to indicate the section along which stresses are plotted in (a).

- **(c)** Contour plots of the stress magnitude of τ_3 varying in space around a hole are shown with a single magenta line drawn to indicate the section along which stresses are plotted in (a).
- **(d)** The tangential (blue) and radial (magenta) stress magnitude concentrations are resolved along the same specific principal stress line as those in (a).
- **(e)** Contours of the dimensionless radial stress are shown. The bold line indicates the axis along which stress concentrations are resolved for the solutions in (d). Where the line is blue, the radial stress is identical to the maximum principal stress, and where it is magenta, it is identical to the least principal stress.
- **(f)** Contours representing the magnitude of the dimensionless tangential stress in space around a borehole. The bold line indicates the principal axis along which stresses are being measured for (a) and (d). When the line is blue, the tangential stress is aligned with the τ_1 stress, and with the τ_3 stress when the line is magenta.

In the below figures, the reversal effect between the principal stresses and the radial and tangential stresses that occurs at the neutral points is observed. When a borehole is overbalanced (F>0; e.g., Figures 12 & 13), the neutral points occur away from the wellbore along the direction of far-field τ_3 stress ($\theta=90^o$). Along the orthogonal principal stress axis ($\theta=0^o$), the radial stress is the maximum principal stress, and the tangential stress is the least principal stress. Along the neutral point axis, however, a reversal occurs, in that, the radial stress is the maximum principal stress close to the wellbore, but passing beyond the neutral point, the tangential stress becomes the maximum principal stress, and the radial stress becomes the least principal stress. Inside the stress cage, all radial stress

is compressional. Tensional failure is the probable mode of failure, and radial fractures will propagate in the direction of the radial τ_1 trajectories.

An opposite phenomenon occurs for underbalanced boreholes ($F<0$; e.g., Figures 14 & 15). Neutral points occur in the direction of the far-field τ_1 stress ($\theta=0^o$). As the radial maximum principal stress reaches the neutral points, the trajectory is tangentially redirected around the wellbore, so that inside the neutral points (inside the fracture cage), the maximum principal stress is tangential and the least principal stress is radial. Inside the fracture cage, all tangential stress is compressional. Any tensional failure inside the fracture cage would cause the fracture to redirect around the borehole, due to the maximum principal stress trajectories forming circumferential rings around the hole. The more probable mode of failure is shear/compressive failure due to the highly compressive tangential stress in the direction of the least principal stress, and due to the shear stress being preferentially oriented for failure (See Fig. 47b).

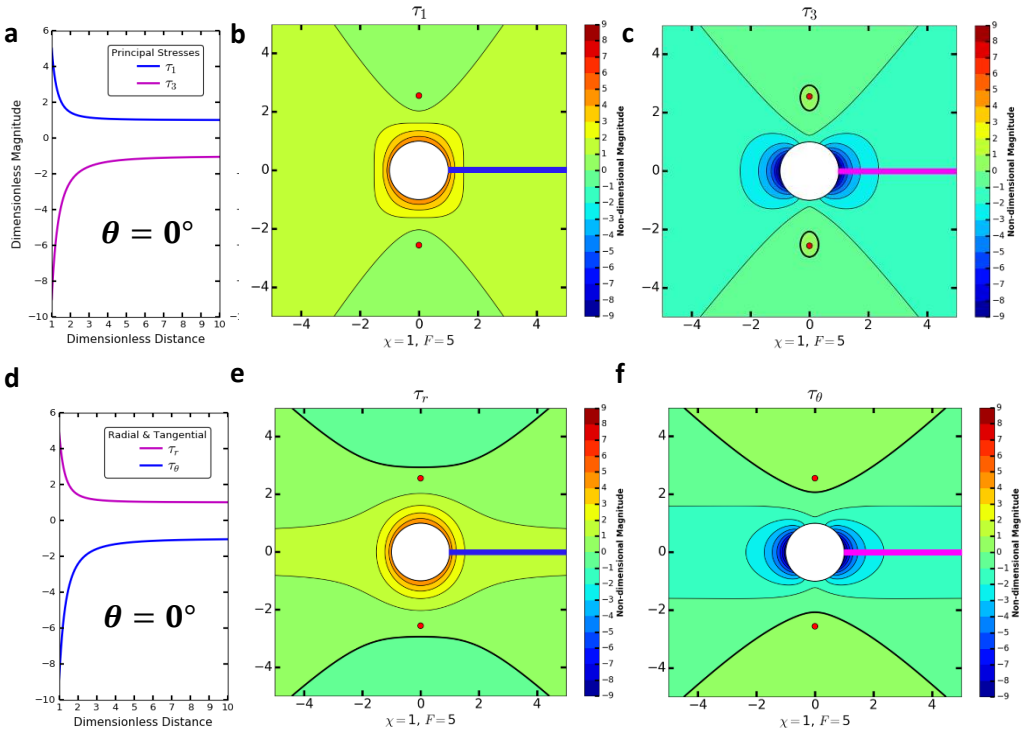

Figure 12: Solutions are along the τ_1 principal axis (θ=0º) for bi-axial plane stress (χ=1) and overbalanced pressure (F=5) conditions. **a:** The magnitude concentrations of τ_1 and τ_3 are plotted along the far-field τ_1 axis. **b:** Contours showing the non-dimensional magnitude of τ_1 in space around the hole. The blue line indicates the concentration of τ_1 shown in (a). **c:** Contours showing the magnitude of τ_3 in space around the hole. The magenta line indicates the concentration of τ_3 shown in (a). **d:** The radial τ_r and tangential τ_θ stress magnitudes are plotted along the far-field τ_1 axis, as in (a). **e:** Contours represent the radial stress magnitude in space around the hole. The line drawn is blue to indicate that along that entire principal axis, the radial stress is the maximum principal stress. **f:** Contours represent the tangential stress magnitude around the hole. The line drawn is magenta to indicate that along that entire principal axis, the tangential stress is the least principal stress.

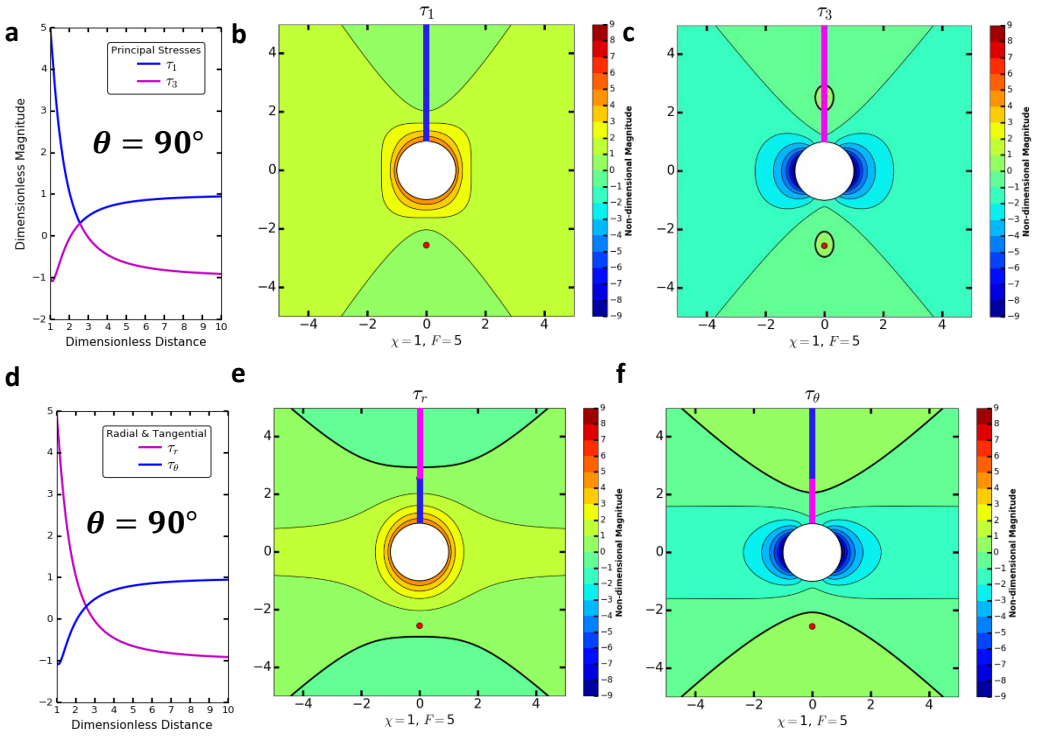

Figure 13: Solutions are along the τ_3 principal axis (θ=90º) for bi-axial plane stress (χ=1) and overbalanced pressure (F=5) conditions. **a:** The non-dimensional magnitude concentrations of τ_1 and τ_3 are plotted along the far-field τ_3 axis. A neutral point occurs at 1.56 radii from the edge of the borehole in this direction. **b:** The magnitude of τ_1 around the hole is plotted as contours. The blue line indicates the concentration of τ_1 plotted in (a). **c:** Contours show the magnitude of τ_3 around the hole. The magenta line indicates the concentration of τ_3 shown in (a). **d:** The radial τ_r and tangential τ_θ stress magnitudes are plotted along the far-field τ_3 axis, as in (a). When comparing (a) and (d), we observe that at the neutral point, the principal stresses, in relation to the radial and tangential stresses, undergo a reversal. **e:** Contours represent the radial stress magnitude in space around the hole. The line drawn is blue near the borehole where the radial stress is the least principal stress. At the neutral point, however, the line is changed to magenta to indicate that the radial stress is the least principal stress at this distance. **f:** Contours represent the tangential stress magnitude around the hole. The line drawn is magenta near the borehole, illustrating that the tangential stress is the maximum principal stress there. At the neutral point, the line is changed to blue, corresponding to the stress reversal, where the tangential stress is then the maximum principal stress.

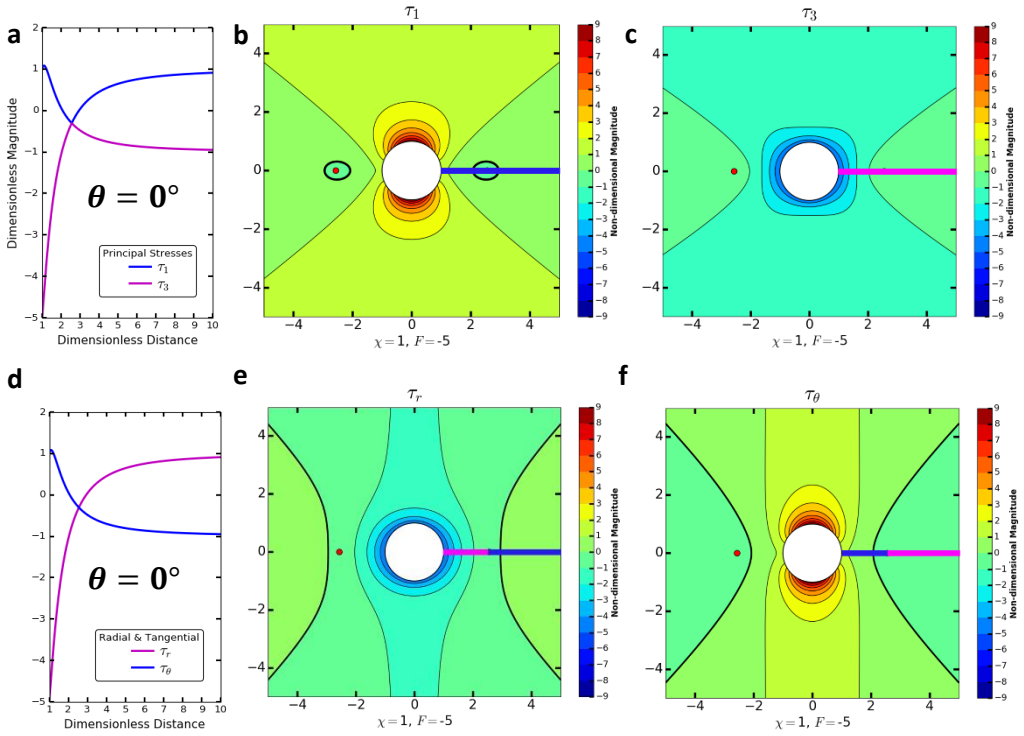

Figure 14: Solutions are along the τ_1 principal axis (θ=0º) for bi-axial plane stress (χ=1) and underbalanced pressure (F=-5) conditions. **a:** The magnitude concentrations of τ_1 and τ_3 are plotted along the far-field τ_1 axis. A neutral point occurs at 1.56 radii from the edge of the borehole in this direction. **b:** The magnitude of τ_1 around the hole is shown as contours. The blue line indicates the concentration of τ_1 plotted in (a). **c:** Contours show the magnitude of τ_3 around the hole. The magenta line indicates the concentration of τ_3 shown in (a). **d:** The radial τ_r and tangential τ_θ stress magnitudes are plotted along the far-field τ_1 axis, as in (a). When comparing (a) and (d), we observe that at the neutral point, the principal stresses, in relation to the radial and tangential stresses, undergo a reversal. **e:** Contours represent the radial stress magnitude in space around the hole. The line drawn is magenta close to the borehole where the radial stress is the least principal stress. At the neutral point, the line is changed to blue to indicate that the radial stress is the maximum principal stress. **f:** Contours represent the tangential stress magnitude around the hole. The line drawn is blue close to the borehole to show that there the tangential stress is the maximum principal stress. At the neutral point, the line is changed to magenta to illustrate the stress reversal, where the tangential stress is then the least principal stress.

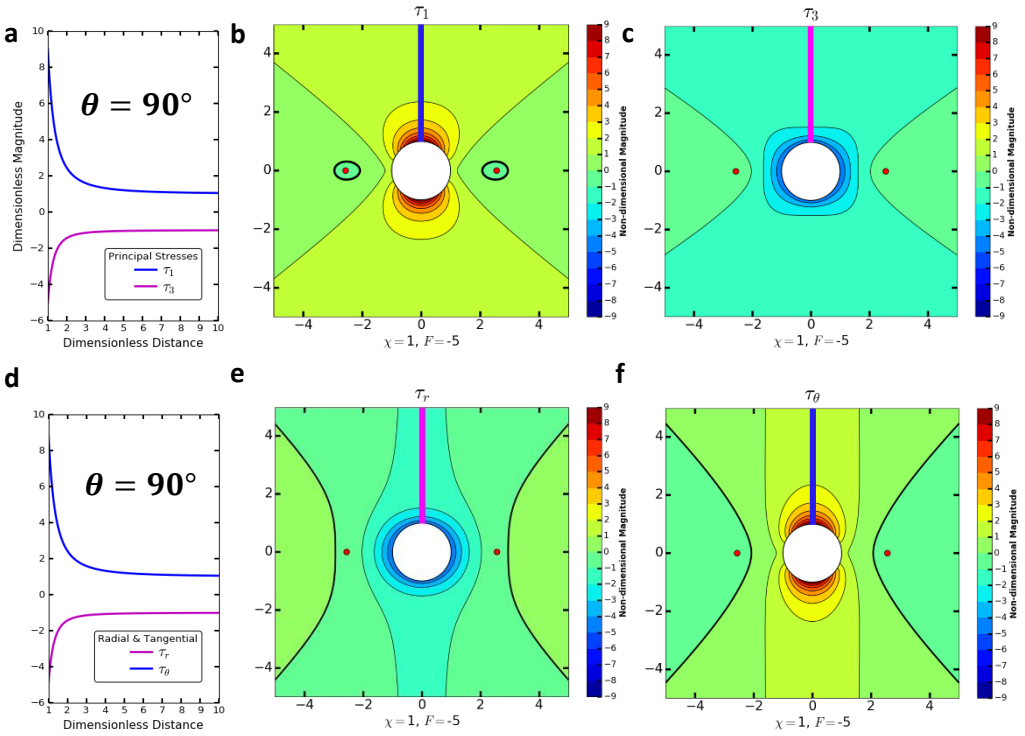

Figure 15: Solutions are along the τ_3 principal axis (θ=90º) for bi-axial plane stress (χ=1) and underbalanced pressure (F=-5) conditions. **a:** The magnitude concentrations of τ_1 and τ_3 are plotted along the far-field τ_1 axis. **b:** Magnitude contours of τ_1 around the hole. The blue line indicates the concentration of τ_1 shown in (a). **c:** Contours representing the magnitude of τ_3 around the hole. The magenta line indicates the concentration of τ_3 shown in (a). **d:** The radial τ_r and tangential τ_θ stress magnitudes are plotted along the far-field τ_3 axis, as in (a). e: Contours represent the radial stress magnitude around the hole. The line drawn is magenta to indicate that along that entire principal axis, the radial stress is the least principal stress. **f:** Contours represent the tangential stress magnitude around the hole. The line drawn is blue to indicate that along that entire principal axis, the tangential stress is the maximum principal stress.

5. STRESS CAGE

A positive Frac Number is indicative of locally overbalanced ($P_{NET} > 0$) borehole conditions. As *F* becomes more and more positive, corresponding to a positive increase in P_{NET}, the directions of τ_1 and τ_3 (largest and smallest principal deviatoric stresses, respectively) interchange near the wellbore. The region bounding the points where this reversal of stress orientations occurs is known as the 'stress cage'. The effect has been recognized only in a few earlier related studies (Weijermars et al., 2012, 2013a). The result of the stress reversal is that, near the wellbore (inside the stress cage region), *all radial stresses are compressional*, even in the direction of the far field tension stress. The isotropic points outline the precise location of the elliptical region around the wellbore where principal stress reversals occur with respect to the far-field stresses. The two aligned principal stresses, τ_1 (compression near the wellbore) and τ_3 (far field tension), are separated by isotropic or neutral points (seen as red dots in Figs. 12b). The stress cage is bounded by a τ_3 trajectory that circumnavigates the entire borehole, passing through both neutral points. Within this elliptical region, tension fractures can form only in the radial planes. Breakout is unlikely as long as τ_3 trajectories follow fully-closed, curved surfaces in the immediate vicinity of the wellbore (forming a stress cage), with potential slip direction solutions precluding movement of such rock breakout (Fig. 16a).

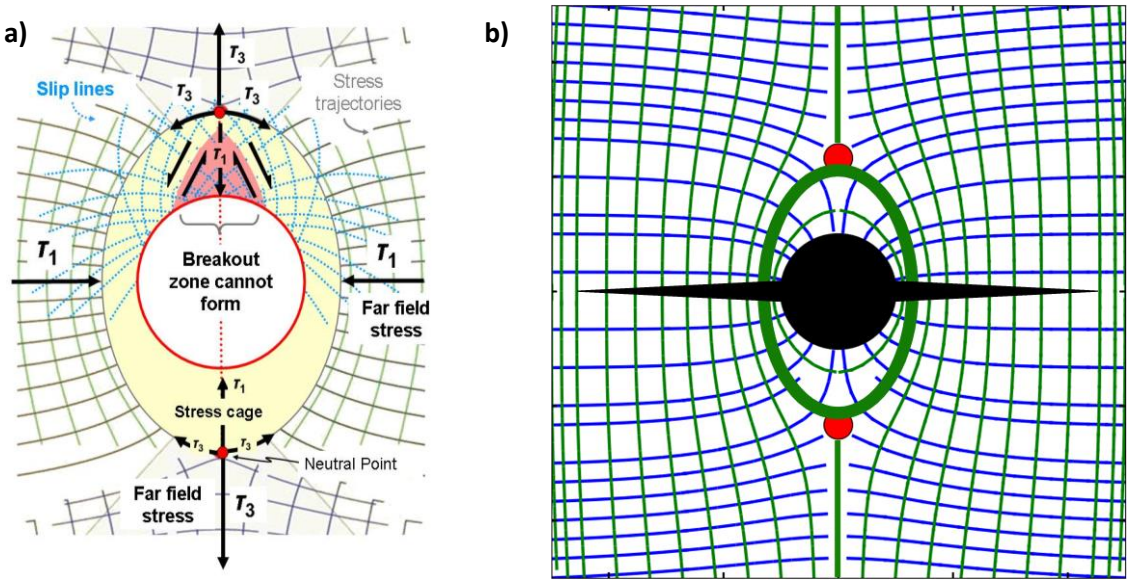

Figure 16 a: Slip line solutions in an overbalanced wellbore are not preferentially aligned for shear failure. Only tensile failure is likely. Reprinted from Weijermars and Schultz-Ela (2015). **b:** Bi-winged fractures propagating in an overbalanced (F=4) borehole.

Formation stress determines borehole integrity. If the stress holding the hole closed is less than the pressure trying to open it, then the hole opens (induced fracture), which causes lost circulation and lost returns. The formation of stress cages in overbalanced wellbores is a mechanism where the opening of initial tension fractures (and any proppant emplacement; Fig. 16a) leads to a change in the hoop stress. The change of the stress state due to stress caging is a drop in tensional hoop stress. The reduction of hoop stress (less tension) makes the formation of additional tensional fractures inside the stress cage more difficult. Previous studies have stated that hoop stress, after stress caging, would be increased compression (Tovar and Bhat, 2011), which is not supported by this study. Consequent to the stress cage concept (Ito et al., 1999; Alberty and McClean, 2004; Wang et al., 2008; Tovar and Bhat, 2011), and the earlier work by Haimson and Fairhurst (1968),

tension fractures commonly form as two diametrically opposed fracture branches known as “bi-wing” fractures (Fig. 16b).

Bi-winged tension fractures typically form when a tectonic far-field stress superimposes a bi-axial anisotropy of stresses around the wellbore. Weijermars (2016) argued that deviations, including multiple fractures, are plausible for higher Frac Numbers. For example, the tangential tension stresses due to the shock wave ($F \rightarrow +\infty$) in a previously stress-free plexiglass plate hit by a bullet may create a ‘starburst’ pattern of tension fractures (Fig. 17a). Likewise, tension fractures formed around vertical volcanic pipe intrusions are known to emanate outward in multiple radial directions (Muller, 1986; Muller and Pollard, 1977; Koenig and Pollard, 1998) that are not necessarily bi-winged (Fig. 17c). The same is true for radially expanding salt diapirs (Caruthers, 2012; Fig. 17b). In addition to the Frac Number, speed of injection may also play a role in favoring either bi-winged or multi-branched starburst tension failure. Although multi-winged tension fractures are most-likely to occur for very large Frac Numbers ($F \rightarrow +\infty$), multi-branched radial tension fractures may form for intermediate Frac Numbers ($0 << F < +50$) when the rate of injection is very high. Note, however, that multi-branched fractures do not appear on Formation Micro-imager (FMI) logs.

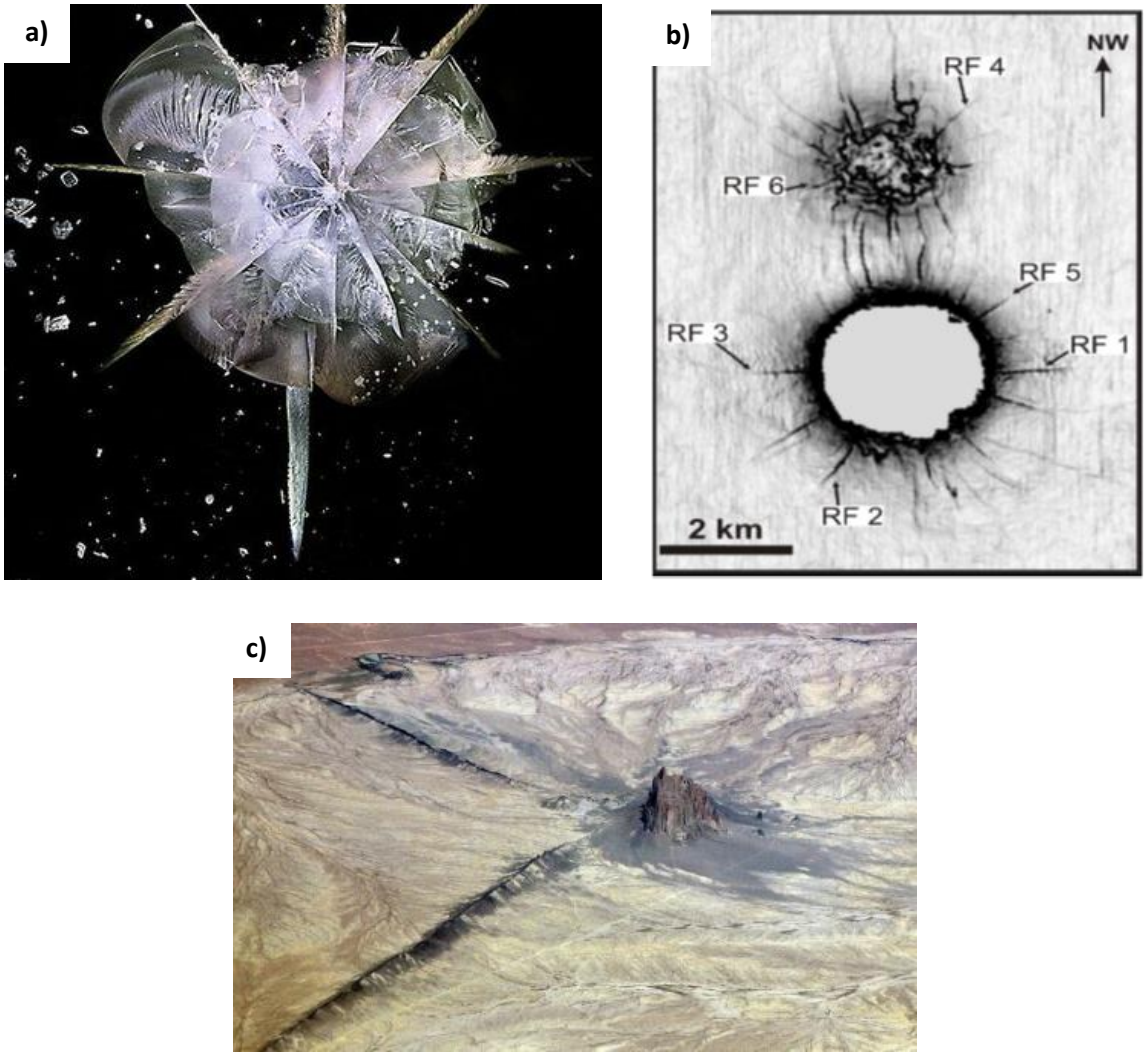

Figure 17 a: A bullet hitting bulletproof glass creates a starburst pattern. Reprinted from Bay (2017). **b:** Radial fractures (RF1-6) in the roof of the Pierce salt stocks, North Sea basin. Reprinted from Carruthers (2012). **c:** Radial dikes emanating from central magma feeder stock now exposed after uplift and erosion and known as Shiprock Mountain, New Mexico.

We analyze the stress cage effect by first observing the tangential and radial stress magnitude contours (Section 5.1) around a borehole – first for uniaxial far-field stress conditions (χ=0) and then for bi-axial plane stress conditions (χ=1) – for Frac Numbers between $0 \leq F \leq +5$. We will then compare these with the deviatoric principal stress contours

(Section 5.2), again for χ=0, first, and then for χ=1. For supplemental understanding, the differential deviatoric principal stress ($\tau_1 - \tau_3$) magnitudes are shown in Section 5.3. Finally, we will tie in what we have observed in the stress magnitude contour plots with the principal stress trajectories (Section 5.4). The same structure is then reproduced in Section 6 for to illustrate the fracture cage mechanism when a wellbore is underbalanced (F<0)

5.1 Tangential and radial stresses

When a hole is drilled in stressed rock, the stress attempts to close the hole in the radial direction, which can reduce the borehole diameter by a few thousandths of an inch. As the diameter shrinks, the circumference is compressed tangentially (increase in hoop stress). The diameter of the hole stops declining when the tangential stress (hoop stress) balances the radial stress. If the tangential stress exceeds the rock strength before the stresses come to equilibrium, the rock breaks and the hole enlarges. If the tangential stress does not exceed the rock strength, there is no breakout and the hole remains gauge. A driller lowers the tangential stress by increasing the internal pressure (mud weight), which expands the circumference of the hole. Under uniaxial far-field stress conditions, when a borehole net fluid pressure is balanced (F=0), an increased concentration of compressive tangential stress exists at the wellbore rim in the direction of τ_3 (Fig. 18; Left), which is the preferred direction of breakout.

The following set of figures characterizes the tangential and radial stress concentrations in space around a borehole that has been drilled into rock exhibiting a

uniaxial far-field boundary stress (Figs. 18-24) and then when it is subjected to a planar bi-axial far-field stress (Figs. 25-31). We will assume that initially, the borehole net pressure is balanced (F=0). In reality, the Frac Number could potentially be negative when the hole is cut into the rock. When the borehole is initially drilled, a highly compressive tangential stress occurs in the direction of the least principal stress, which precludes any shear failure including breakout. In order to prevent such instabilities, a driller increases the mud weight (increases the F-value), which expands the borehole, lowering the magnitude of the tangential stress. As the F-value continues to increase by increasing the mud weight, or possibly because the formation pressure unexpectedly decreases drastically, the tangential stress reduces more and more, exhibiting highly anisotropic behavior (i.e., highly tensional stress concentrations in the τ_1 direction with much less extreme stress concentrations in the τ_3 direction). In contrast, the radial stress increases positively (compressively) rather uniformly around the borehole with a slight peak concentration in the τ_3 direction.

Under uniaxial far-field stress conditions, when the borehole is initially drilled (assume F=0), the radial stress around a borehole is considerably weak, with a slight peak in the τ_1 direction. However, as F becomes larger positively (more overbalanced), the maximum stress concentration reverses and becomes aligned with the τ_3 direction, corresponding to the stress reversal that occurs within the stress cage associated with overbalanced (F>0) wellbores. As the *F*-value increases to *F*=1 (Figs. 19), the tangential stress is everywhere reduced, becoming less compressive (i.e., less positive) in the τ_3 direction and more tensional (i.e., more negative) in the τ_1 direction. When F=2 (Figs. 20),

the tangential stress at the wellbore wall is everywhere less compressive than far-field conditions, with a large tensional concentration in the τ_1 direction. In all orientations, the radial stress concentration at the wellbore is more compressive than far-field stress. At F=3 (Figs. 21), the tangential stress at the borehole wall is negative (tensional) in all orientations. For larger F-values (e.g., F=4,5 and up to F=+∞), the tangential stress becomes progressively more tensional, and larger regions around the borehole become susceptible to tensional failure [i.e., the width where τ_θ is negative (tensional stress) grows around the wellbore]. This corresponds to the growing stress cage witnessed in the stress trajectory plots (Figs. 22-26).

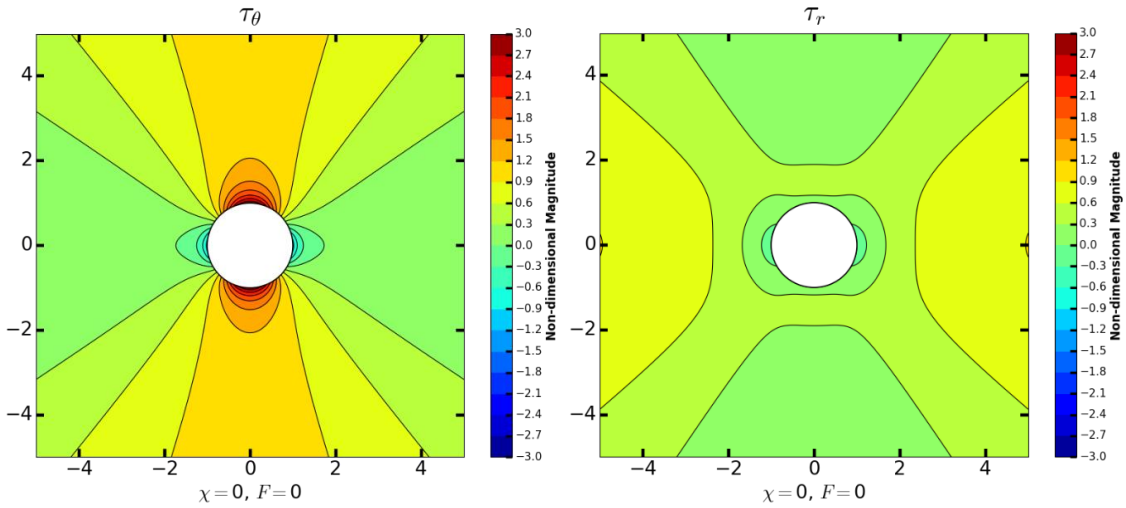

Figure 18: χ=0 (uniaxial far-field stress) and F=0 (balanced borehole net pressure). A highly compressive tangential stress concentration exists in the τ_3 direction (three times as compressive as far-field τ_1). The radial stress is reduced near the borehole. Compressive failure is likely to occur, depending on the strength of the rock. Increase mud weight (increase F) to avoid break out.

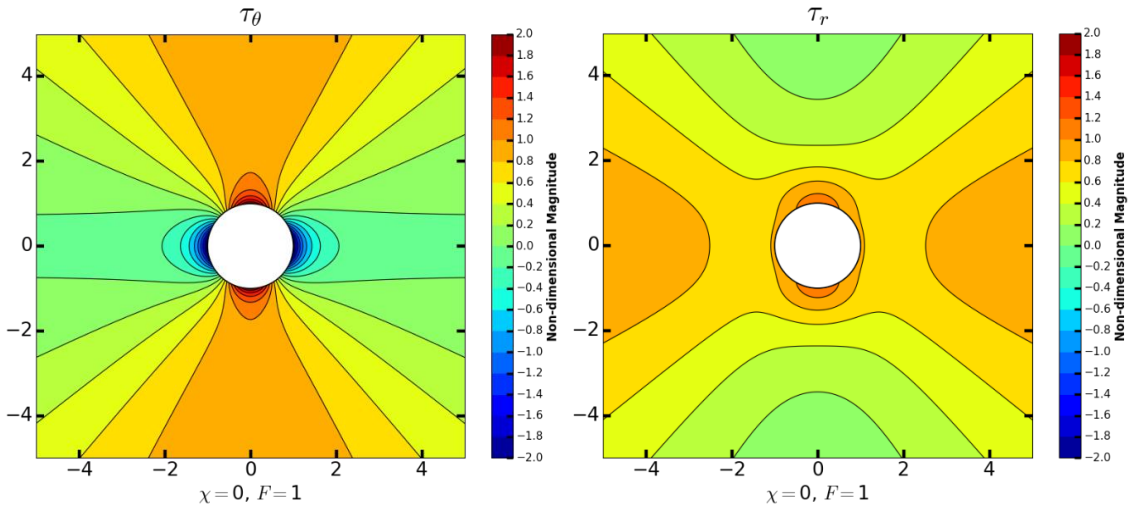

Figure 19: χ=0 (uniaxial far-field stress) and F=1 (borehole net pressure is overbalanced and proportional in compressive magnitude to far-field τ_1). The tangential stress is reduced in all orientations (recall we lower tangential stress to prevent breakout failure by increasing mud weight) and is still positive (compressive) in the τ_3 direction and more negative in the τ_1 direction.

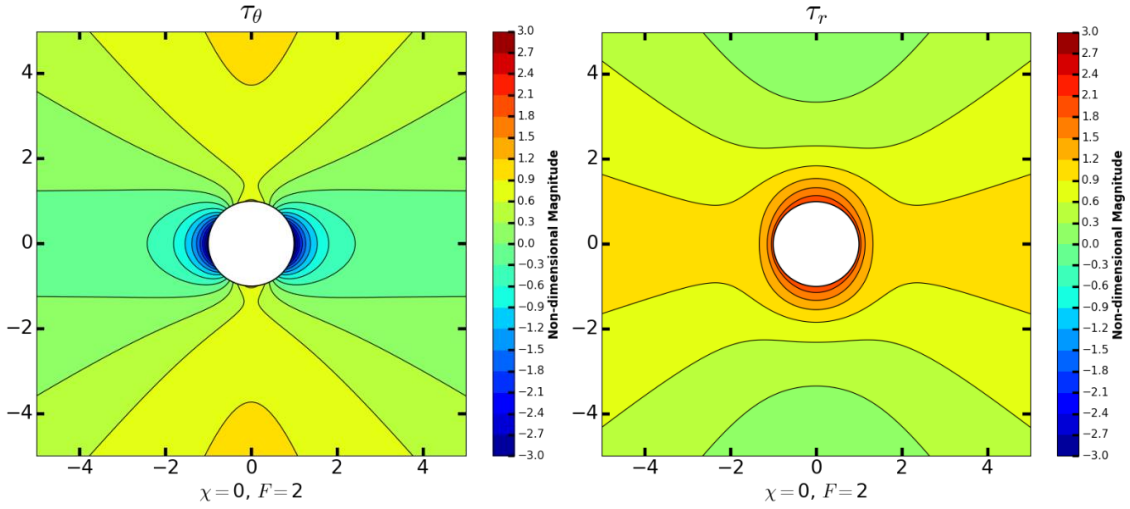

Figure 20: χ=0 (uniaxial far-field stress) and F=2 (borehole net pressure is overbalanced and two times as compressive in magnitude as far-field τ_1). The tangential stress is still slightly compressive in the direction of τ_3, although it is now less compressive than at far-field conditions, and in the direction of τ_1, the tangential stress concentration is considerably tensional (-3 times far-field τ_1). The radial stress is much more evenly distributed around the wellbore rim than the tangential stress which exhibits highly anisotropic stress concentrations.

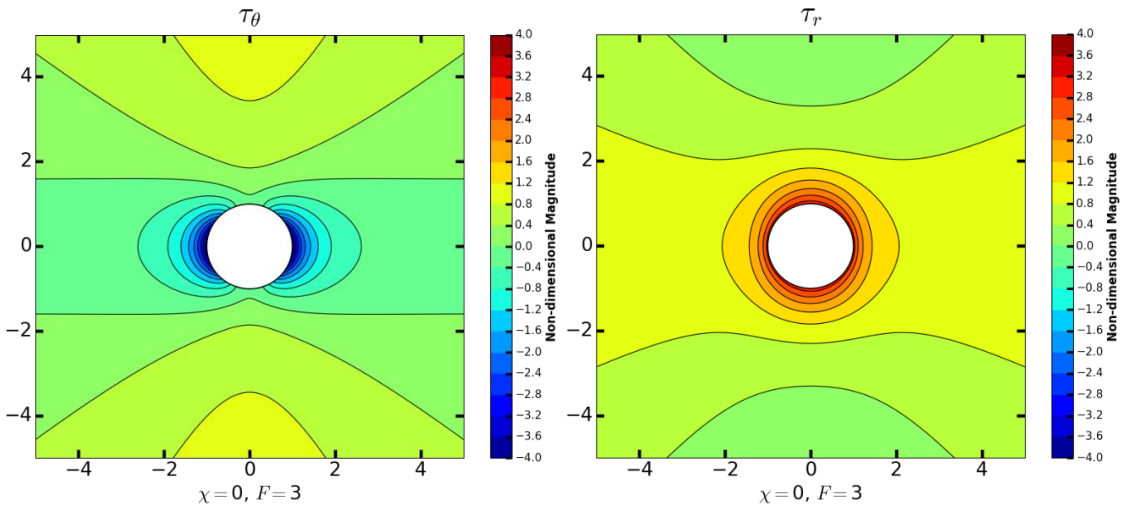

Figure 21: χ=0 (uniaxial far-field stress) and F=3 (borehole net pressure is overbalanced and three times as compressive in magnitude as far-field τ_1). The area along the borehole wall where the tangential stress is still compressive no longer exists. The tangential stress is negative around the entire hole, with high tensional stress concentrations in the τ_1 direction. The compressive radial stress is fairly evenly distributed around the borehole rim, with slight peaks in the τ_3 directions.

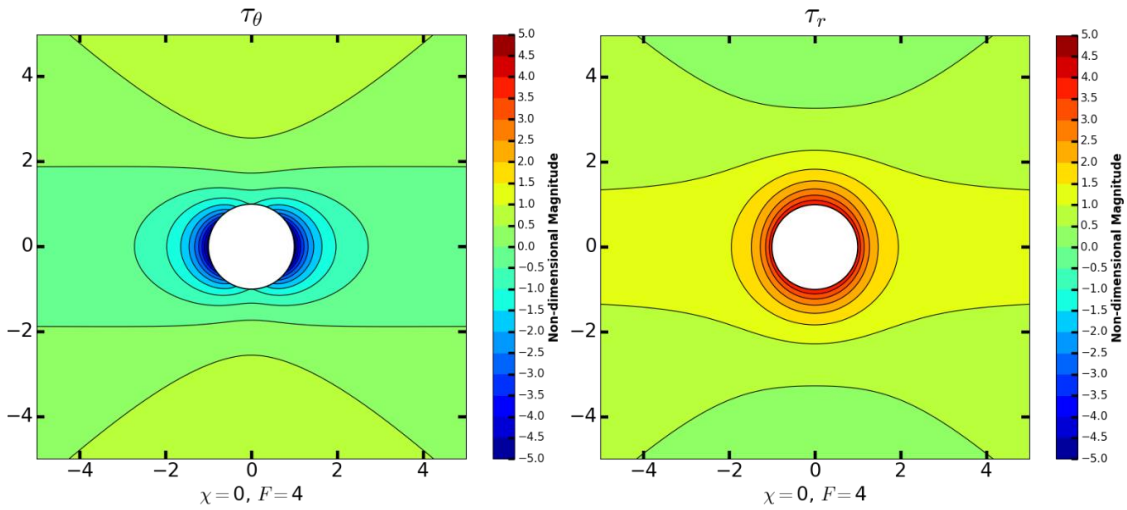

Figure 22: χ=0 (uniaxial far-field stress) and F=4 (borehole net pressure is overbalanced and four times as compressive in magnitude as far-field τ_1). The tangential stress becomes more tensional, particularly in the τ_1 direction and the radial stress continues to increase in magnitude compressively. The radial stress is quite evenly distributed around the borehole, not displaying the high anisotropic stress concentrations that we see of the tangential stress. Due to the large tensional stress concentrations exhibited by the tangential stress, tensional failure is likely to occur.

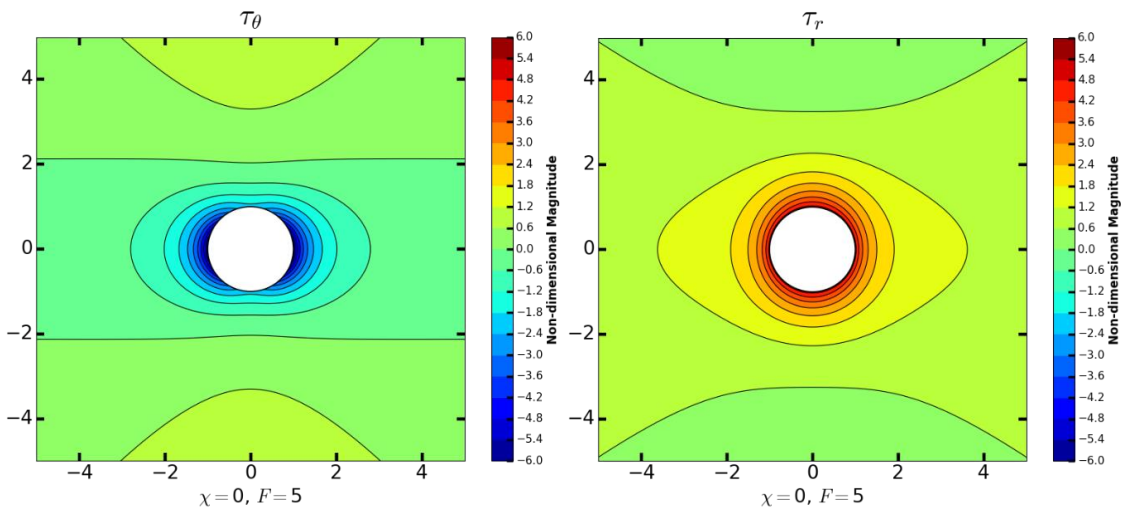

Figure 23: χ=0 (uniaxial far-field stress) and F=5 (borehole net pressure is overbalanced and five times as compressive in magnitude as far-field τ_1). The region where tensile failure is likely to occur (due to tangential stress reaching tensile strength) nearly reaches all the way around the wellbore. If rapid injection occurred in such a way to increase borehole net pressure this rapidly, tensional failure could occur from several discrete locations around the wellbore wall, rather than forming the typical bi-winged fractures we're familiar with (see Fig. 12b). Note also how evenly distributed the radial stress is around the borehole compared to the high anisotropy displayed by the tangential stress.

Under bi-axial far-field stress conditions, when the borehole net fluid pressure is balanced (F=0), an increased concentration of compressive tangential stress exists at the wellbore rim in the direction of τ_3 (Fig. 20), which is the preferred direction of breakout. When the borehole is initially opened (F=0), the tangential and radial stress contours show extraordinarily balanced patterns. If we naturally divide the contours of Fig. 24 into four triangles divided by the diagonal contour lines, we see that the top and bottom triangles are perfect rotations of the triangles on the sides of the borehole, multiplied by -1 (i.e., the compressive magnitudes in the top and bottom triangles are equal in magnitude but

opposite in sign to the tensional magnitudes at the sides of the borehole). As the *F*-value increases to *F*=1 (Figs. 25), the tangential stress is everywhere reduced, becoming less compressive (i.e., less positive) in the τ_3 direction and more tensional (i.e., more negative) in the τ_1 direction. When $2 \leq F \leq 3$ (Figs. 26, 27), the tangential stress is still compressive in increasingly small regions in the τ_3 direction and exhibits large tensional concentrations in the τ_1 directions. In all orientations, the radial stress concentration at the wellbore is more compressive than far-field stress. At F=4 (Figs. 28), the compressive tangential stress concentration has vanished at the borehole wall and τ_θ is tensional in every direction from the hole. For larger F-values (e.g., F=5 and up to $F=+\infty$), the tangential stress becomes progressively more tensional, and larger regions around the borehole become susceptible to tensional failure (i.e., the width where τ_θ reaches tensile strength of the rock grows around the wellbore). This corresponds to the growing stress cage witnessed in the stress trajectory plots (Figs. 44 & 45).

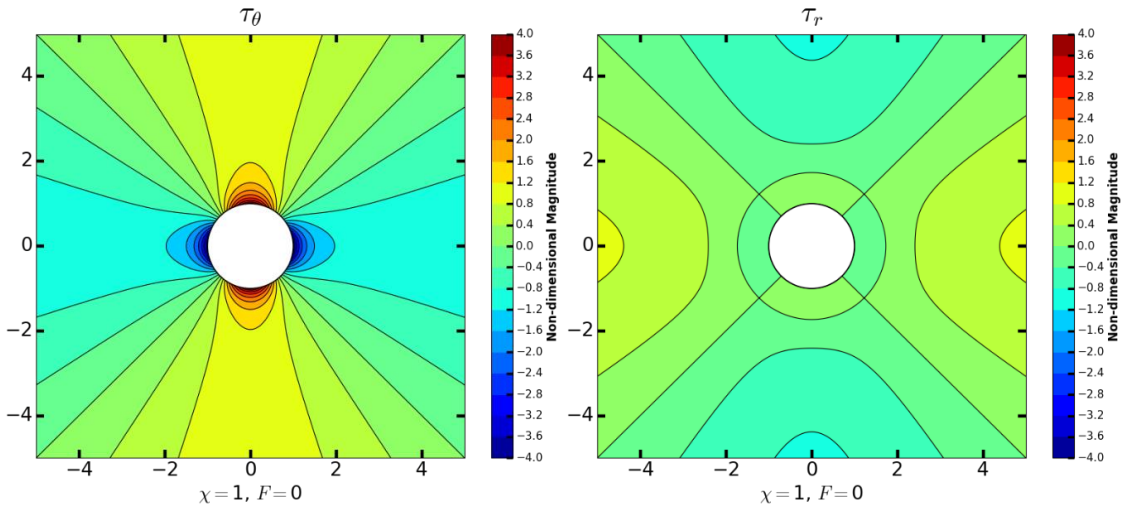

Figure 24: χ=1 (bi-axial far-field stress) and F=0 (balanced borehole net pressure). A highly compressive tangential stress concentration exists in the τ_3 direction (four times as compressive as far-field τ_1). The radial stress is reduced near the borehole. Compressive failure is likely to occur, depending on the strength of the rock. Increase mud weight (increase F) to lower the tangential stress to avoid break out.

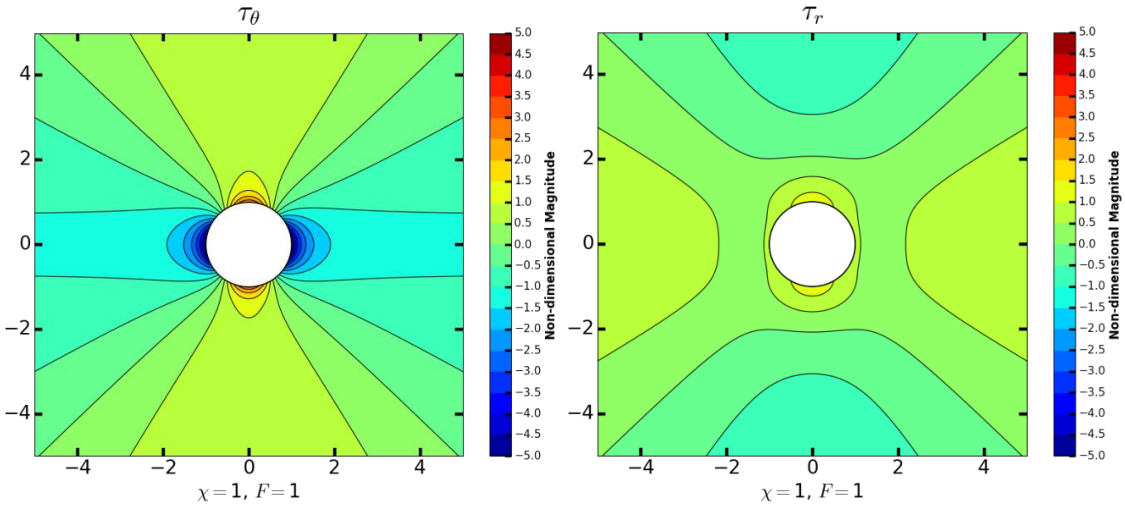

Figure 25: χ=1 (bi-axial far-field stress) and F=1 (borehole net pressure is overbalanced and proportional in compressive magnitude to far-field τ_1). The tangential stress is reduced in all orientations (recall we lower tangential stress to prevent breakout failure by increasing mud weight) and is still positive (compressive) in the τ_3 direction and more negative in the τ_1 direction. The most-compressive region for the radial stress has consolidated into a finer region above and below the borehole (τ_3 direction).

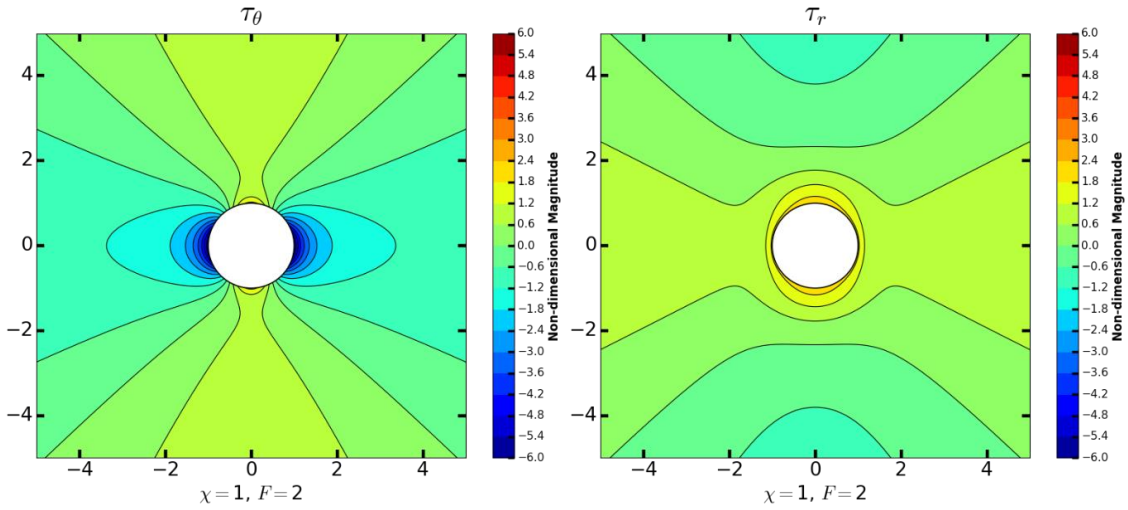

Figure 26: χ=1 (bi-axial far-field stress) and F=2 (borehole net pressure is overbalanced and two times as compressive in magnitude as far-field τ_1). The tangential stress is still slightly compressive in the direction of τ_3, and in the direction of τ_1, the tangential stress concentration is considerably tensional (-6 times far-field τ_1). The radial stress is much more evenly distributed around the wellbore rim than the tangential stress which exhibits highly anisotropic stress concentrations.

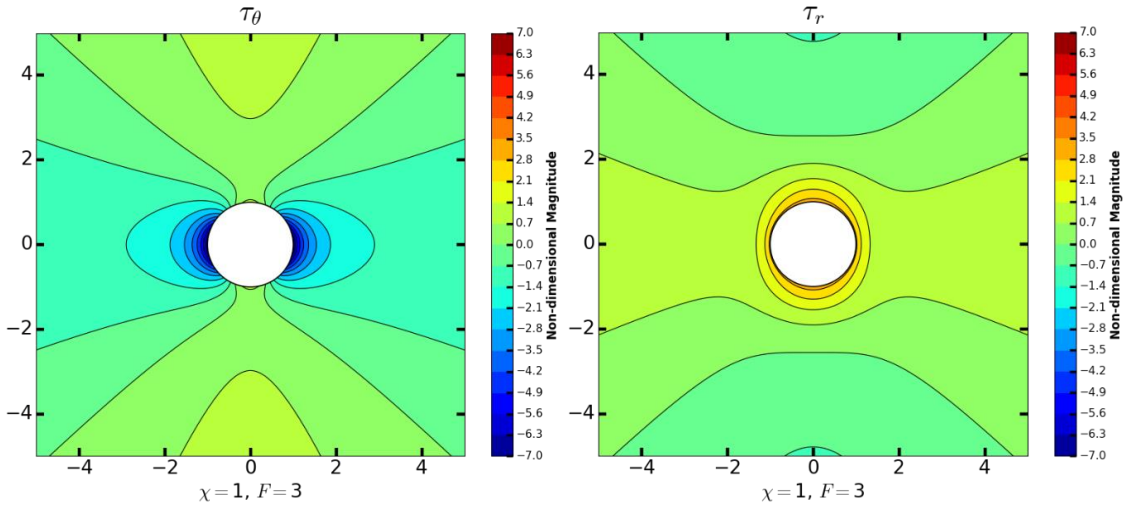

Figure 27: χ=1 (bi-axial far-field stress) and F=3 (borehole net pressure is overbalanced and three times as compressive in magnitude as far-field τ_1). A small region in the direction of τ_3 still exists at the wellbore wall where the tangential stress is compressive. Around the remainder of the borehole, the tangential stress is negative, with high tensional stress concentrations in the τ_1 direction. The compressive radial stress is fairly evenly distributed around the borehole rim, with slight peaks in the τ_3 directions.

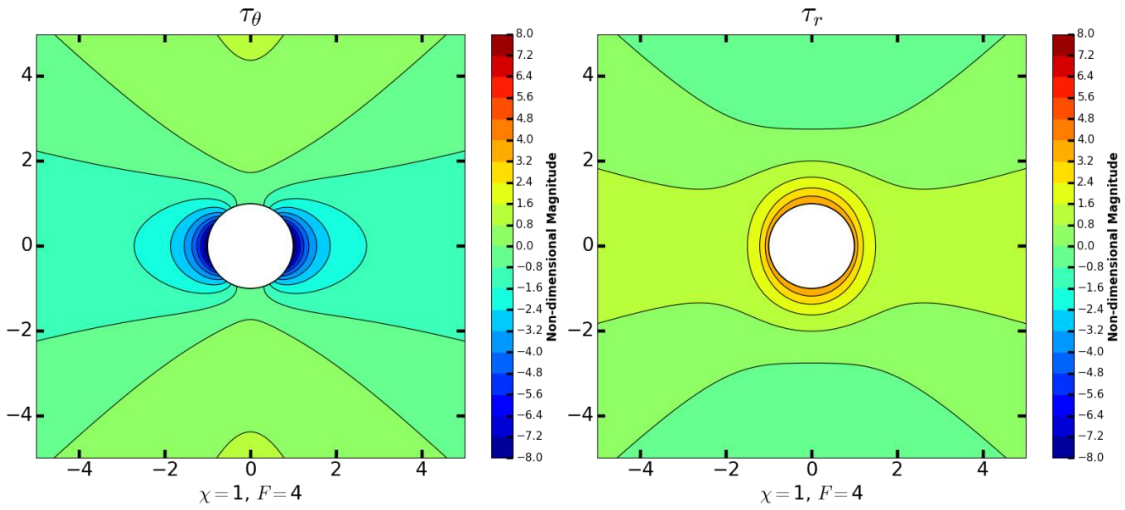

Figure 28: χ=1 (bi-axial far-field stress) and F=4 (borehole net pressure is overbalanced and four times as compressive in magnitude as far-field τ_1). The tangential stress is now tensional (negative) in all directions at the borehole wall. The radial stress continues to increase in magnitude compressively. Due to the large tensional stress concentrations exhibited by the tangential stress, tensional failure is likely to occur.

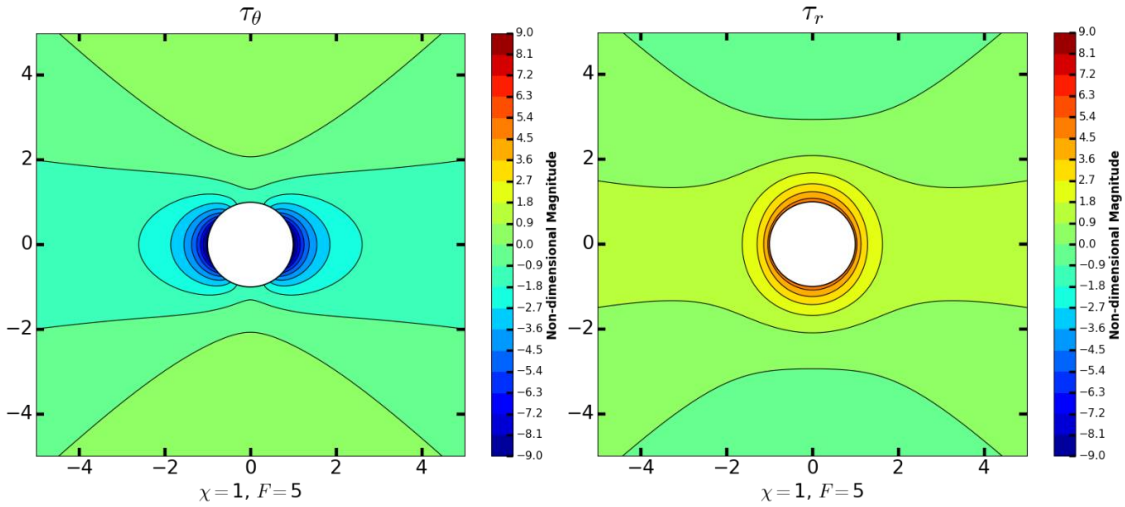

Figure 29: χ=1 (bi-axial far-field stress) and F=5 (borehole net pressure is overbalanced and five times as compressive in magnitude as far-field τ_1). The region where tensile failure is likely to occur (due to tangential stress reaching tensile strength) nearly reaches all the way around the wellbore. If injection occurs in such a way as to increase borehole net pressure rapidly, tensional failure could occur from several discrete locations around the wellbore wall, rather than forming the typical bi-winged fractures we are familiar with (see Fig. 16b).

If tensional failure occurs in a larger stress cage (due to strong tensile strength of rock), what could be the effect on fracture geometry? Even when there is a far-field stress, fractures may initiate at multiple locations as a discrete point of tensional stress concentration. Failure initiation sites blur into a wider region for larger borehole net pressures. If episodic injection occurs at a rapid rate, and if the tensile strength is large enough to prevent tensile failure until the Frac Number is very high, multi-winged fractures analogous to when a bullet hits plexiglass (Fig. 17a), or around a radially-expanding salt diaper (Fig. 17b), are possible.

5.2 Principal Deviatoric Stress

The principal deviatoric stress non-dimensional magnitudes are plotted as contours in the subsequent set of figures to show their relationship to the tangential and radial stresses. Along the principal axes (e.g., τ_1 is oriented along the horizontal axis and τ_3 is along the vertical axis), the principal stresses will be perfectly related to the radial and tangential stresses. Outside of these preferential axes, there will be some deviation between the principal stress magnitudes and the radial and tangential stress magnitudes. A general pattern is observed between the two sets of figures, however, and we can observe governing characteristics between the two types of stresses. In the non-dimensional principal stress contour plots, the neutral points are readily observed, unlike in the radial and tangential stress contour plots. For $F \geq 2$, the neutral points can be discerned by comparing the τ_1 contours with the τ_3 contours, looking for a region above and below the hole (direction of τ_3) where the magnitudes are equal. Typically, in one or

both contour plots, there exists a small circular contour close to the region where the neutral point occurs.

Initially, when the hole is first cut into the rock (F=0), the maximum principal stress τ_1 is very similar to the tangential stress (Fig. 18, 30) and the minimum principal stress τ_3 relates to the radial stress. However, as the net borehole pressure increases to F=2, we observe the stress reversal associated with the stress caging mechanism, and τ_1 relates to the radial stress and τ_3 to the tangential stress. This remains true for large positive Frac Numbers also.

For $F \geq 2$, the neutral points occur along the τ_3 axis, at equal distances on opposite sides of the borehole. Looking at the τ_3 non-dimensional magnitude contours (Figs. 32-35), for larger F-values, the neutral points occur further away from the borehole. Accordingly, a region where compressive stress still occurs for τ_3 moves further away from the borehole, and the width around the borehole where τ_3 is tensional, correspondingly grows.

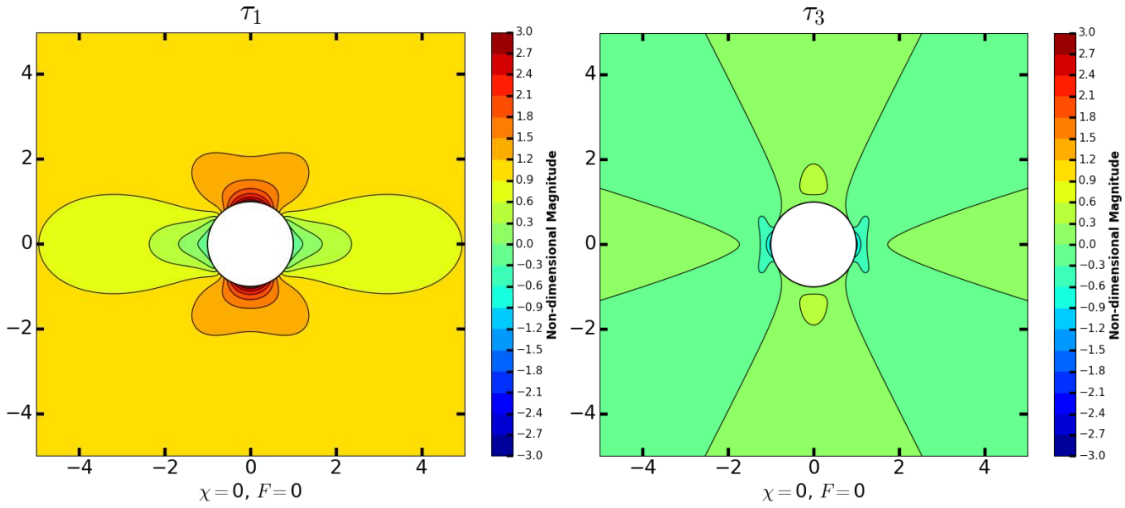

Figure 30: χ=0 (uniaxial far-field stress) and F=0 (balanced borehole net pressure). Observe that in this initial state, the maximum principal stress τ_1 has similar orientation and magnitude as the tangential stress, and the minimum principal stress τ_3 is similar to the radial stress. Four neutral points occur along the wellbore wall (see Fig. 44a). The magnitudes of τ_1 and τ_3 are very close to each other near the wellbore wall in the τ_3 direction (θ=0º).

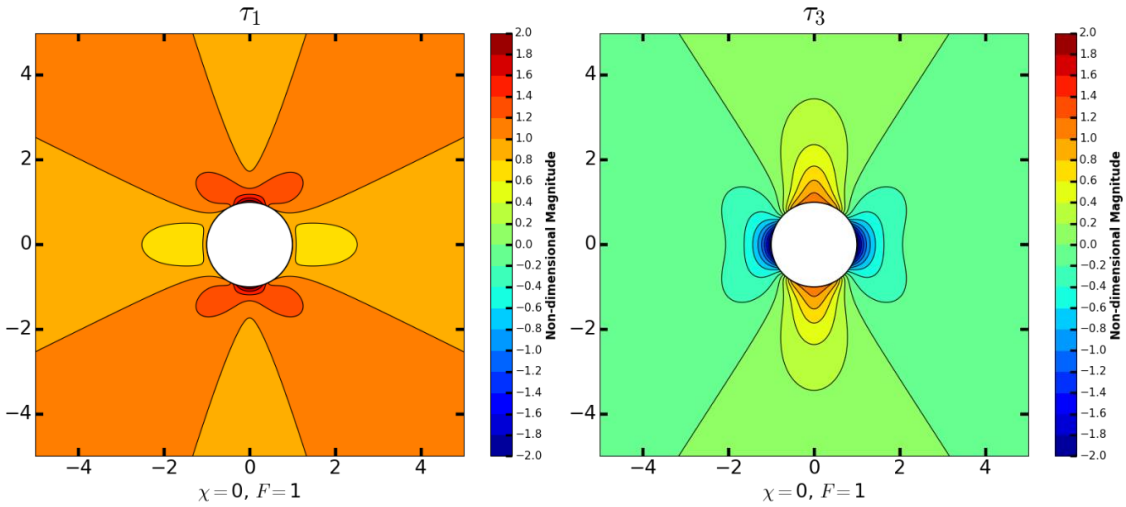

Figure 31: χ=0 (uniaxial far-field stress) and F=1 (borehole net pressure is overbalanced and proportional in compressive magnitude to far-field τ_1). The maximum principal stress τ_1 is compressive in all orientations at the borehole rim. Both τ_1 and τ_3 have peak compressive stress concentrations in the τ_3 direction. Four neutral point regions still occur around the wellbore rim, closer together at the top and bottom of the hole in the image than for F=0 (see Fig. 44b).

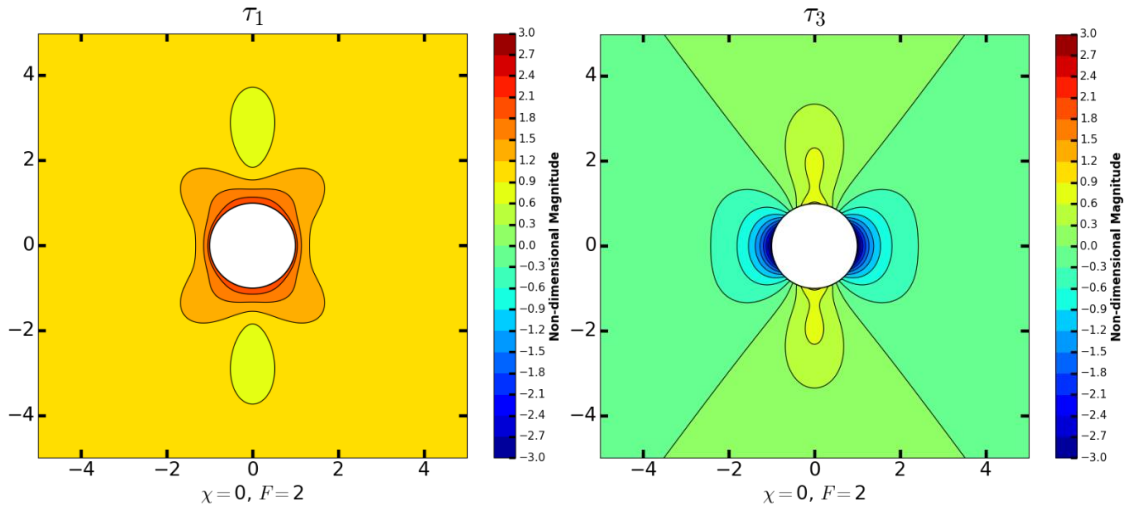

Figure 32: χ=0 (uniaxial far-field stress) and F=2 (borehole net pressure is overbalanced and two times as compressive in magnitude as far-field τ_1). Observe now that the stresses have reversed, and the maximum principal stress τ_1 is now more like the radial stress and the minimum principal stress τ_3 relates to the tangential stress (Fig. 20). Two neutral points occur both above and below the hole for F=2 which could cause serious issues during hydraulic fracturing.

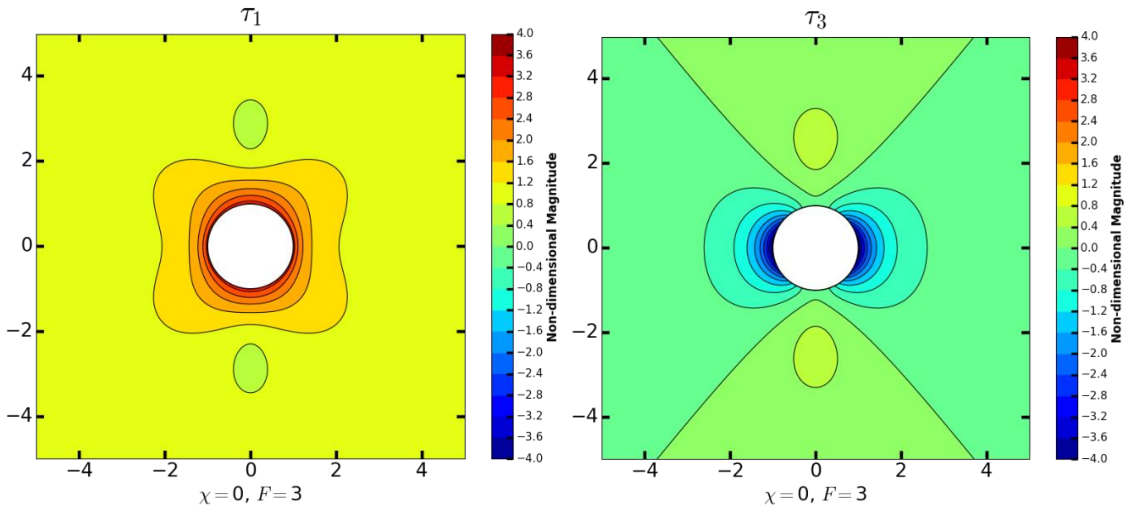

Figure 33: χ=0 (uniaxial far-field stress) and F=3 (borehole net pressure is overbalanced and three times as compressive in magnitude as far-field τ_1). The maximum principal stress τ_1 is similar to the radial stress and the minimum principal stress τ_3 relates to the tangential stress (Fig. 21). Distinct neutral point regions are delineated by small circular contours above and below the hole in the image. The minimum principal stress τ_3 is now tensional at the wellbore wall in all directions.

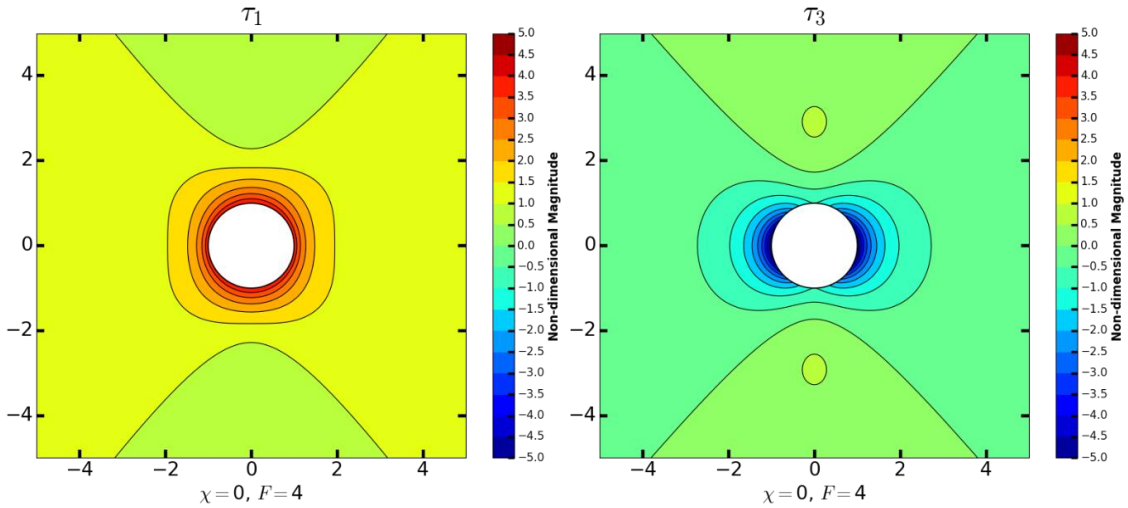

Figure 34: χ=0 (uniaxial far-field stress) and F=4 (borehole net pressure is overbalanced and four times as compressive in magnitude as far-field τ_1). The maximum principal stress τ_1 is similar to the radial stress and the minimum principal stress τ_3 relates to the tangential stress (Fig. 22). Distinct neutral point regions are seen as small circular contours above and below the hole in the image for the τ_3 contours, but are not so easily seen in the τ_1 contours.

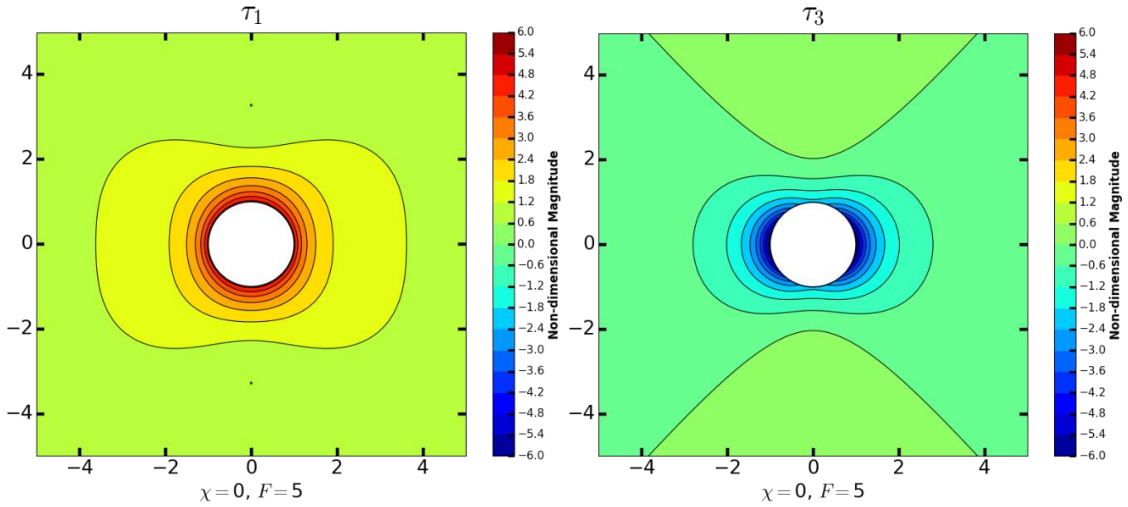

Figure 35: χ=0 (uniaxial far-field stress) and F=5 (borehole net pressure is overbalanced and five times as compressive in magnitude as far-field τ_1). The maximum principal stress τ_1 is similar to the radial stress and the minimum principal stress τ_3 relates to the tangential stress (Fig. 23). Distinct neutral point regions are seen as tiny circular contours above and below the hole in the image for the τ_1 contours, but are not so easily seen in the τ_3 contours.

Under bi-axial planar far-field stress conditions, the compressive τ_1 magnitude contours are a perfect 90º rotation of the tensional τ_3 magnitude contours, having equal magnitude but opposite sign (i.e., if you know the magnitude of τ_3 at a point, multiply it by -1 and rotate its position around the borehole by 90º to know the magnitude of τ_1 at a point. The same is true in reverse. Although the stress magnitude contours of τ_1 are similar for the uniaxial (Fig. 30-35) and the bi-axial plane (Fig. 36-41) stress cases with only slight variations, the magnitude contours for τ_3 vary quite considerably between the two, with much larger negative tension stresses in the τ_1 direction for χ=1. As borehole net pressure increases to F=1, the magnitude of τ_1, at the borehole wall, increases by one normalized unit (normalized by far-field τ_1 magnitude) in the direction of far-field τ_1 (θ=0º) and decreases by one normalized unit of magnitude in the direction of far-field τ_3 (θ=90º). In sharp contrast, the minimum principal stress decreases by one unit of magnitude in the direction of far-field τ_1 (θ=0º) and increases by one normalized unit of magnitude in the direction of far-field τ_3 (θ=90º), effectively increasing the anisotropy between the two far-field orientations.

When F=2, the magnitude of τ_1 has again increased in the direction of far-field τ_1 (θ=0º) and decreased in the direction of the direction of far-field τ_3 (θ=90º), and the magnitude of τ_3 has likewise decreased and increased in these orientations, respectively. What becomes very interesting, is when the Frac Number is increased to F≥3. For these Frac Numbers, the magnitude of τ_1 progressively becomes more positive (compressive) in all orientations, with compressive stress concentrations around the wellbore wall becoming less anisotropic as F increases; and the magnitude of τ_3 becomes progressively

more negative (tensional) in all orientations, with large tensional concentrations in the τ_1 direction, and magnitudes that approach far-field τ_3 stress concentrations in the τ_3 direction. Although neutral points have already realigned along the τ_3-axis when F=2, their exact locations become somewhat apparent when F=3 (Fig. 38), and increasingly apparent for larger F-values (Figs. 39-43).

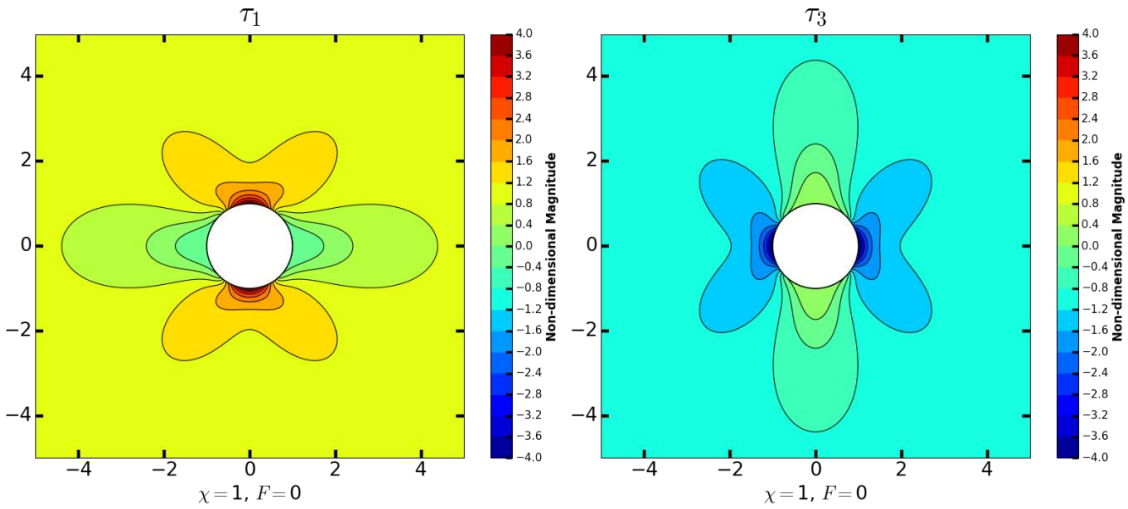

Figure 36: χ=1 (bi-axial far-field stress) and F=0 (balanced borehole net pressure). Observe that in this initial state, the maximum principal stress τ_1 has similar orientation and magnitude as the tangential stress, and the minimum principal stress τ_3 is similar to the radial stress (Figs. 24). Four neutral points occur along the wellbore wall (see Fig. 45a).

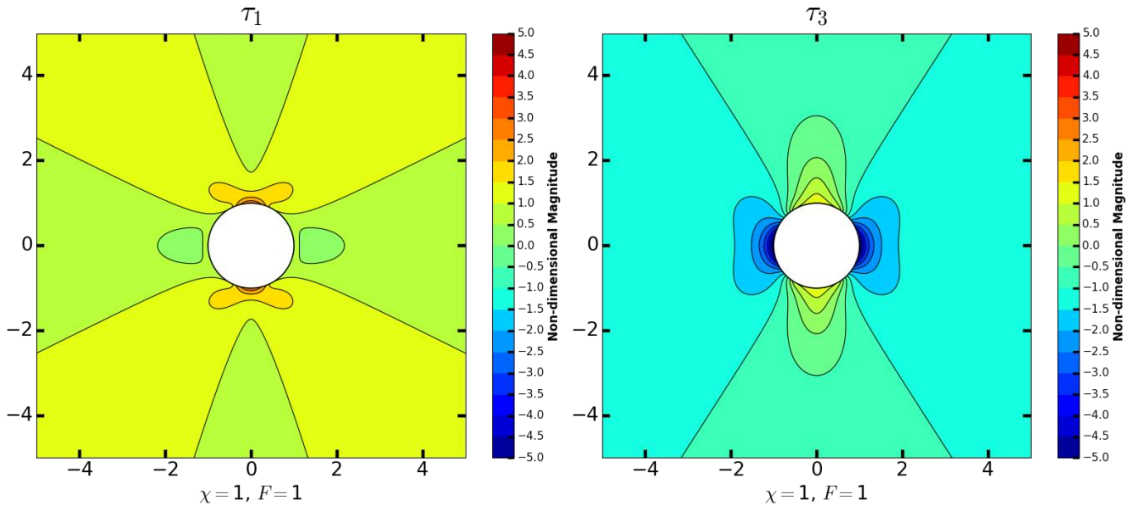

Figure 37: χ=1 (bi-axial far-field stress) and F=1 (borehole net pressure is overbalanced and proportional in compressive magnitude to far-field τ_1). The maximum principal stress τ_1 is compressive in all orientations at the borehole rim. Both τ_1 and τ_3 have peak compressive stress concentrations in the τ_3 direction. Four neutral point regions still occur around the wellbore rim, closer together at the top and bottom of the hole in the image than for F=0 (see Fig. 45b).

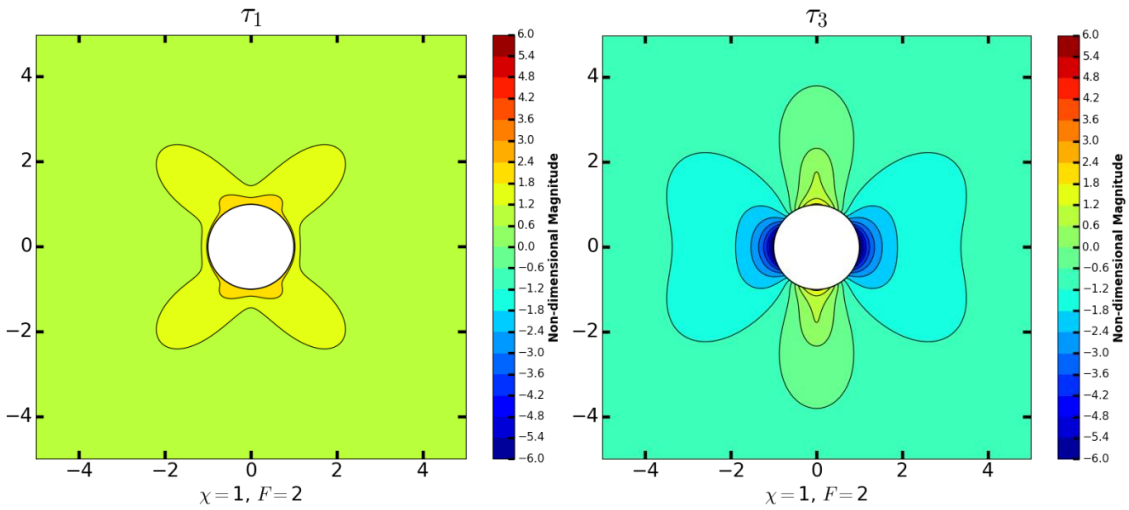

Figure 38: χ=1 (bi-axial far-field stress) and F=2 (borehole net pressure is overbalanced and two times as compressive in magnitude as far-field τ_1). Observe now that the stresses have reversed, and the maximum principal stress τ_1 is now more like the radial stress and the minimum principal stress τ_3 relates to the tangential stress (Fig. 26).

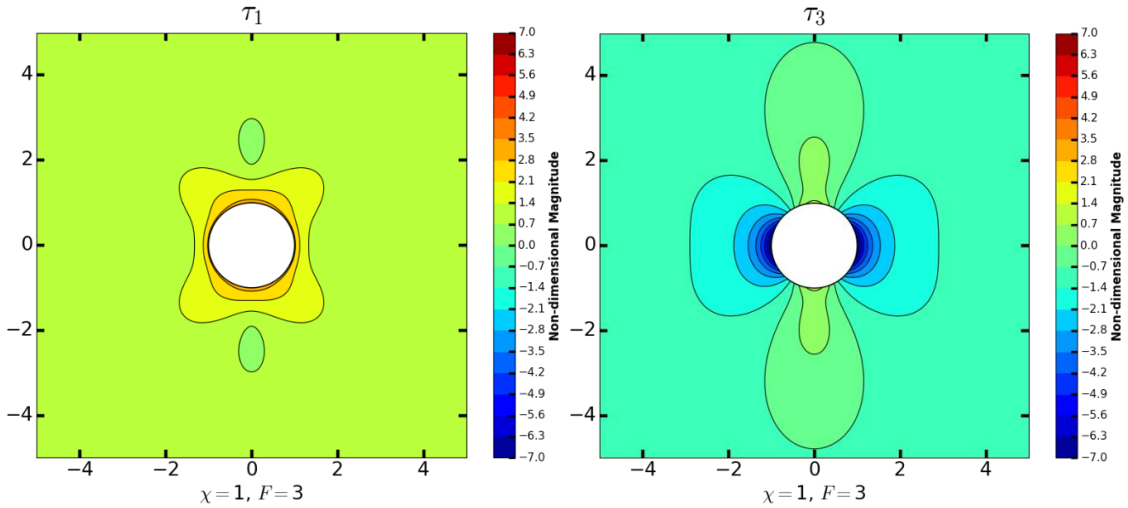

Figure 39: χ=1 (bi-axial far-field stress) and F=3 (borehole net pressure is overbalanced and three times as compressive in magnitude as far-field τ_1). The maximum principal stress τ_1 is similar to the radial stress and the minimum principal stress τ_3 relates to the tangential stress (Fig. 27). Distinct neutral point regions are delineated by small circular contours above and below the hole in the image. The minimum principal stress τ_3 is now tensional at the wellbore wall in all directions.

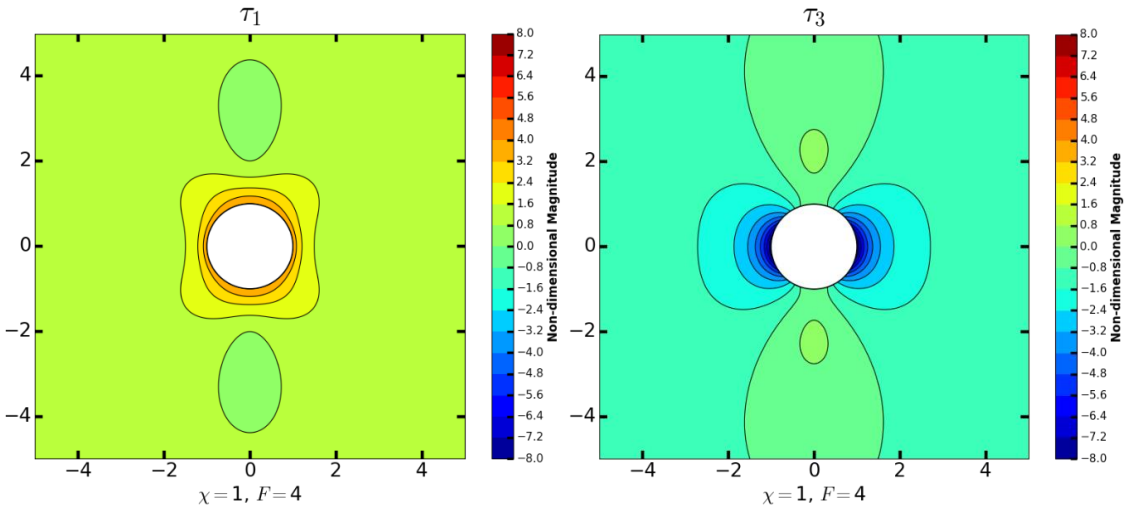

Figure 40: χ=1 (bi-axial far-field stress) and F=4 (borehole net pressure is overbalanced and four times as compressive in magnitude as far-field τ_1). The maximum principal stress τ_1 is similar to the radial stress and the minimum principal stress τ_3 relates to the tangential stress (Fig. 28). Distinct neutral point regions are seen as small circular contours above and below the hole in the image for the τ_3 contours, but are not so easily seen in the τ_1 contours.

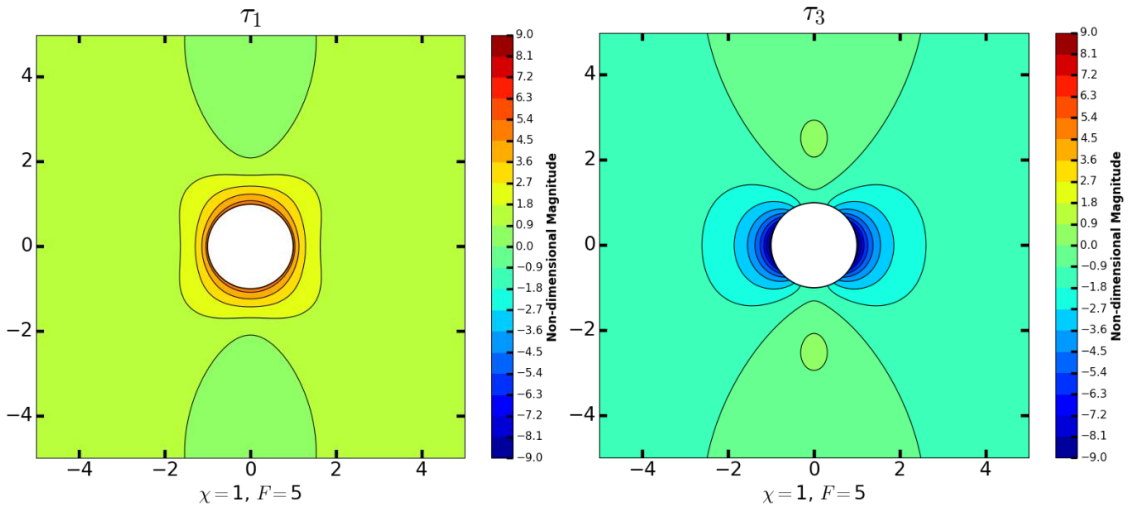

Figure 41: χ=1 (bi-axial far-field stress) and F=5 (borehole net pressure is overbalanced and five times as compressive in magnitude as far-field τ_1). The maximum principal stress τ_1 is similar to the radial stress and the minimum principal stress τ_3 relates to the tangential stress (Fig. 29). Distinct neutral point regions are seen as tiny circular contours above and below the hole in the image for the τ_1 contours, but are not so easily seen in the τ_3 contours.

5.3 Differential principal stresses

Additionally, the differential non-dimensional deviatoric principal stress magnitudes are mapped out in the subsequent figures. Beginning with the uniaxial far-field stress case, observe that for the initial borehole state (F=0), a compressive (positive) stress concentration exists in the direction of the least principal stress (θ=90º). As the net borehole pressure is increased positively to F=1, the differential stress contours form a perfect image of the F=0 case, rotated by 90º. An excess compressive stress concentration now exists in the direction of the maximum principal stress (θ=0º). Note that for F=0, instability is likely to be compressive failure due to the increased compressive tangential stress in the τ_3 direction (Figs. 30, 36), precisely where we see the concentration of compressive stress for the deviatoric stress differential. For F≥1, instability is likely to be

tensile failure in the τ_1 direction due to the tangential stress going negative and reaching tensile strength, corresponding to the buildup of compressive stress we see in the differential contour plots. This fundamental insight gives further credence and understating to the theory that instability will occur in planes where differential stress is greatest, and this direction from the borehole is always perpendicular to the neutral point locations.

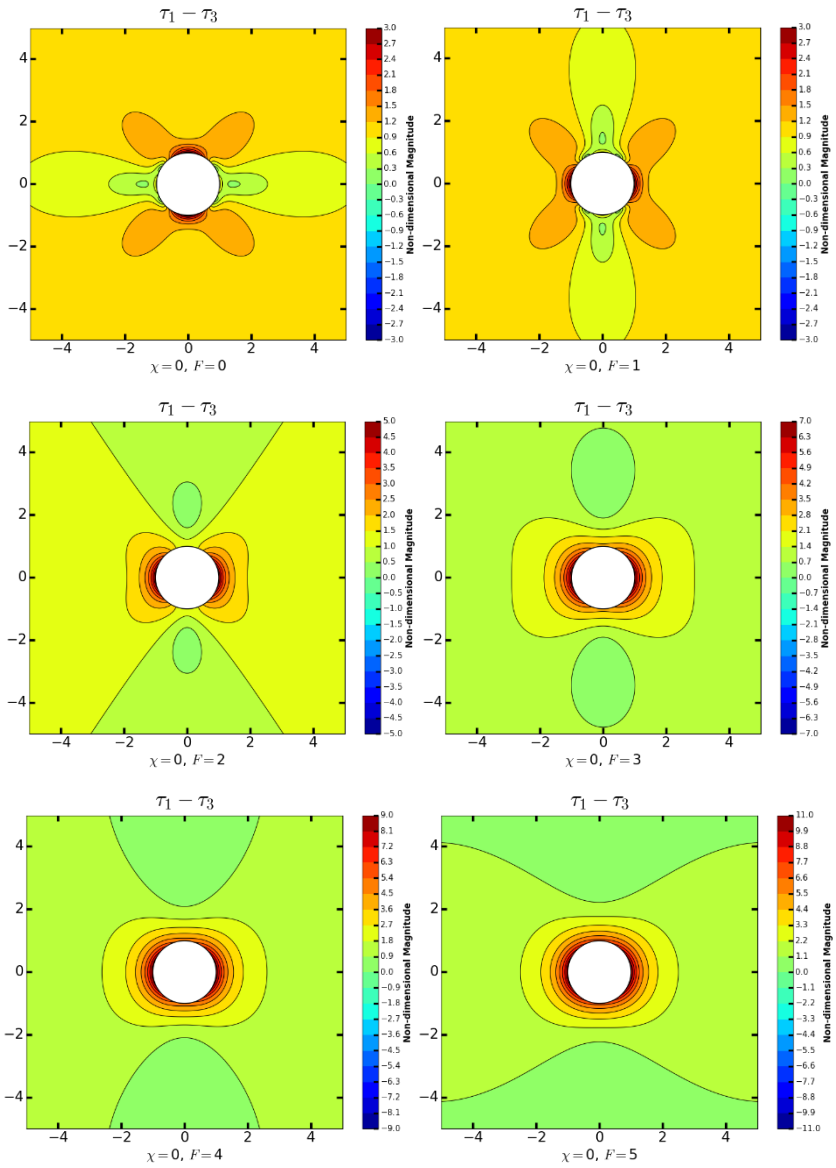

Figure 42: $\chi = 0$, $F \geq 0$. The deviatoric principal differential stresses ($\tau_1 - \tau_3$) are shown. For F=0, the highest stress concentration is in the τ_3 direction, and compressive failure is likely to occur in this direction. For F≥1, the maximum stress concentrations occur orthogonal to the direction seen for F=0 (i.e., in the direction of τ_1). Depending on rock properties, tensional failure will occur along this τ_1 axis for F≥1.

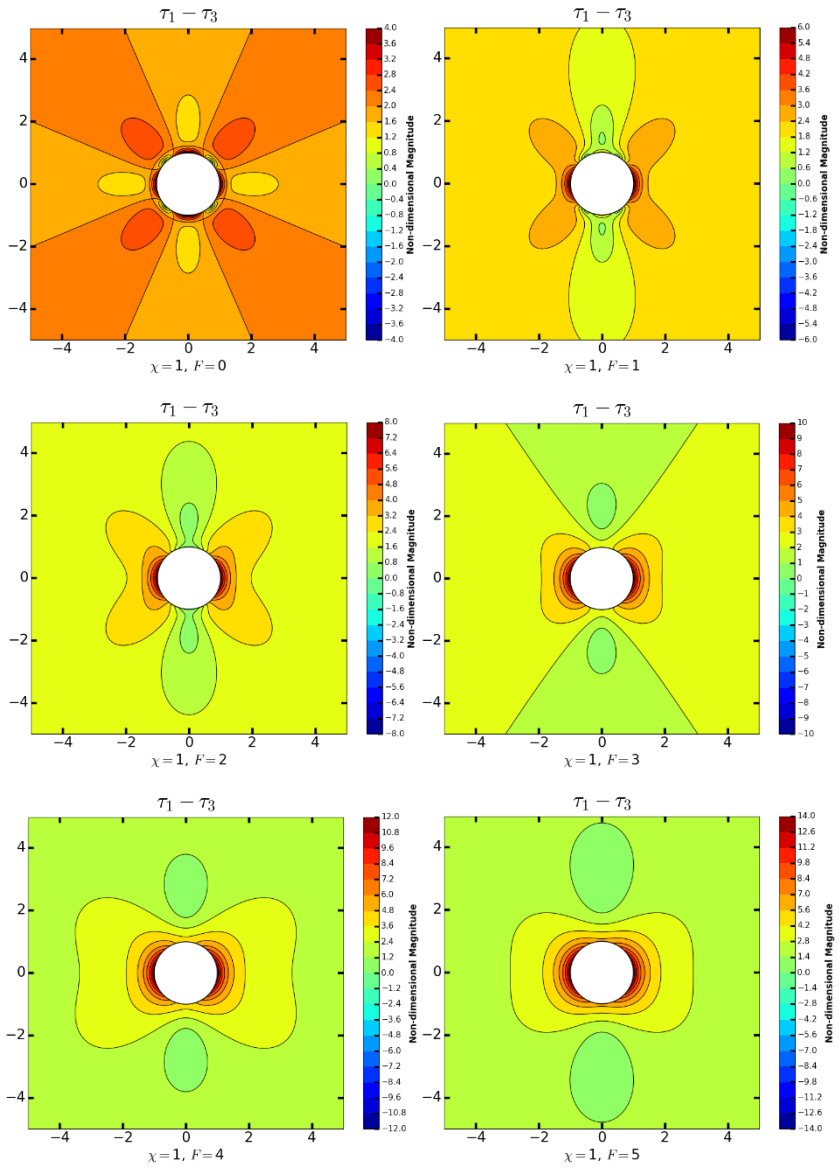

Figure 43: The deviatoric principal differential stresses ($\tau_1 - \tau_3$) are shown for χ=1 and 0≥F≥5. When F=0, the differential stresses form a flower pattern, with balanced stress concentrations on the four principal sides of the hole. For F≥1, maximum stress concentrations occur in the direction of τ_1. Depending on rock properties, tensional failure will occur along this τ_1 axis for F≥1 if the strength of the rock is less than the stress trying to push it open.

5.4 Principal stress trajectories

Neutral points are defined as locations where the magnitudes of the two deviatoric principal stresses in a plane of view are equal to each other. When F=0 (i.e., balanced borehole net fluid pressure), neutral points occur at four locations around the rim of the wellbore. For χ=0 (Fig. 44a), the neutral points are pulled in closer to the horizontal axis (direction of far-field τ_1), occurring around the borehole rim at θ = (30º, 150º, 210º, 330º). The compressive τ_1 trajectories (blue) located near the θ=0º line, curve around the borehole, unable to pass through the region where the two neutral points are so close together. When F=0 and χ=1 (Fig. 45a), τ_1 (blue) and τ_3 (green) trajectories are perfectly balanced, and as a result, the four neutral points are located at even distances between the two deviatoric principal stress – occurring along the wellbore wall at θ = (45º, 135º, 225º, 315º). As *F* increases positively, corresponding to an increase in P_{NET}, the neutral points move around the rim of the rock towards the τ_3-direction. At *F*=1, four neutral points still exist at the wellbore rim, but they have moved closer to the top and bottom of the borehole in the alignment of the image (i.e., closer to the direction of τ_3; see Figs. 44b and 45b).

As the Frac Number increases from 1 to 2, the four neutral points move away from the wellbore rim and in the direction of τ_3, until the four neutral points become only two neutral points appearing on opposite sides of the borehole in the direction of the least principal far-field stress. The two neutral points mark the boundary for the stress cage, within which all radial stress is compressional (See Figs. 44c and 45c). For these larger Frac Numbers, the most striking difference between the uniaxial case and the bi-axial plane case is that for the same F-value, the neutral points are much further away, and by

extension, the stress cage is much larger, for the uniaxial stress cases (χ=0). Therefore, the region wherein the principal stresses have reversed behaviors in relation to the tangential and radial stresses is larger for the uniaxial case. However, the levels of anisotropy (differences in stress concentrations between the maximum and minimum orientations) are far greater for the bi-axial plane stress condition.

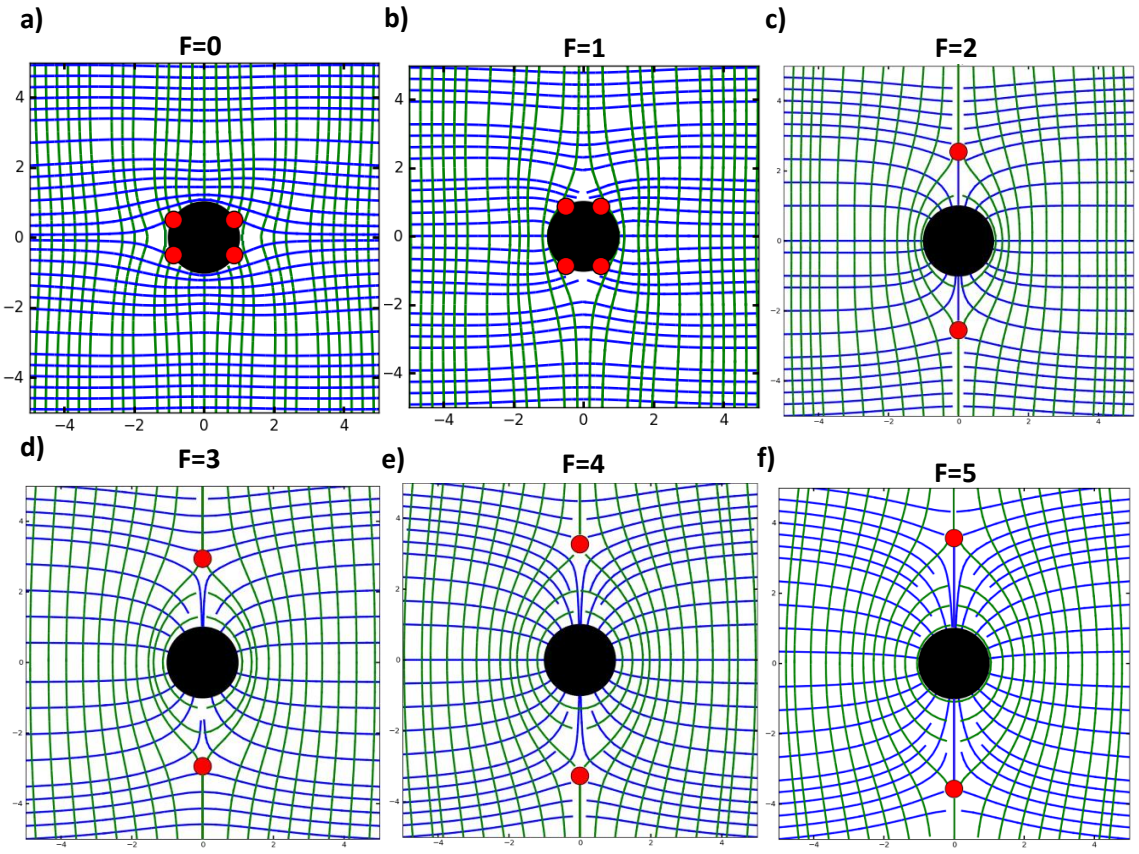

Figure 44: Principal stress trajectories are displayed for χ=0 and 0≥F≥5. The maximum principal stress τ_1 (blue trajectories) is oriented along the horizontal and the minimum principal stress τ_3 (green trajectories) is directed along the vertical. Neutral points are indicated by red dots. The borehole (black circle) is centered and given unit radius. Distances are non-dimensional, normalized by the borehole radius. For F≥2, the τ_3 (green) trajectories form closed elliptical rings around the borehole, bounded by the two neutral points. **a:** F=0. **b:** F=1. **c:** F=2. **d:** F=3. **e:** F=4. **f:** F=5.

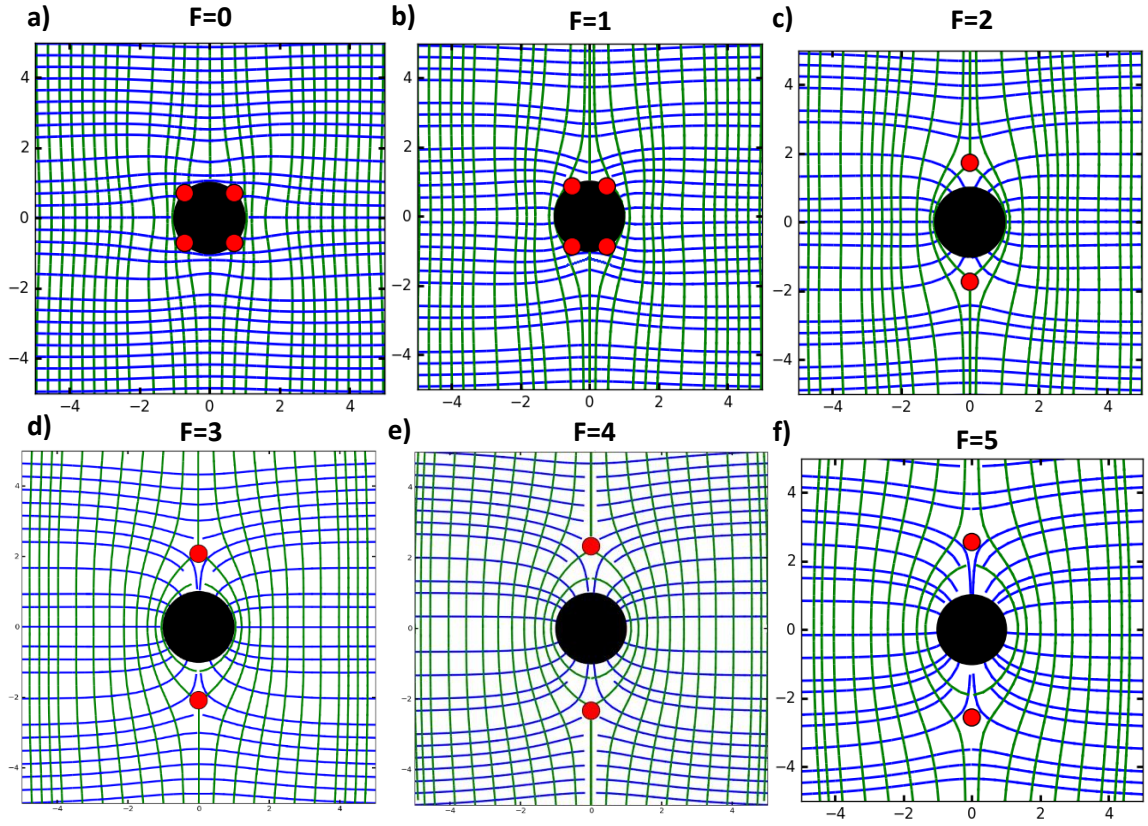

Figure 45: Principal stress trajectories are displayed for χ=1 and 0≥F≥5. The maximum principal stress τ_1 (blue trajectories) is oriented along the horizontal and the minimum principal stress τ_3 (green trajectories) is directed along the vertical. Neutral points are indicated by red dots. The borehole (black circle) is centered and given unit radius. Distances are non-dimensional, normalized by the borehole radius. For F≥2, the τ_3 (green) trajectories form closed elliptical rings around the borehole, bounded by the two neutral points. **a:** F=0. **b:** F=1. **c:** F=2. **d:** F=3. **e:** F=4. **f:** F=5.

6. FRACTURE CAGE

When a borehole is drilled into stressed rock, the host rock attempts to close the hole in the radial direction (reduce the hole's diameter by a few thousandths of an inch). The diameter of the hole decreases slightly, compressing the circumference tangentially (increase hoop stress). The hole diameter stops declining when the tangential stress (hoop stress) balances the radial stress. If the hoop stress exceeds the rock strength before the stresses come to equilibrium, the rock breaks and the hole enlarges.

Formation stress determines stability of the borehole. If the stress around the hole exceeds the strength of the rock, the rock fails and the hole enlarges. This type of instability, known as shear failure, occurs when a borehole is locally underbalanced (Frac Number is negative), which creates a fracture cage. Negative Frac Numbers may arise during underbalanced drilling, open-hole completions, or regular drilling operations when an unexpected high-pressure formation is penetrated. They can also occur during drilling when the pumps are turned off.

Fracture cage: Confined space around borehole where the principal deviatoric compressional stress follows concentric rings so that any radial fracture emanating from the wellbore into the fracture cage space will remain trapped inside and rotate into the direction of the concentric τ_1 trajectories (normal to the tension stress, which is radial inside the fracture cage).

Fracture caging: Formation of concentric tension fractures and shear joint breakouts inside a fracture cage space due to a wellbore going underbalanced as it unexpectedly penetrates an overpressured formation, which renders the Frac Number for that wellbore section negative.

Fracture caging runaway: Progressive elongation of borehole in the direction of least principal stress due to sustained fracture caging as circumferential tension fractures continue to form new and wider fracture cages that collapse inwards while the removal of rock debris by upward flow through the production annulus creates room for further fracture caging. This process continues as long as the Frac Number remains negative and the net pressure large enough to continue collapse of the wellbore section by tensional failure and shear joint breakout.

Figure 46: Definition of 'fracture cage' and related terms. Adapted from Weijermars et al. (2013).

Fracture cages, which occur in underbalanced wellbores, preclude any tension fracture initiated at the wellbore to escape outward from the elliptical area. The fracture cage is outlined by a τ_1 trajectory that forms a closed elliptical ring around the borehole, bounded by the two neutral points (Fig. 47a). Weijermars et al. (2013a) derived an equation for determining the fracture cage ellipse dimensions. The horizontal line through the two neutral points connects zones of principal stress reversal, with a change in the

deviatoric stress sign (see Figs. 12-16). The compressional stress (τ_1) due to the far-field stress will be deflected inside the fracture cage zone. A tensional stress (τ_3) on the horizontal line inside the fracture cage is aligned with a compressional stress (τ_1) outside the fracture cage zone. These two principal deviatoric stresses are separated by the neutral points, where their respective magnitudes are equal. This insight differs slightly from Weijermars (2016), which stated that at the neutral point locations, the two deviatoric stresses are both zero. For lower F-values, this is definitely not the case (see Fig. 12-16).

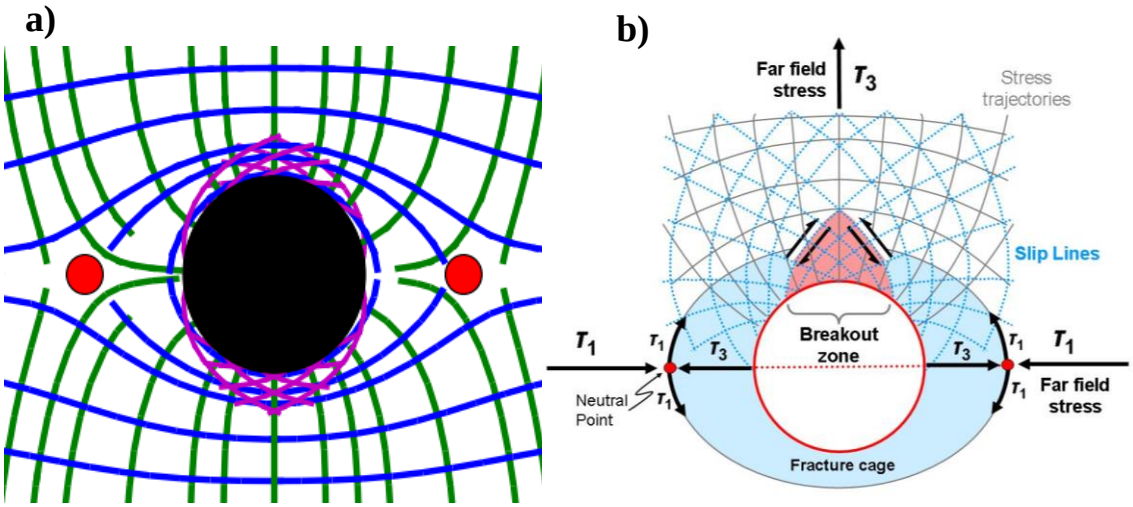

Figure 47 a: Principal stress trajectories for an underbalanced borehole are shown. The slip lines (magenta), resolved by rotating the principal stress direction by an angle θ_b (Eq. 16), show the preferential slope of shear failure. Reprinted from Weijermars and Schultz-Ela (2015). **b:** A more detailed rendition of the relationship between slip lines and shear failure. The breakout zone can be rendered by incorporating both slip line solutions and a failure criterion that predicts the width and depth of breakout.

In locally underbalanced settings, radial tension fractures cannot initiate at the wellbore because tension fractures may only propagate along the τ_1-trajectories, and the stress reversal inside the fracture cage imposes concentric τ_1-trajectories. Such tensile

fractures always form perpendicular to the tensile stress (τ_3) and dilate in the direction of τ_3. Underbalanced wellbores (F<0) have principal stresses, τ_1 and τ_3, in the fracture cage (Fig. 47a) rotated 90˚ compared to those in the stress cage of overbalanced wells (F>0; Fig. 10b). Fracture caging is a recently recognized drilling hazard that directs induced fractures around the wellbore (Fig. 11). Fracture caging (Fig. 46) associated with underbalanced borehole conditions leads to cavitations, slabbing, and spalling under specific physical conditions. Tension fractures may grow after hydraulic pressure is applied only when an initial crack is already present normal to the wellbore. However, such fractures will not grow radially outward. Instead, such fractures will deflect into the direction of τ_1 trajectories, which form closed ellipses inside the fracture cage. This phenomenon has been described analytically (Weijermars, 2011) and examples appeared in numerical, fully-coupled fluid flow simulations (Zhang et al., 2011a,b).

When the pressure within the drilled rock is higher than the mud hydrostatic pressure acting on the borehole or rock face (i.e., F<0), the greater formation pressure forces formation fluids into the wellbore. This forced fluid flow is called a “kick”. If the flow is successfully controlled, the kick is considered to have been killed. An uncontrolled kick that increases in severity may result in what is known as a “blowout.” Kicks occur as a result of formation pressure being greater than mud hydrostatic pressure, which causes fluids to flow from the formation into the wellbore. In almost all drilling operations, the operator attempts to maintain a hydrostatic pressure greater than formation pressure and, thus, prevent kicks. When the formation occasionally exceeds the mud pressure, a kick occurs. The imbalance between mud and formation fluid pressures that leads to kicks are

most often attributed to inadequate mud weight, improper hole fill-up during trips, swabbing, cut mud, and lost circulation (Hornung, 1990).

The slip line solutions (Section 8) related to the principal stresses in the fracture cage (Fig. 47a) are compatible with common breakout observations (Zoback et al., 1985). The occurrence of circular tension failure around underbalanced holes has been observed in laboratory experiments (Roest et al., 1989; Vardoukalis et al., 1988) and is known from implosions around cavities in nuclear tests (Fig. 48a). These examples are for confining pressure and do not involve any deviatoric background stress, which therefore corresponds to boreholes with a negative net pressure ($F \rightarrow -\infty$).

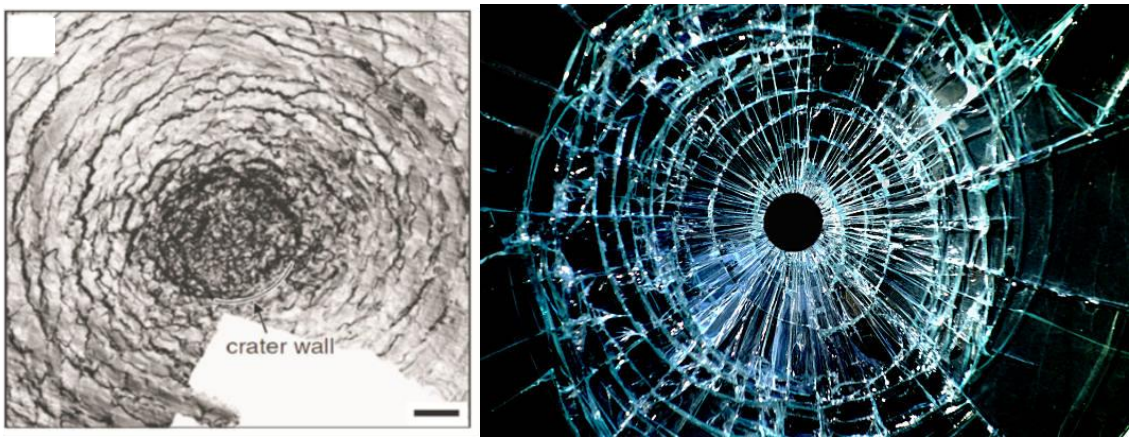

Figure 48 a: Impact crater used analogously to a collapsing salt diapir. Reprinted from Stewart (2006). **b:** When a bullet makes vacuum as it penetrates through a plane of glass, the preferred fracture orientation is redirected and circumferential fractures occur around the exit-hole. Because radial and circumferential fractures occur for this case where underbalanced conditions approach $F \rightarrow -\infty$, it is reasonable to assume that during instability common with underbalanced wellbores, shear/compressive failure, tensile fractures also occur as the rock breaks.

6.1 Tangential and radial stresses

The following sets of figures depict the non-dimensional tangential and radial stress concentrations (normalized by far-field τ_1) around a borehole that has been drilled into rock subjected to a uniaxial far-field boundary stress. We will assume that initially, the borehole net pressure is balanced (F=0). The F-value may even be negative, initially, when the hole is cut into the rock. The tangential stress is increased compressively as the host rock attempts to close the hole, decreasing the radius slightly. This resultant compressive tangential stress precludes shear failure, including breakout. To prevent such instabilities, a driller increases the mud weight (increases the F-value), which expands the borehole, lowering the tangential stress. If, while drilling, an unexpected high-pressure formation is penetrated, the F-value could suddenly decrease considerably, reaching negative values that could cause fracture caging or even fracture caging runaway.

As a wellbore becomes more underbalanced, higher concentrations of compressive tangential stress accumulate along the wellbore rim in the direction of τ_3. Beginning with the uniaxial boundary stress condition (χ=0), when F=-1, the tangential stress is already positive (compression) in every orientation from the borehole. As F become progressively more negative (borehole becomes increasingly more underbalanced), the tangential stress increases compressively around the borehole, and the regions where tangential stress exceeds rock strength (necessary for borehole failure) widen. For negative Frac Numbers ($F \geq 5$), shear failure can encompass the entire borehole, with breakout sections reaching 360º. Also, the radial stress become more negative as the borehole becomes more underbalanced, and the difference between the maximum and minimum radial stress

magnitudes exhibited at the borehole wall becomes smaller, corresponding to the neutral points (in the direction of far-field τ_1) moving further away from the borehole.

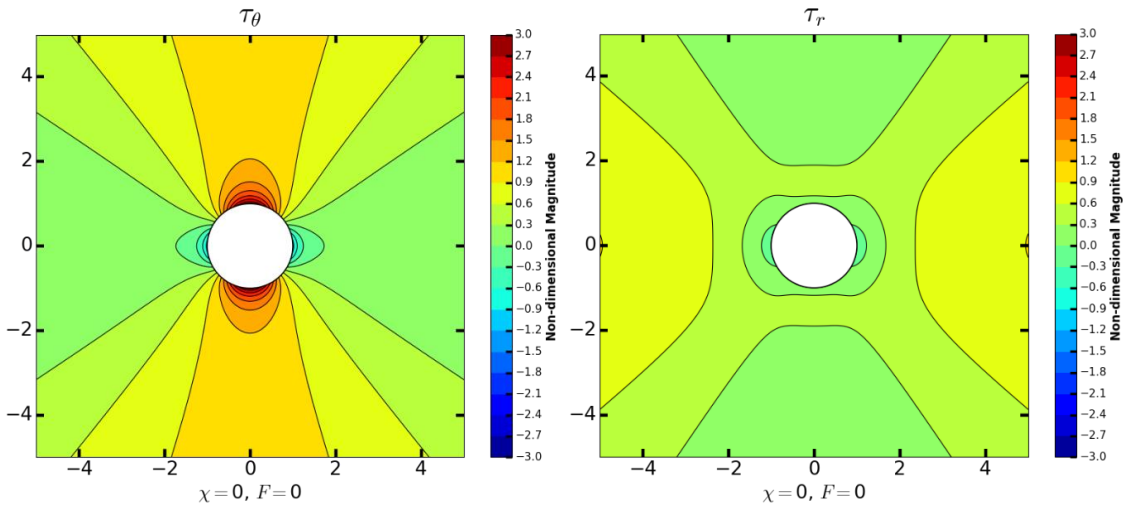

Figure 49: χ=0 (uniaxial far-field stress) and F=0 (balanced borehole net pressure). A highly compressive tangential stress concentration exists in the τ_3 direction (three times as compressive as far-field τ_1). The radial stress is reduced near the borehole. Compressive failure is likely to occur, depending on the strength of the rock. Increase mud weight (increase F) to avoid break out.

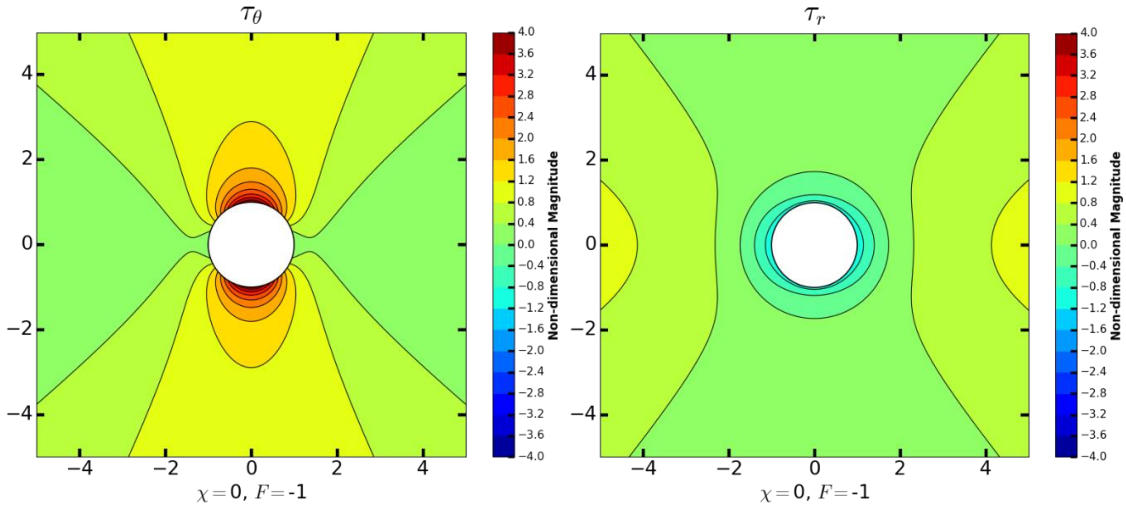

Figure 50: χ=0 (uniaxial far-field stress) and F=-1 (underbalanced borehole net pressure where $P_{NET} = -1*\tau_1$). The region where the tangential stress was tensile for F=0 has vanished, and the tangential stress is compressive around the entire borehole rim, with large stress concentrations in the direction of the least principal stress. The radial stress is tensional around the entire borehole, with peak negative stress concentrations in the τ_1 direction.

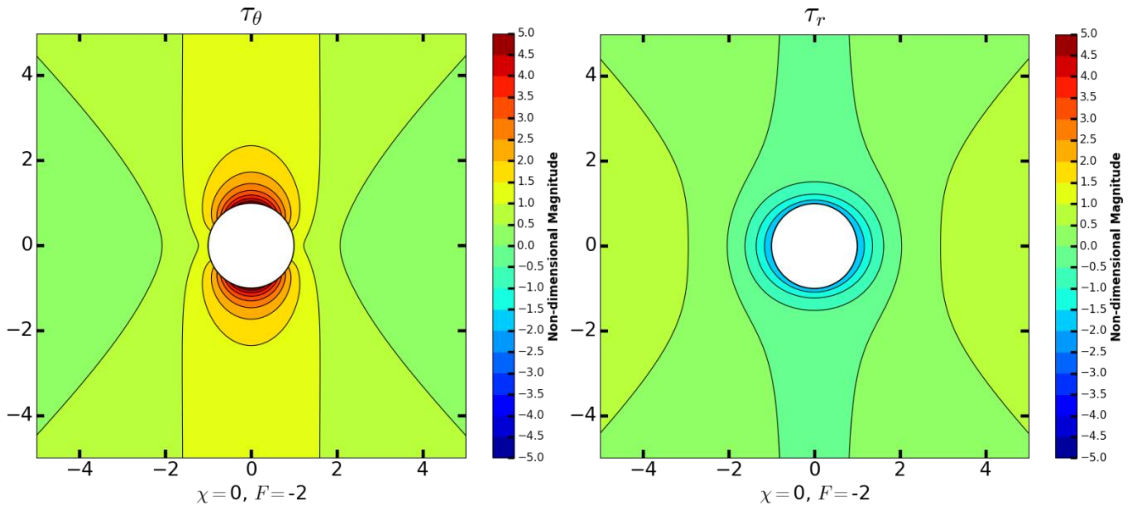

Figure 51: χ=0 (uniaxial far-field stress) and F=-2 (underbalanced borehole net pressure where $P_{NET} = -2*\tau_1$). The tangential stress is compressive around the entire borehole rim, with large stress concentrations in the direction of the least principal stress (5 times the magnitude of far-field τ_1). The radial stress is tensional around the entire borehole, with peak negative stress concentrations in the τ_1 direction. The radial stress is much more evenly distributed around the hole than the tangential stress which exhibits large stress anisotropies between the two far-field directions.

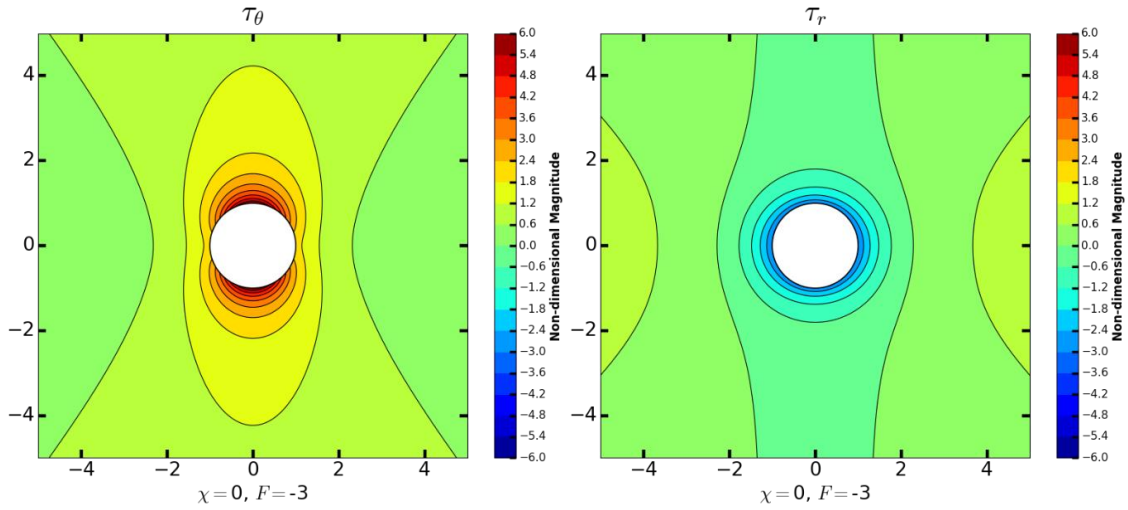

Figure 52: χ=0 (uniaxial far-field stress). As F become progressively more negative (borehole becomes increasingly underbalanced), the tangential stress increases compressively around the borehole, and the regions where tangential strength exceeds rock strength, necessary for borehole failure, widens. The radial stress become more negative, and the difference between the maximum and minimum magnitudes exhibited at the borehole wall becomes smaller as the neutral points move further away from the borehole in the direction of far-field τ_1.

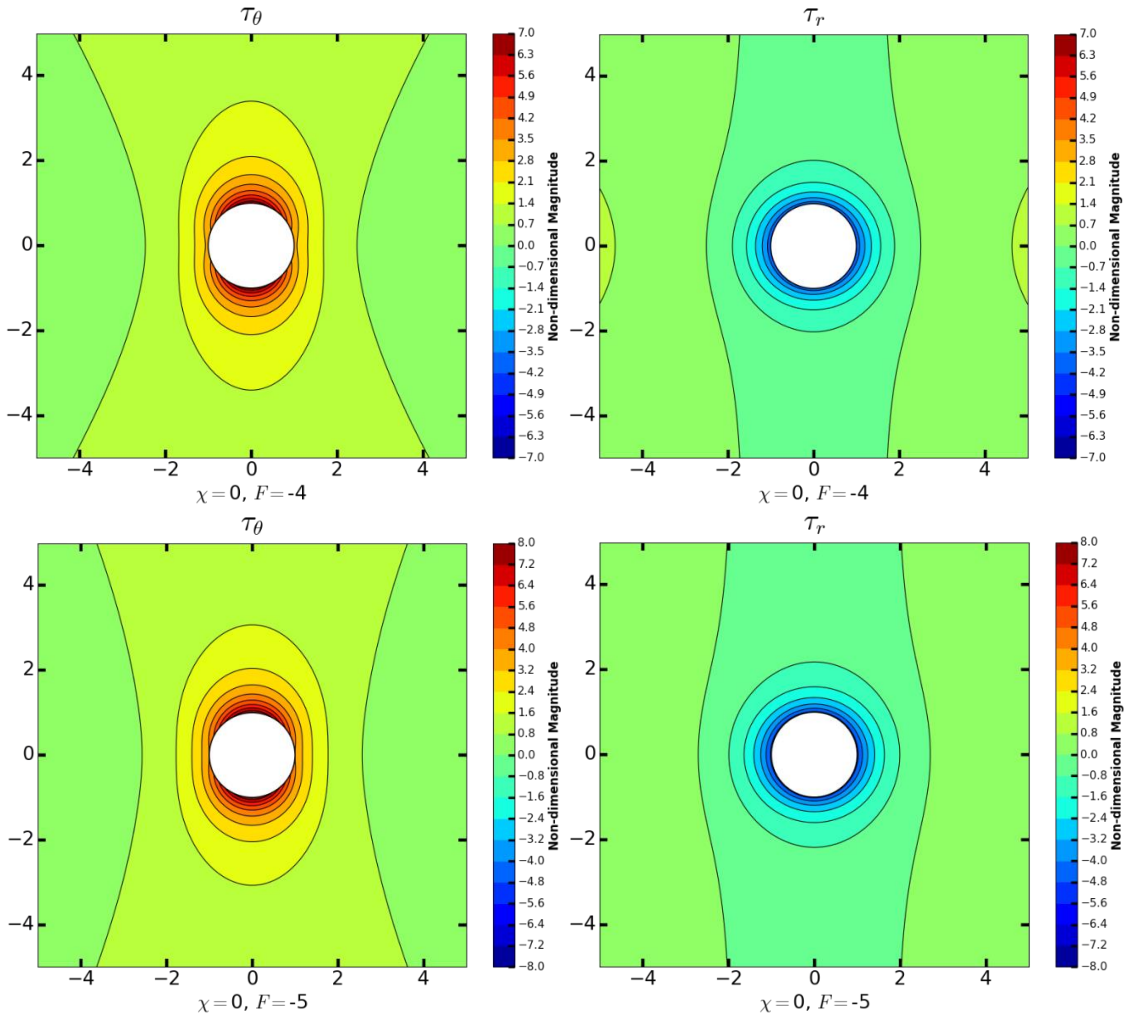

Figure 52: Continued

When bi-axial plane stress conditions occur (χ=1), we again observe that for F=0, perfect symmetry occurs between the section -45º≤θ≤45º and 45º≤θ≤135º, with magnitudes of the two sections being equal in absolute magnitude but opposite in sign (positive is compression and negative is tension). When the Frac Number is decreased (more negative), the tangential stress continues to increase positively in all directions and the radial stresses becomes more tensional (negative) in all directions. The region where

the tangential stress is still tensional at the borehole rim is very small for F=-3, and has vanished by F=-4.

Breakout occurs when the tangential stress exceeds rock strength and breaks the rock. By comparing the tangential stress magnitude contours for the uniaxial (χ=0) and bi-axial plane (χ=1) cases, the region where compressive tangential stress would exceed rock strength is much wider (i.e., breakout angle is much larger) for χ=0; however, for χ=1, although the breakout region would be narrower, the extent of the breakout into the rock formation is deeper, having the characteristic "pointed dog ears" shape speculated by Gough and Bell (1982).

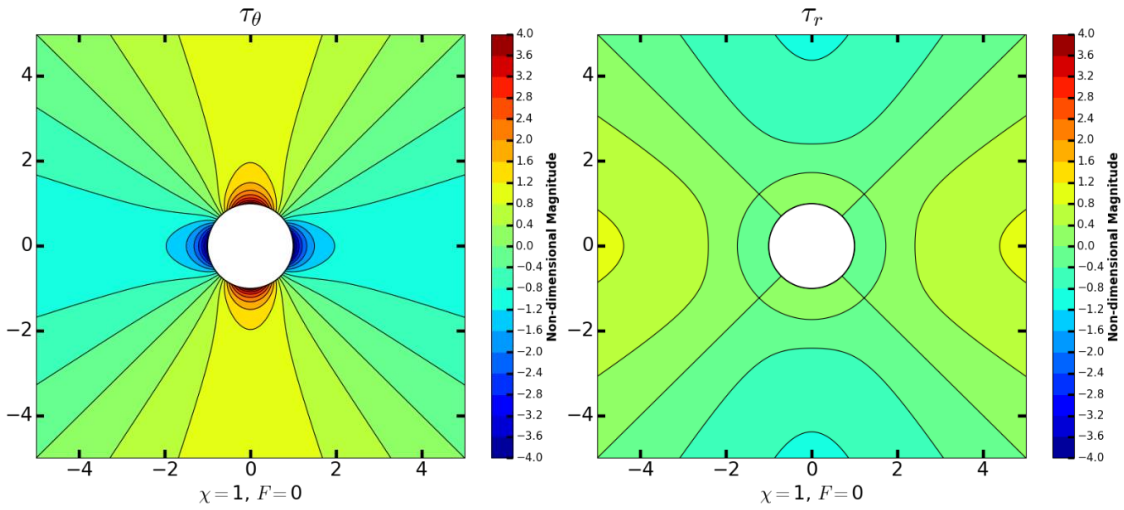

Figure 53: Bi-axial plane stress boundary conditions (χ=1) with underbalanced borehole net pressures -5≤F≤0. The distances are non-dimensional, normalized by the radius of the borehole. The contours represent non-dimensional deviatoric tangential (left-hand plots) and radial (right-hand plots) stress magnitudes, which have been derived using the Kirsch equations normalized by far-field τ_1 stress. In each row, a different Frac Number is used for the set of figures, with F=0 in the top row and F=-5 in the bottom row.

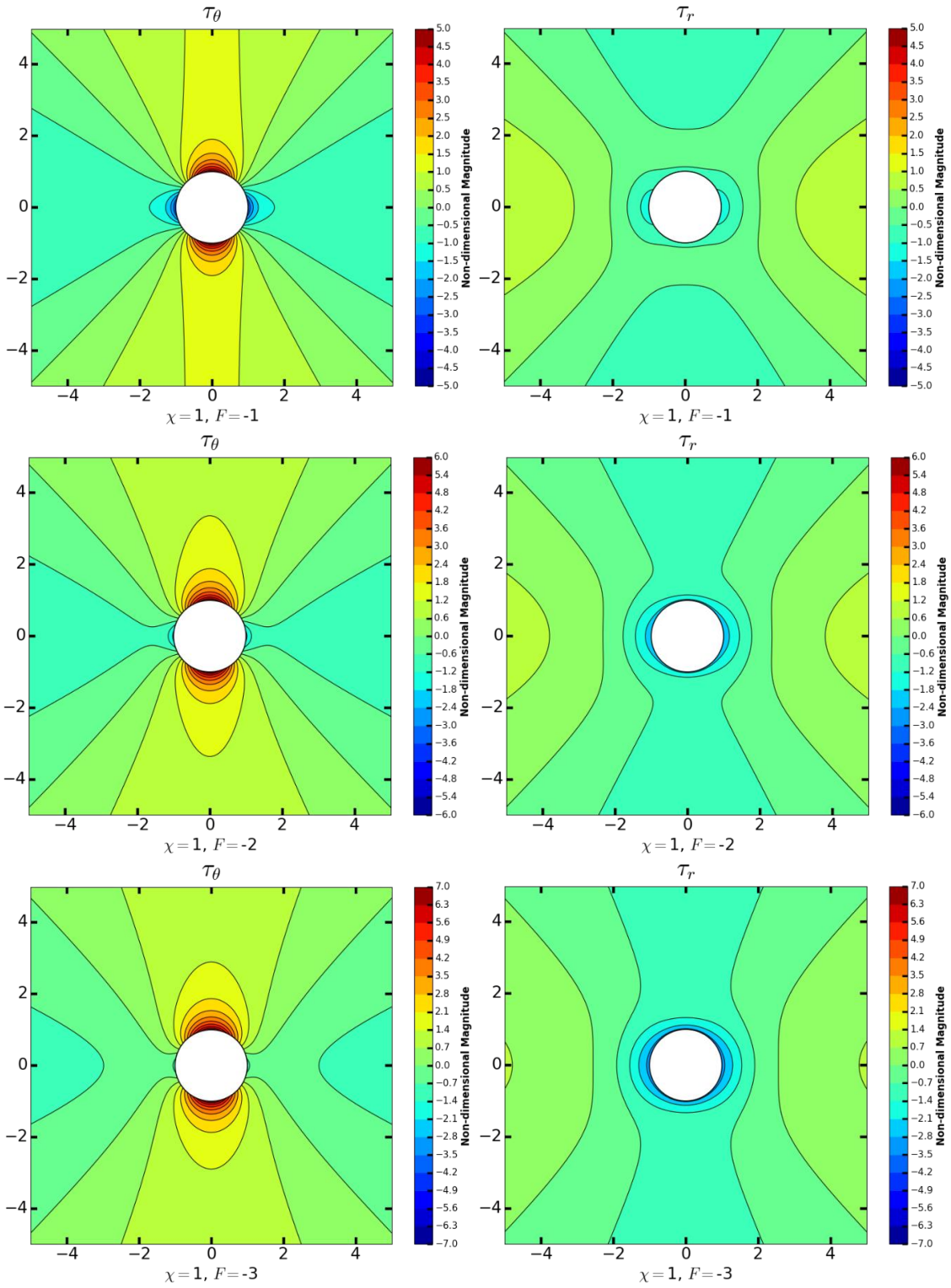

Figure 53: Continued

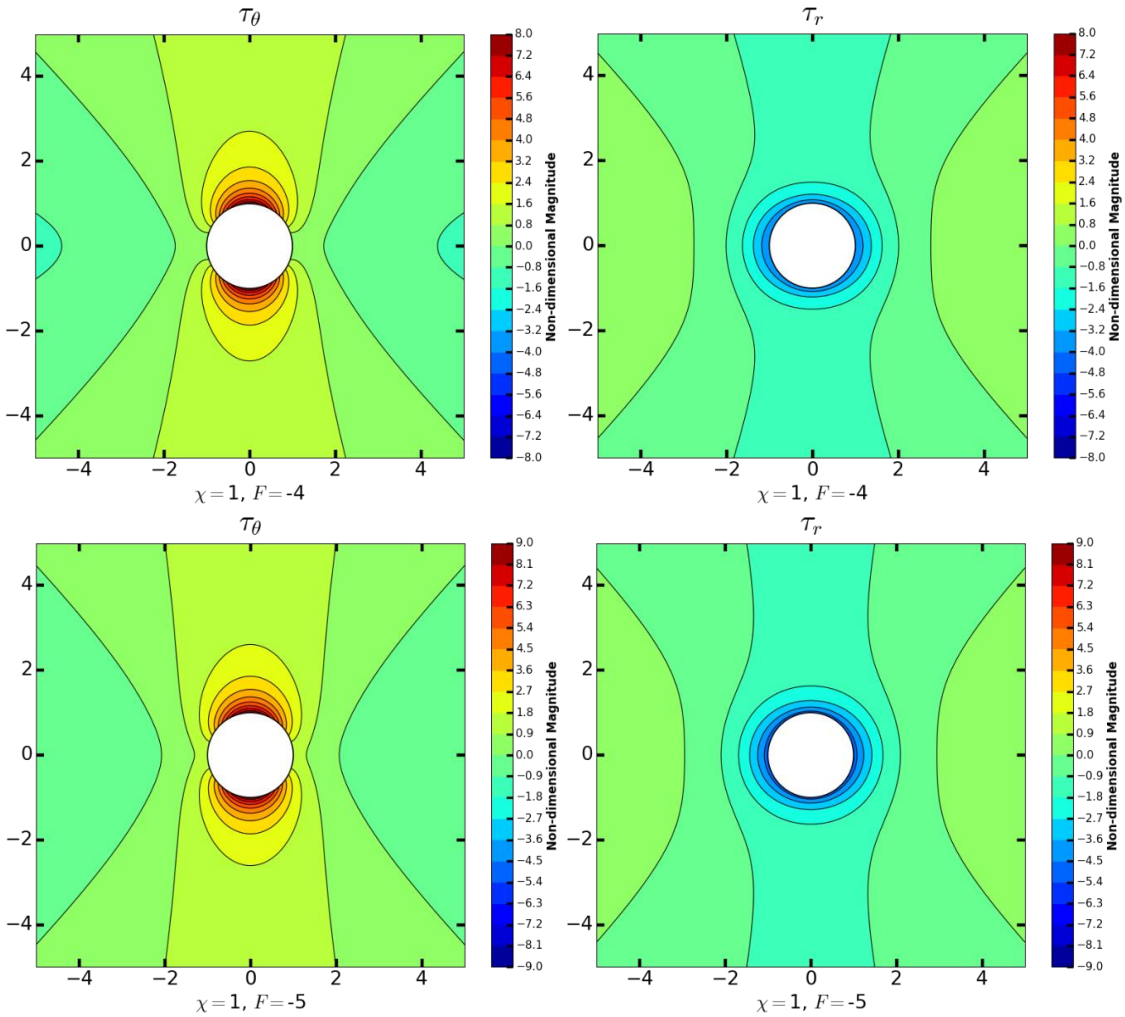

Figure 53: Continued

6.2 Principal deviatoric stresses

Just as we saw in Section 5.2, the principal deviatoric stress non-dimensional magnitudes are plotted as contours in the subsequent set of figures to show their relationship to the tangential and radial stresses. For F≥2, the neutral points can be discerned by comparing the τ_1 contours with the τ_3 contours, looking for regions on the left and right sides of the hole (direction of τ_1) where the magnitudes are equal. Typically, in one or both contour plots, there exists a small circular contour close to the region where

the neutral point occurs. For F≤-1, two neutral points occur along the τ_1 axis, at equal distances on opposite sides of the borehole. Looking at the τ_1 non-dimensional magnitude contours, for larger negative F-values, the neutral points occur further away from the borehole.

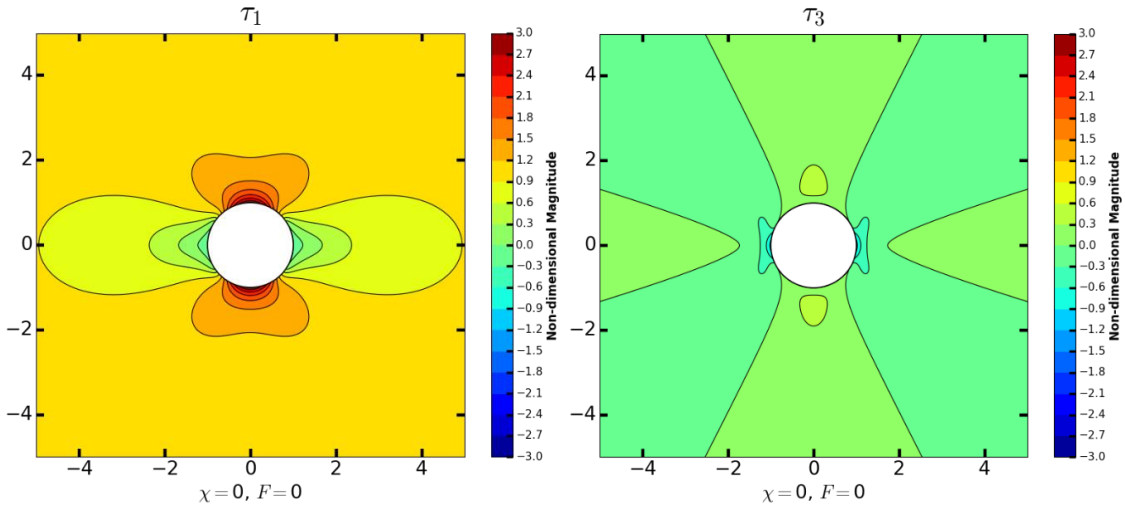

Figure 54: Uniaxial boundary stress conditions (χ=0) with underbalanced borehole net pressures -5≤F≤0. The distances are non-dimensional, normalized by the radius of the borehole. The contours represent non-dimensional principal deviatoric stress magnitudes, normalized by the far-field τ_1 stress. τ_1 stress magnitudes are shown in the left-hand images and τ_3 stresses in the right-hand. In each row, a different Frac Number is used for the set of figures, with F=0 in the top row and F=-5 in the bottom row.

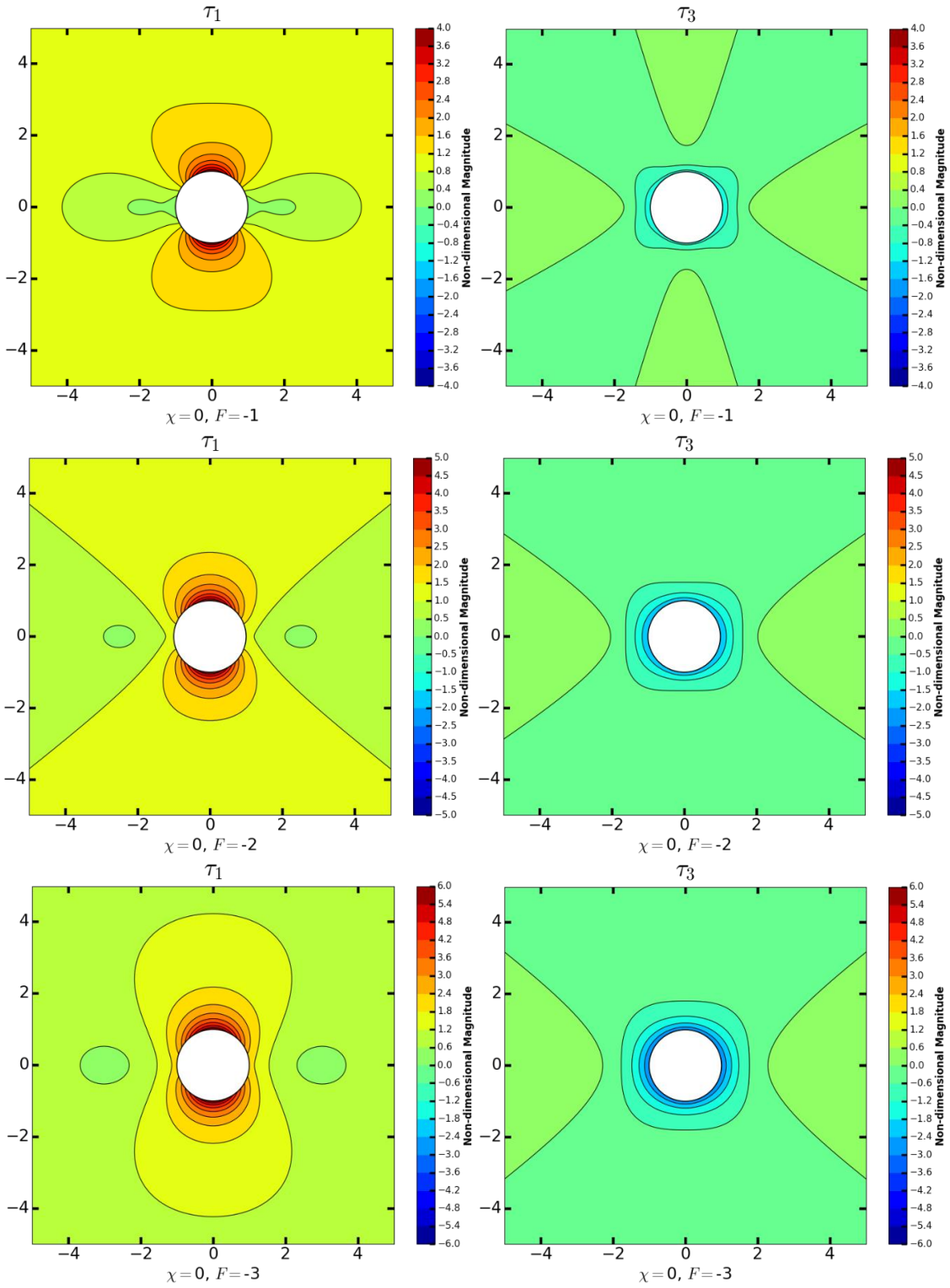

Figure 54: Continued

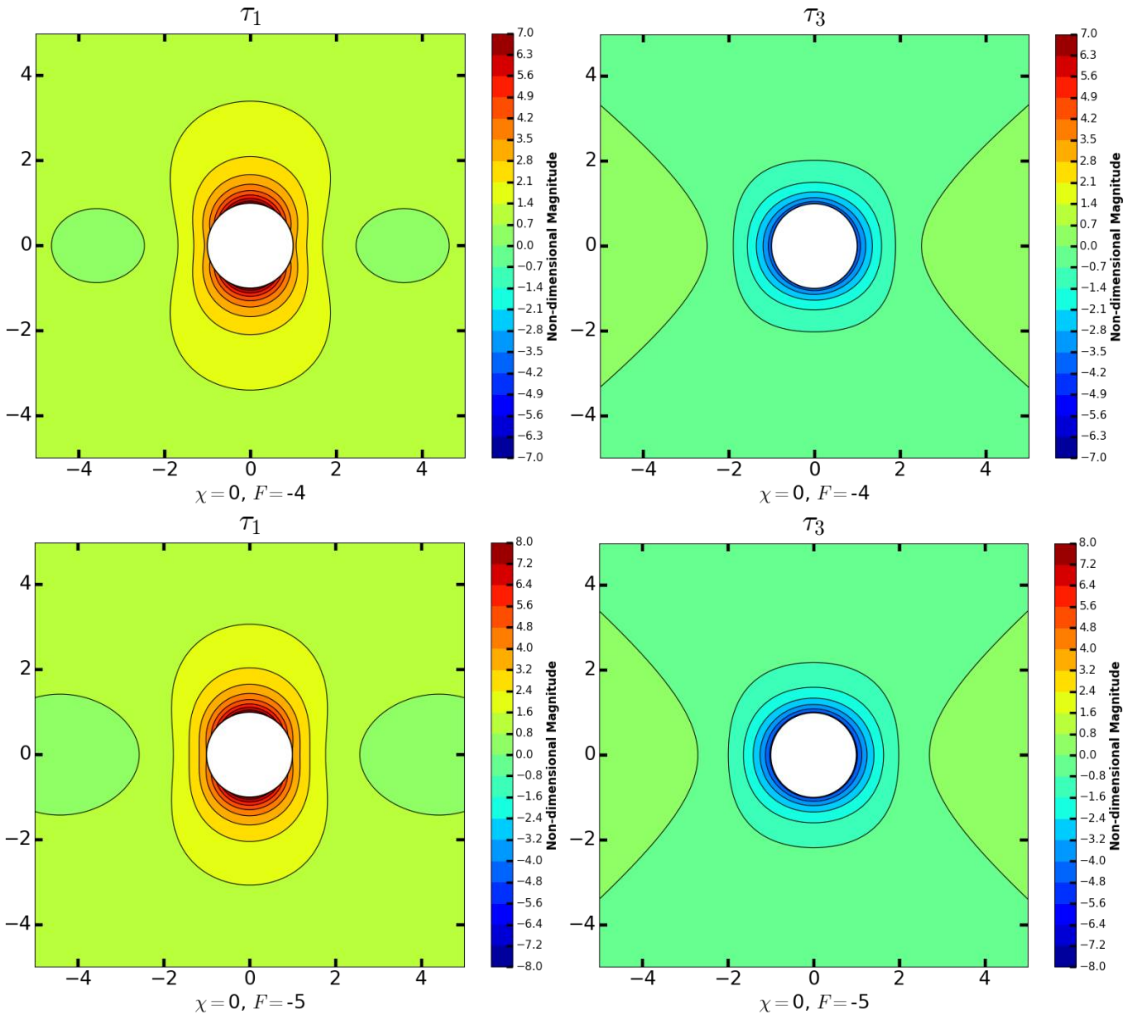

Figure 54: Continued

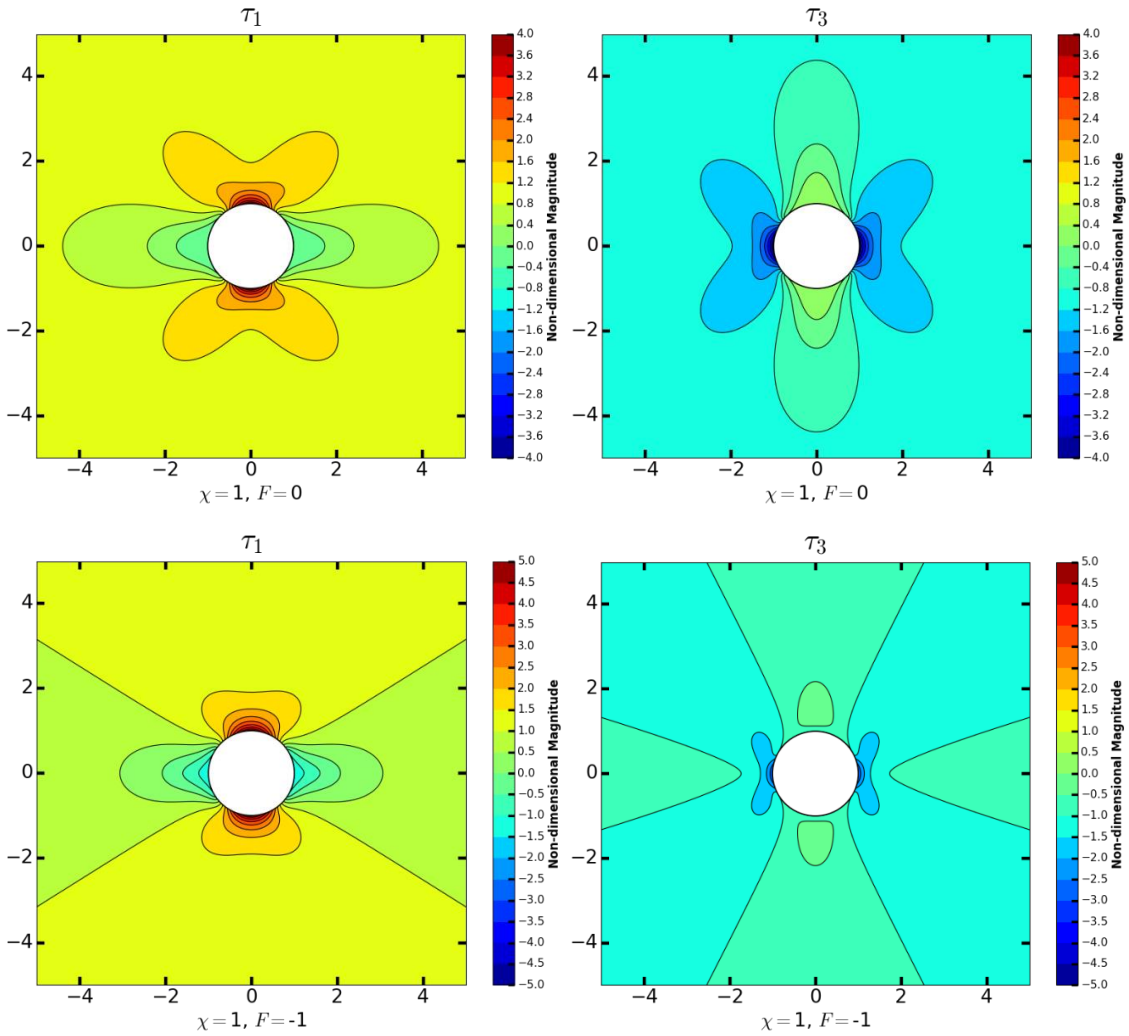

Figure 55: Non-dimensional stress magnitude contours are shown for principal deviatoric stresses τ_1 (Left) and τ_3 (Right). The magnitudes can be understood as multiples of the far-field τ_1 stress, as our solutions were normalized by the far-field τ_1 stress. Bi-axial plane stress boundary conditions (χ=1) are assumed for these sets of plots with underbalanced borehole net pressures $-5 \leq F \leq 0$. In each row, a different Frac Number is used for the set of figures, with F=0 in the top row and F=-5 in the bottom row. The distances are non-dimensional, normalized by the radius of the borehole.

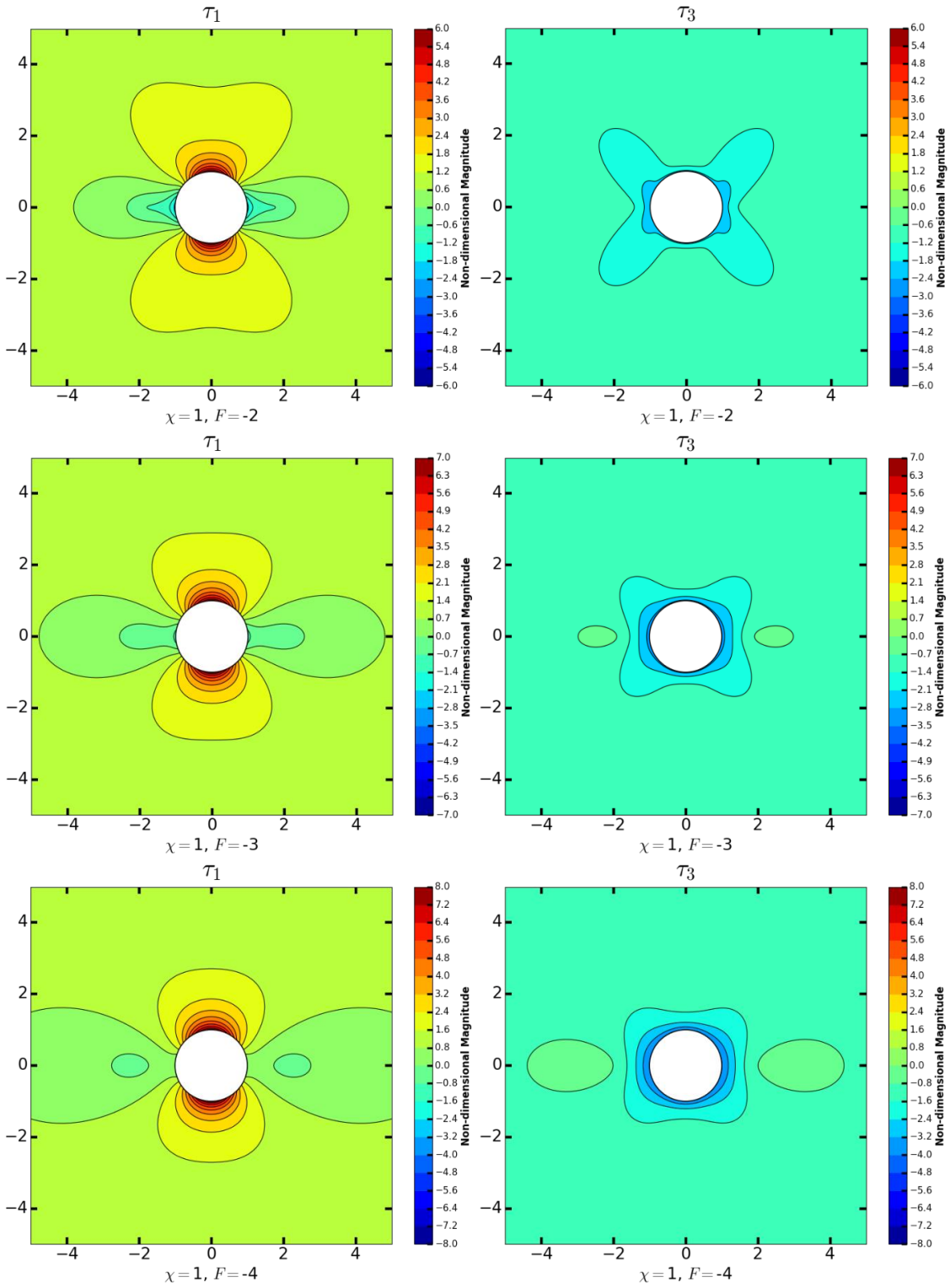

Figure 55: Continued

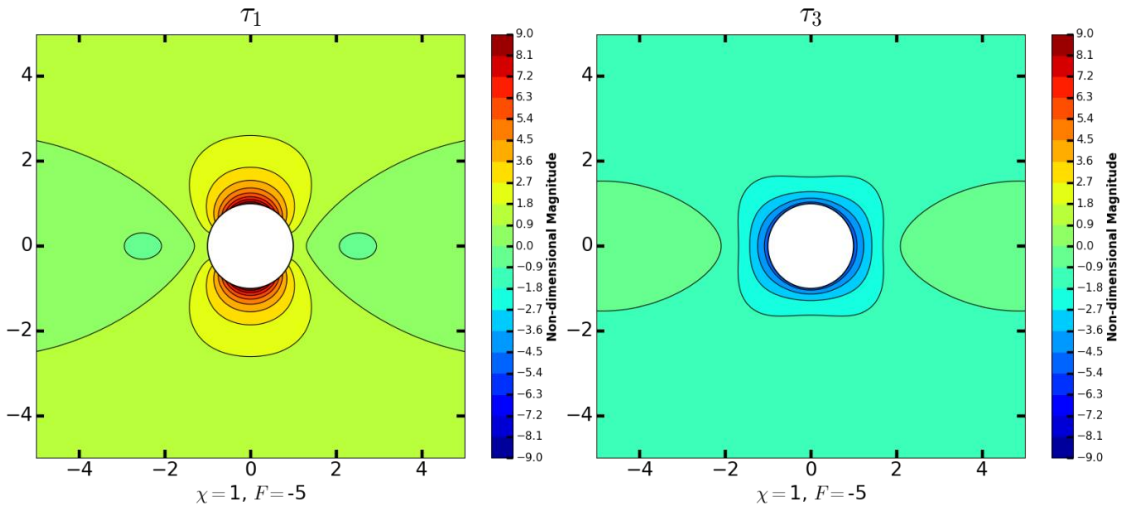

Figure 55: Continued

6.3 Principal differential stress

Neutral points are defined as points in space where the two deviatoric principal stresses are equal in magnitude. Thus, if we plot the difference of these two stresses $(\tau_1 - \tau_3)$, we can see visualize the neutral point locations by observing the regions where the contoured magnitudes are equal to zero. Because the contours are shown as intervals, the exact zero locations are not explicit in these figures, but they do provide a good enough approximation as to where the neutral points occur. The differential stress plots also serve to further our understanding of failure. For underbalanced boreholes (F<0), shear failure and breakout are the typical modes of failure, occurring parallel to the least principal stress. Failure, whether it be tensile or shear, appears to occur in the direction with the highest concentration of differential deviatoric stress, which would then of course be in the opposite direction to which the neutral points occur, since differential deviatoric stress is zero near them.

Uniaxial (χ=0) far-field stress conditions are considered in Figure 56 and bi-axial plane (χ=1) stress conditions are then observed in Figure 57. For the uniaxial case, a maximum stress difference occurs in the direction of the least principal stress for each figure. Beginning with F=0, four neutral points can be made out along the borehole rim, occurring at θ=(30º, 150º, 210º, 330º). Observe also that in the τ_1 direction, the regions between the two neutral points occurring on each side of the borehole are close to zero, with a point at about 0.7 radii from the borehole where the differential stress is practically zero. As F decreases, the neutral points move away from the borehole, and the differential stress increases near the borehole in all orientations, indicating that for larger negative Frac Numbers, shear failure could affect a wider region around the borehole.

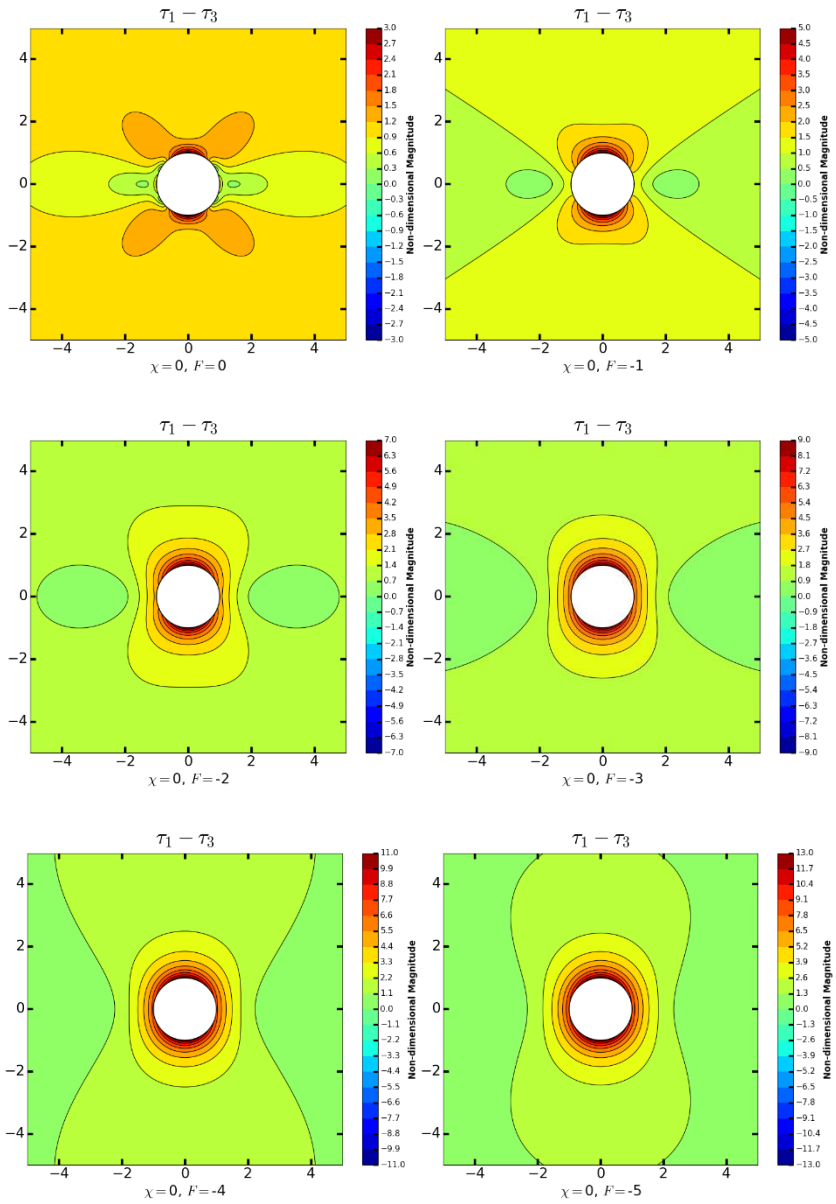

Figure 56: The principal deviatoric stress differentials are shown for uniaxial far-field stress (χ=0) and underbalanced borehole net fluid pressures -5≤F≤0. The contours represent the difference between the non-dimensional deviatoric principal stresses $(\tau_1 - \tau_3)$, where the solutions are normalized by far-field τ_1. Distances are non-dimensional, normalized by the radius of unit length. Regions where differential stress is greatest are most likely to experience failure, and given that the borehole is underbalanced in each figure, compressive/shear failure is most likely. Shear failure occurs in the direction of the least principal stress, which coordinates with the results shown here.

A few significant differences exist for the bi-axial plane stress (χ=1) compared to the uniaxial stress (χ=0) case. First of which is the unique flower shape the magnitude contours make when F=0. Recall that for χ=1 and F=0, the τ_3 contours are a perfect replica of the τ_1 contours rotated by 90º and multiplied by a negative 1 (Fig. 55). Because of this balance and the neutrality between the τ_1 and τ_3 trajectories (Fig. 58a) where neutral points occur at equal distances between the τ_1 and τ_3 directions (i.e., at θ=45º), the differential stresses have equal peaks in both principal stress directions. Thus, the most balanced condition is bi-axial plane stress (χ=1) with balanced borehole net pressure (F=0). Also observe that the differential stress contours of χ=1, F=-1 are identical to the case when χ=0, F=0, except the χ=1, F=-1 contours are 3 units of magnitude (normalized by far-field τ_1) higher everywhere around the borehole. Thus, although the two cases exhibit like contours, the χ=1, F=-1 case has much higher anisotropic stress concentrations that would much more readily inhibit borehole failure.

When F=-2, a unique neutral point profile occurs, in that, along the τ_1 axis, the two principal deviatoric stresses are equal at the borehole rim, and again a short distance away from the hole (Fig. 55). It is unclear what effect this would have on borehole stability or fracture propagation. Finally, the peak concentrations of differential stress are much more pronounced in the χ=1 plots than in the χ=0 plots. The χ=1 plots show higher differential stress concentrations in the peak orientations (parallel to τ_3) and also lower differential stress concentrations in the perpendicular directions (parallel to τ_1). This characterization is in part due to the neutral points being closer to the borehole for the χ=1 case than for χ=0 when using the same F-values.

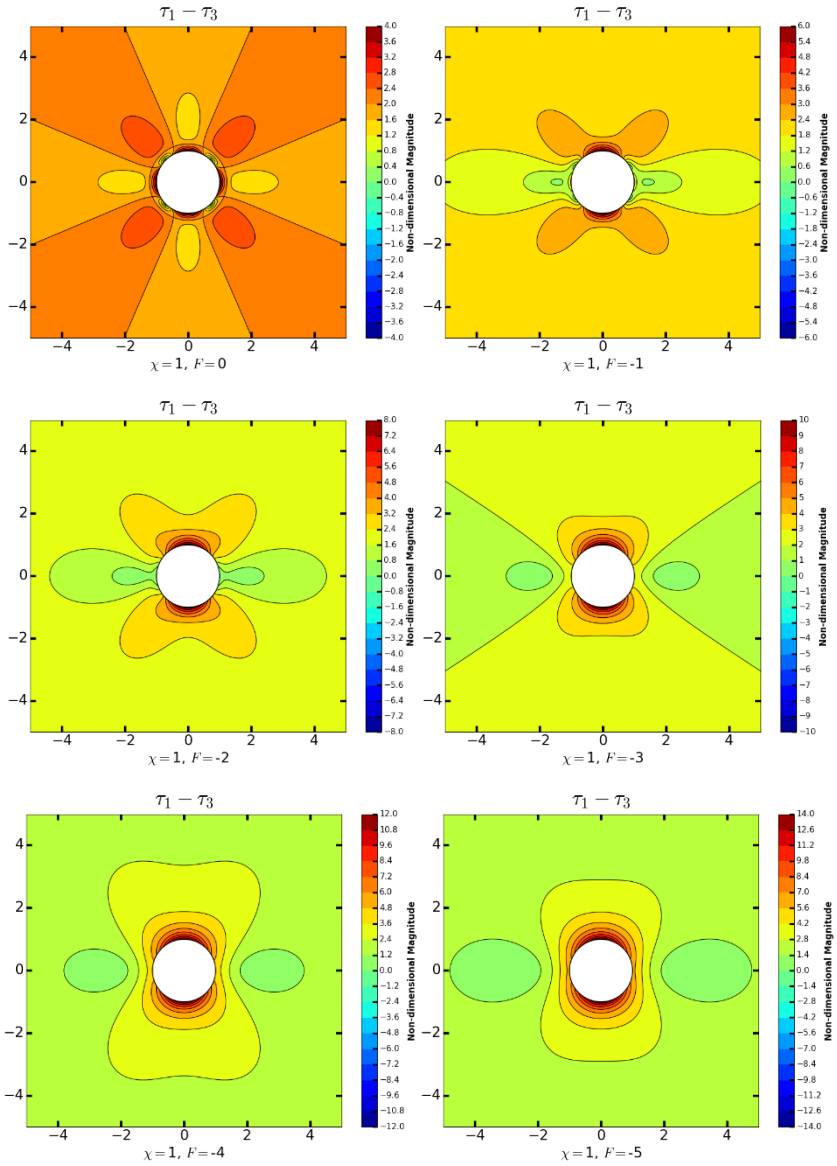

Figure 57: The principal deviatoric stress differentials are shown for plane bi-axial far-field stress (χ=1) and underbalanced borehole net fluid pressures -5≤F≤0. The contours represent the difference between the non-dimensional deviatoric principal stresses $(\tau_1 - \tau_3)$, where the solutions are normalized by far-field τ_1. Distances are non-dimensional, normalized by the radius of unit length.

6.4 Principal stress trajectories

The principal stress trajectories around underbalanced boreholes form a fracture cage, inside which all tangential stress is compressional. The maximum principal stress τ_1 trajectories form closed elliptical rings around the borehole, so that, if an initial crack were to form at the wellbore, it would redirect around the borehole if not initially long enough to protrude beyond the fracture cage region. This behavior has been described (Kogsbøll et al., 1993) in regard to tortuosity, which causes a loss of wellbore pressure when a fracture redirects too sharply and the proppant is unable to navigate the sharp-curved channel which leads to screenout of the pumping fluid. Tortuosity primarily occurs when a borehole is not able to be drilled in the direction of least principal stress (so that perf guns can direct orthogonal to this direction, in the direction of fracture propagation). Because of this, fractures will grow away from the borehole in the initial direction of the perforation guns, but at some distance, the fractures will become more influenced by the regional stresses, and will redirect in the direction of the far-field maximum principal stress. Cases have even been identified where the fractures redirected immediately and travelled around the borehole.

Although many authors have noted on the effects of tortuosity and the underlying reasons for it to occur (i.e., borehole not drilled along least principal stress; large horizontal stress anisotropies; weak cement bonding, etc.; Cleary et al., 1993; Kogsbøll et al., 1993), a physical understanding of the mechanisms behind the stress redirection in the near-wellbore region has been overlooked, and it is the opinion of the author that the fracture caging concept systematically explains why some fractures redirect around the wellbore.

A major proof of this concept derives from an extremely simple field practice used to prevent tortuosity. If tortuosity effects are observed, one recommendation is to simply use larger perforation guns (Cleary et al., 1993). Here, we are again drawn back to the dynamic numerical model which validated the fracture cage concept, and which showed that a short initial crack would redirect around the borehole and not escape the fracture cage, whereas the longer crack was initially long enough to extend beyond the fracture cage, and was therefore able to propagate away from the borehole, outside the influence of the fracture cage.

The following set of figures shows principal stress trajectories for uniaxial far-field stress (χ=0) and underbalanced borehole net pressures. At F=-1, the fracture cage is fully formed, with compressional τ_1 (blue) trajectories redirected around the borehole. If a fracture were to form, it would propagate along a τ_1 trajectory, possibly circumferentially around the hole. Shear/compressive failure is likely and the mud weight should be increased to lower the tangential stress and reduce the chance of failure. As $F \rightarrow -5$, the fracture cage grows larger, with the neutral points occurring at greater distances from the borehole.

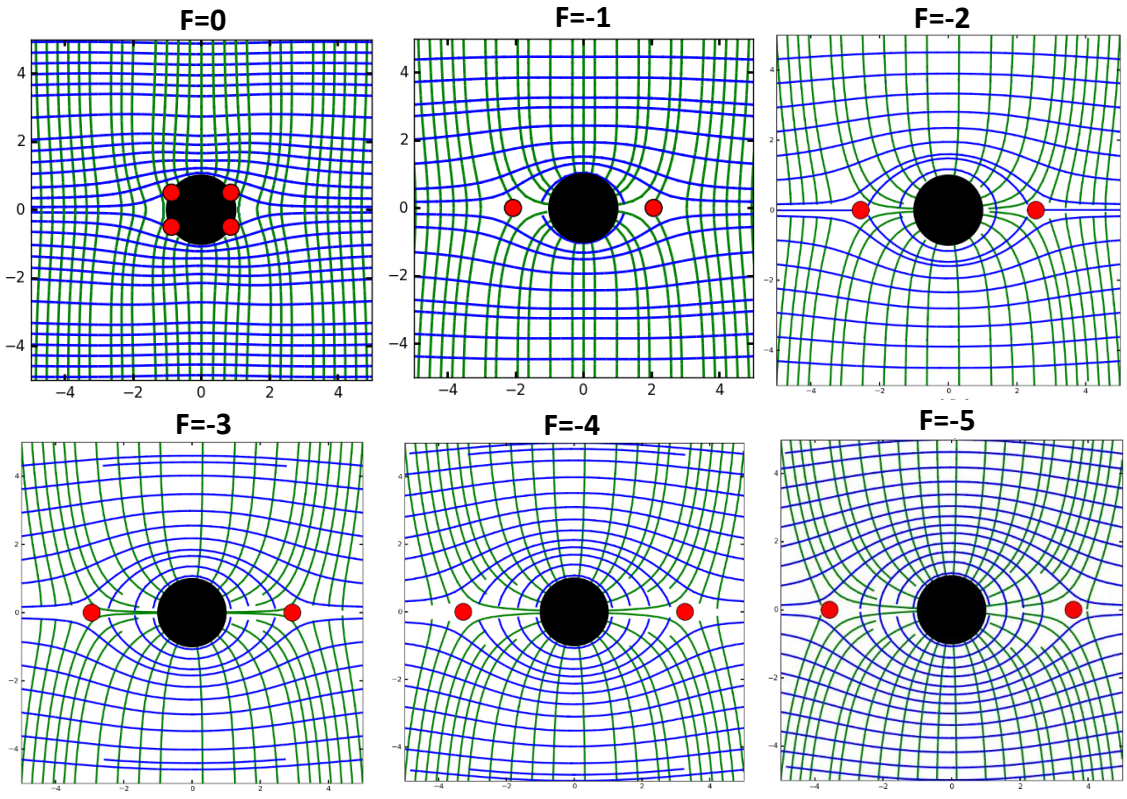

Figure 58: Principal stress trajectories are displayed for χ=0 and -5≥F≥0. The maximum principal stress τ_1 (blue trajectories) is oriented along the horizontal and the minimum principal stress τ_3 (green trajectories) is directed along the vertical. Neutral points are indicated by red dots. The borehole (black circle) is centered and given unit radius. Distances are non-dimensional, normalized by the borehole radius. For F≤-1, the τ_1 (blue) trajectories form closed elliptical rings around the borehole, bounded by the two neutral points.

In Figure 59(a-f), the same Frac Numbers are shown but for a bi-axial plane stress boundary condition. A few significant differences in the stress trajectories exists. First, when F=0, the neutral points are succinctly located around the borehole at multiples of θ=45º, perfectly balanced between the two far-field principal stress directions. Because failure is most likely to occur away from the neutral points, failure is probably least likely

under these conditions. When F=-1, a fracture cage has still not formed, and the four neutral points still exist along the borehole rim; however, now they occur at an angle $\theta=30^{o}$ in relation to the τ_1 far-field direction. Thus, they are moving towards the eventual location that neutral points occur in underbalanced borehole (direction of maximum principal stress). When F=-2, a unique situation arises in that two neutral points occur – one at the borehole wall, and one a short distance away from the hole along the same principal axis. For $F\leq-3$, the fracture cage is in full effect and grows in size for more negative F-values, just as we observed for the uniaxial case. Notice that the fracture cage is much smaller for the bi-axial plane stress condition. There are two takeaways from this: (1) A fracture initiated in an underbalanced borehole is more likely to escape the fracture cage when bi-axial plane stress ($\chi=1$) conditions exist because the initial fracture doesn't need to be as long to be beyond the cage and (2) borehole instabilities are more likely to occur for wells in bi-axial plane stress conditions because the tangential stress is significantly more compressive for $\chi=1$ compared to $\chi=0$ for the same Frac Numbers.

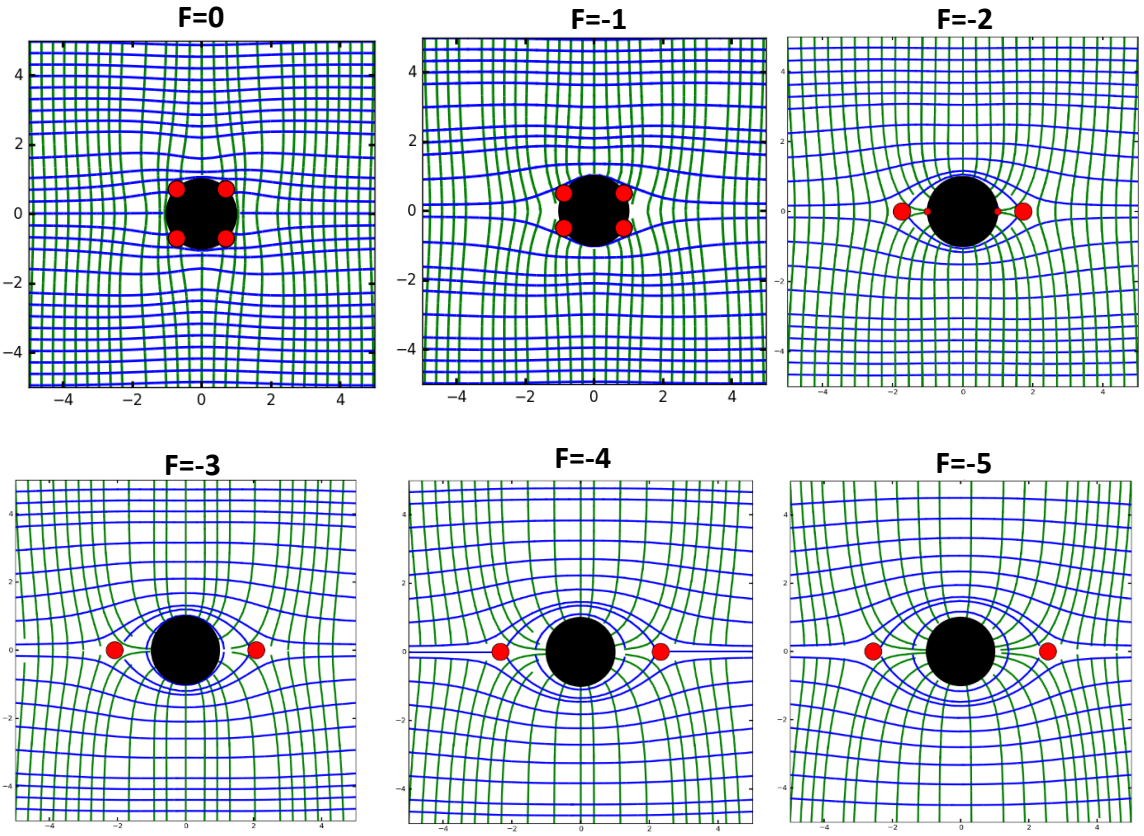

Figure 59: Principal stress trajectories are displayed for χ=1 and -5≥F≥0. The maximum principal stress τ_1 (blue trajectories) is oriented along the horizontal and the minimum principal stress τ_3 (green trajectories) is directed along the vertical. Neutral points are indicated by red dots. The borehole (black circle) is centered and given unit radius. Distances are non-dimensional, normalized by the borehole radius. For F≤-2, the τ_1 (blue) trajectories form closed elliptical rings around the borehole, bounded by the two neutral points. Observe that for F=-2, neutral points occur at the borehole wall, and a short distance into the host rock.

7. POROELASTIC EFFECTS

Understanding pore pressure effects, particularly in unconventional plays, is critical in executing a safe drilling strategy and for accurate production modelling. In conventional explorations, the most common source of overpressure is disequilibrium compaction, where porosity is preserved in mud rocks as pore fluids take on additional overburden load (Couzens-Schultz et al., 2013).

The poroelastic effects exerted on the excavated hole must be accounted for in any serious stress analysis model. The existence of a pore pressure tends to shield the rock from compressive failure by reducing the effective stress. However, increasing pore pressure also reduces the strength of the rock. At the time the hole is drilled, Cheng et al. (1993) gives the pore pressure distribution as

$$p = p_o + \frac{1}{2}(\tau_1 - \tau_3)\frac{4}{3}B(1+\nu_u)c^2\cos 2\theta \tag{19a}$$

which when normalized by τ_1 reduces to

$$p' = p'_o + \frac{1}{2}(1+\chi)\frac{4}{3}B(1+\nu_u)c^2\cos 2\theta \tag{19b}$$

where we observe that the deviatoric stress contributes to the initial pore pressure field. Here, p'_o is the non-dimensional virgin pore pressure normalized by τ_1, $B = \Delta p/P$ is the Skemptom pore pressure coefficient (Skempton, 1954) which is defined as the ratio between the pore pressure rise, Δp, and the mean stress, $P = (\sigma_1 + \sigma_1 + \sigma_3)/3$; and ν_u is the undrained Poisson ratio.

The pore-fluid pressure effectively reduces the stress in all directions. The effective tangential and radial stresses are defined as

$$\tau_r^* = \tau_r' - p' \tag{20a}$$

$$\tau_\theta^* = \tau_\theta' - p' \tag{20b}$$

Note that $\tau_{r\theta}'$ is unchanged by the pore-fluid pressure but we will still now adopt the notation $\tau_{r\theta}^*$. Also, observe that $\tau_r^* - \tau_\theta^* = \tau_r' - \tau_\theta'$ so that the pore-fluid pressure doesn't change the differential stress and instead only lowers the confining pressure. Increased pore fluid pressure moves the Mohr circle closer to the failure envelopes (Fig. 4). It should especially be noted that the effective stress should not be confused with the deviatoric stress, which would be obtained by subtracting the average pressure, *P* (Eq. 2), from the total stress σ. It is essential that it is recognized that the pore pressure, *p*, not only acts in the pores, but also in the particles, which are fully surrounded by pore fluid.

The pore pressures, as calculated using Eq. 19b, are shown in the subsequent sets of figures, with uniaxial stress states in Figure 60a-e, and bi-axial plane stress in Figure 61a-e. The dimensionless pore pressure magnitudes are shown as contours in the same way that the principal, radial, and tangential stresses were resolved. The magnitudes in these pore pressures would be subtracted from the effective stresses. The poroelastic effects are magnified, and the pressure more compressive, in the in the τ_1 direction for $\chi \to +1$, but there is also more negative (tension) pressure in the direction of least principal stress for these same χ values.

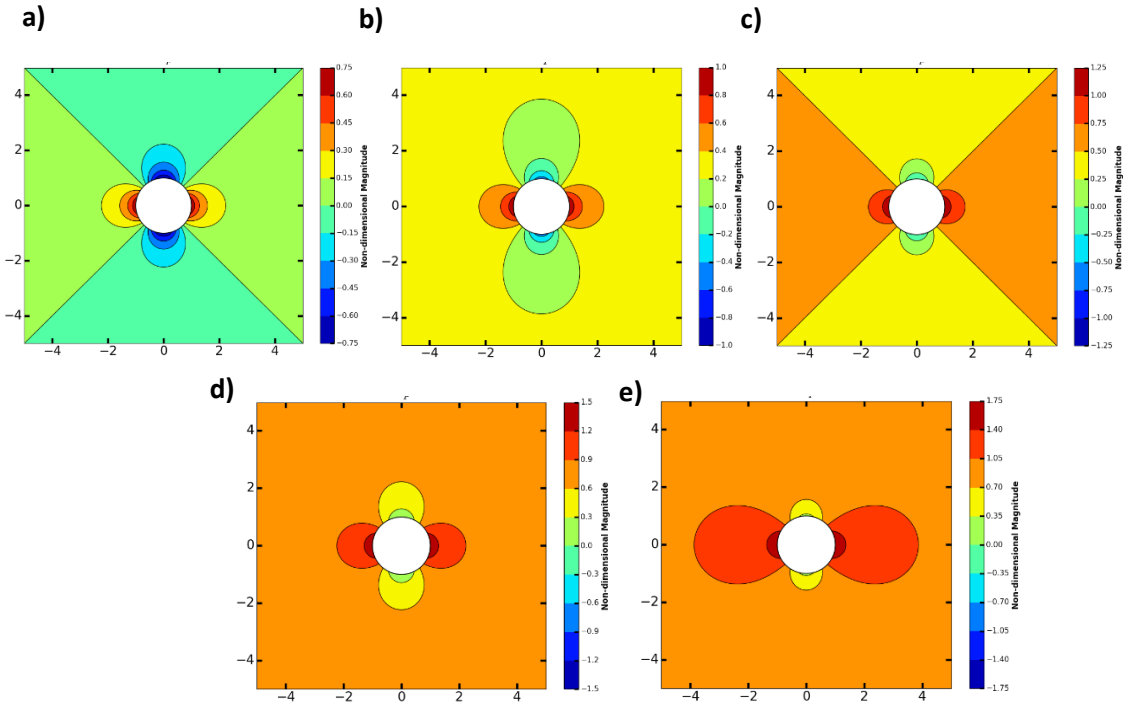

Figure 60: Dimensionless pore pressure magnitude contours for uniaxial far-field plane stress conditions (χ=0) and various virgin pore pressures, p_o are shown. The solutions come from Eq. 6, using B=0.8 and ν_u=0.4. **a:** p_o=0, **b:** p_o=0.25, **c:** p_o=0.5, **d:** p_o=0.75, **e:** p_o=1

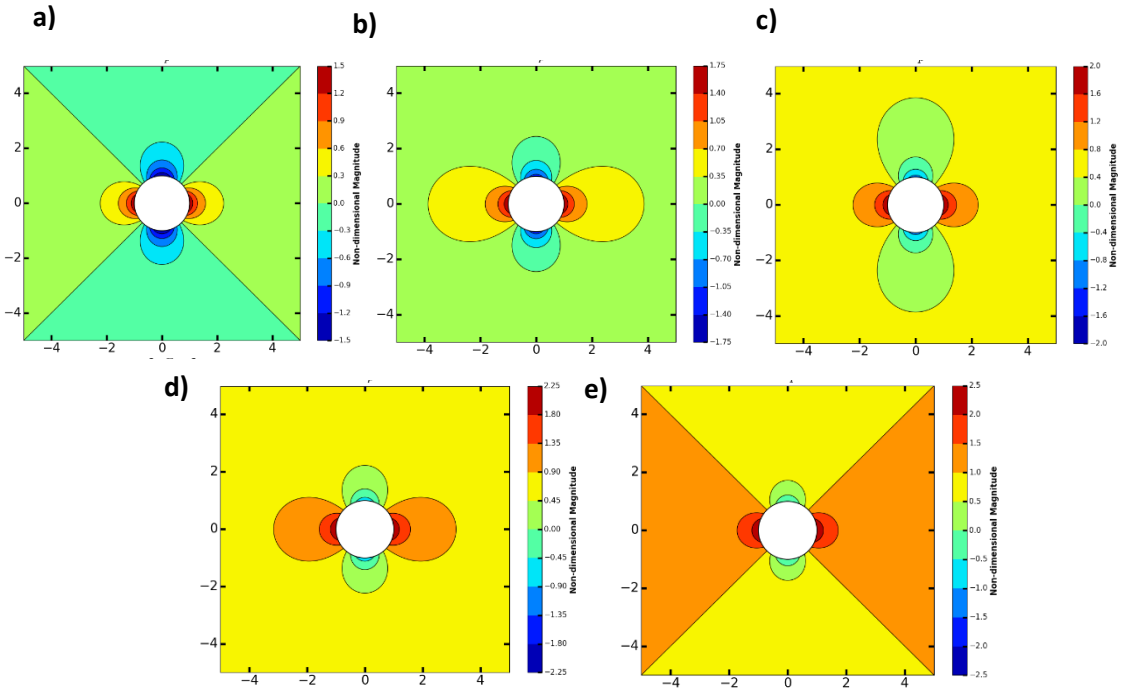

Figure 61: Dimensionless pore pressure magnitude contours for uniaxial far-field plane stress conditions (χ=0) and various virgin pore pressures, p_o are shown. The solutions come from Eq. 6, using B=0.8 and ν_u=0.4. **a:** p_o=0, **b:** p_o=0.25, **c:** p_o=0.5, **d:** p_o=0.75, **e:** p_o=1

Porosity can reduce the compressive stress by several MPa. However, the poroelastic effects do not alter the orientations of the principal stresses (Schutjens et al., 2012), and therefore they also do not alter the slip line orientations. Thus, the dimensionality of our problem is greatly reduced in that poroelastic effects need not be considered when estimating direction of principal stresses based on breakout angle and geometry. Poroelastic effects must, however, be taken into account when estimating principal stress magnitudes, as the porosity will increase the depth of failure into the host rock. The null effect of the porosity on stress orientations is readily observed in the following way. First, using simple notation, we will reduce the total stresses to effective stresses as follows:

$$\sigma'_{xx} = \sigma_{xx} - P_p \tag{21a}$$

$$\sigma'_{yy} = \sigma_{yy} - P_p \tag{21b}$$

$$\sigma'_{xy} = \sigma_{xy} \tag{21c}$$

where σ' are effective stresses, σ are the total stresses and P_p is pore pressure. If we then compare the principal stress orientations, β, (Eq. 16) for the effective and total stresses, we see that

$$\begin{aligned}
\beta_{\text{Effective}} &= \frac{1}{2}\tan^{-1}\left(\frac{2\sigma'_{xy}}{\sigma'_{xx} - \sigma'_{yy}}\right) && \text{(Effective stresses)} \\
&= \frac{1}{2}\tan^{-1}\left(\frac{2\sigma_{xy}}{(\sigma_{xx} - P_p) - (\sigma_{yy} - P_p)}\right) \\
&= \frac{1}{2}\tan^{-1}\left(\frac{2\sigma_{xy}}{\sigma_{xx} - P_p - \sigma_{yy} + P_p}\right) \\
&= \frac{1}{2}\tan^{-1}\left(\frac{2\sigma_{xy}}{\sigma_{xx} - \sigma_{yy}}\right) = \beta_{\text{Total}} && \text{(Total stresses)}
\end{aligned} \tag{22}$$

which confirms that the porosity does not affect the orientation of the principal stresses, and by extension, also will not alter the slip line orientations.

8. WELLBORE INSTABILITY

In engineering practice, a linear poroelasticity stress model in combination with a rock strength criterion is commonly used to determine the minimum and maximum mud pressures required for ensuring wellbore stability. Therefore, a main aspect of wellbore stability analysis is the selection of an appropriate rock strength criterion. Borehole stability problems continue to be extremely important to study (e.g., Gnirk, 1972; Bradley, 1979; Guenot, 1989; Santarelli et al., 1992; Ong and Roegiers, 1993; Maury, 1994; Last et al., 1995).

Based on linear elasticity, maximum stresses occur in the wellbore wall. Therefore, borehole instability is expected to initiate at the borehole wall. Reduction of mud pressure, corresponding to lower confining pressures, increases the potential for shear failure. On the other hand, increasing the mud pressure above a certain limit causes tensile failure to occur. This discussion indicates that there is a safe operating window for the mud pressure to stabilize the borehole. The lower limit for this window (collapse pressure) corresponds to shear failure and the upper limit (fracture pressure) precludes tensile failure.

Tensile failure occurs when the minimum effective stress reaches the tensile strength of the rock**.** In general, most sedimentary rocks have a rather low tensile strength. Experiments and measurements in the laboratory indicate that tensile failure is typically only a few MPa or less, and in several applications, is even assumed to be zero. Thus, tensile failure is not often measured directly on sandstone cores. Values are typically derived from indirect measurements. However, Muller and Pollard (1977) adopted a tensile failure strength of |-100| MPa, quoting groundbreaking work by Handin (1966).

Recent work has shown that tensile strengths of rocks may vary with the testing device used (Perras and Diederichs, 2014), and has further indicated that tensile strengths for crack initiation in sedimentary rocks is generally much lower than 100 MPa, with measurements ranging between 17 MPa for siltstone and 52.3 MPa for schist. Tensile failure occurs when

$$\tau_3 = -T_o = \frac{2S_0}{(\mu^2 + 1)^{1/2} + \mu} \tag{23}$$

where T_0 is the tensile strength. Because the horizontal stress difference is smaller in a normal or reverse-faulting stress state than for a strike-slip stress state, tensile failure is less likely in these faulting regimes unless a wellbore is inclined.

The wellbore stress concentration decreases as a function of radial distance from the wellbore wall. Thus, the zone of failed rock will only extend to a certain depth away from the well. Once the rock has failed, however, the stresses are re-concentrated around the now broken-out wellbore, and it is possible (depending on the residual strength of the failed rock, which determines whether it can support stress) that additional failure will occur. One important thing to keep in mind is that even if the rock has failed, it may not lead to drilling difficulties. In practice, raise the mud weight to the economic limit of performance. If borehole pressure is high enough to cause the hoop stress to go into tension, the borehole is pushed open and we suffer lost returns. Reduce the mud weight or use treatments that increase hoop stress.

Hydraulic fractures are created by pressure, not rate. Often, rate is used to help generate the required pressure, but it is nonetheless the pressure that opens the rock. Over a long, perforated interval, fractures can form anywhere that the fluid pressure exceeds the

local fracture gradient. Generally, the rock will have a weakest point where the initial fracture will form from. However, if the pressure continues to rise, other fractures may initiate from other points as well, and these fractures will eventually align with their natural direction. Every perforation is a potential source of fracture initiation. Many of these fractures will be very small, but some of them can be large enough to take a significant amount of the treatment fluid. This effect – known as tortuosity – remains one of the biggest challenges faced by shale and tight gas hydraulic-fracturing treatments. Tortuosities lead to high near-wellbore frictional pressure loss, premature screenouts, reduced treating rates, and poor production results (Denney, 2012).

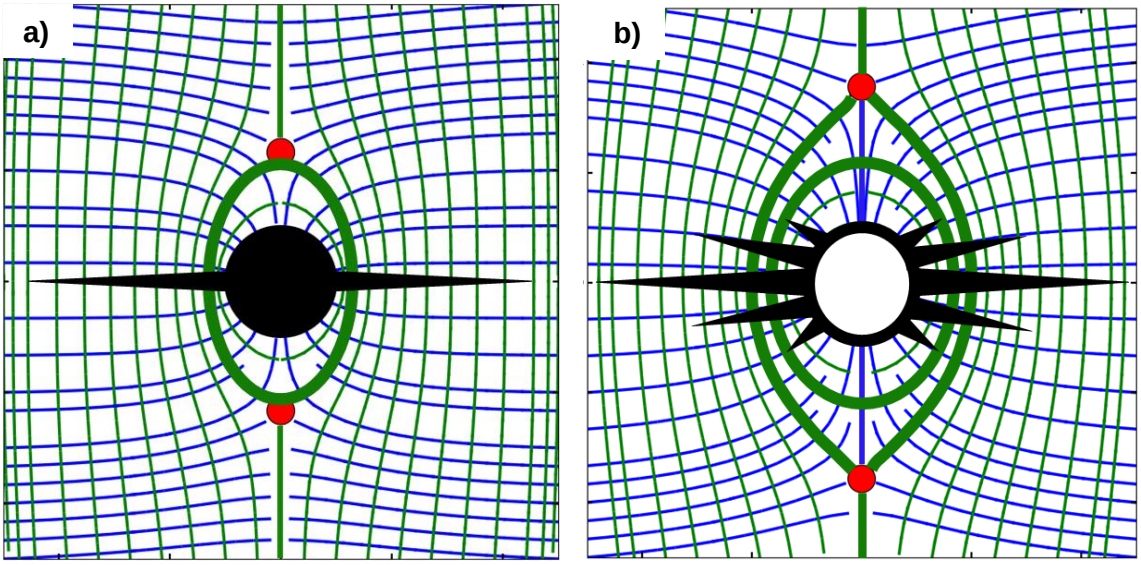

Figure 62: Stress cages are shown around two overbalanced wellbores. **a:** χ=1 and F=4. Based on tensile failure criteria, typical bi-winged fractures are expected to occur as shown (in the direction of maximum principal stress). **b:** χ=0 and F=5. The uniaxial stress condition provides lower stress concentrations at the wellbore than if bi-axial plane stress conditions prevailed. Bi-winged fractures are anticipated; however, if injection occurs very rapidly, multi-fractures are possible, as indicated.

Stress-induced wellbore breakouts form because of compressive wellbore failure when the compressive strength of the rock is exceeded in the region of maximum compressive stress around a wellbore. If the rock inside the breakout has no residual strength, the failed rock falls into the wellbore and gets washed out of the hole. The shape of these cuttings (Fig. 63) can be diagnostic of the mode of wellbore failure. If hoop stress exceeds the rock strength, the rock breaks and the hole enlarges. The mud weight must be raised to prevent such failure. Near misses should be exploited to trigger real-time decisions and to redesign borehole quality.

The hidden costs associated with reaming or circulating time are often larger than the trouble time associated with instability. Hole enlargement limits rate-of-penetration (ROP) by limiting the rate at which cuttings can be transported without seeing packoffs. Measured pressure drilling (MPD) may help prevent instability. Also, limit pulling speeds and swab. Stability mud weight should be modeled for critical wells to ensure they are feasible. However, real-time decisions should be based on cavings surveillance (Fig. 63). The driller should react immediately to blocky material. Develop directional plan and detailed well trajectory path. Stability mud weight will depend on the angle and azimuth at which the formation is being drilled (not accounted for in this study). Use the above data in a stability model to predict full stability mud weight. Conduct sensitivity analysis over a reasonable range of parameters. If possible to obtain DCM or LWD sonic data, revise the model while drilling. Monitor cavings while drilling to confirm or refine the model. Raise the mud weight immediately if cavings are blocky. During any drilling operation, real-time recognition and response practices are critical.

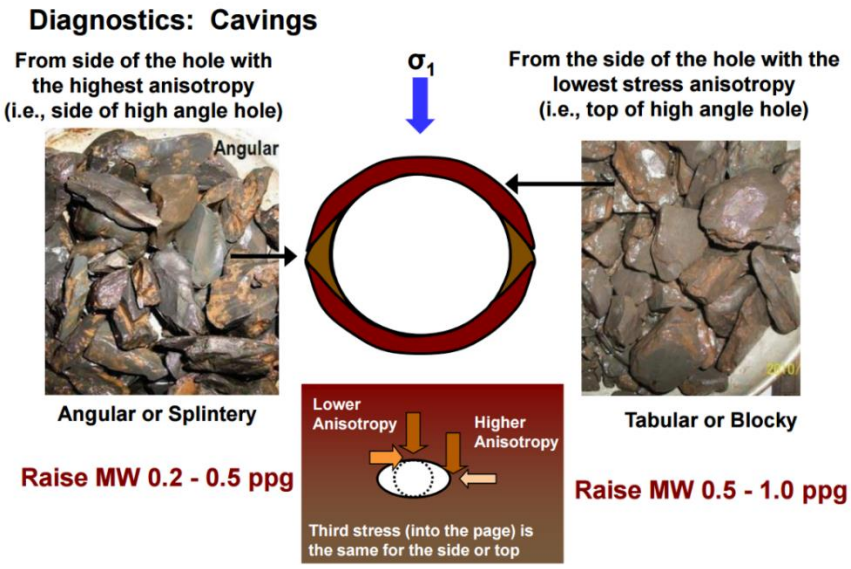

Figure 63: Cavings during drilling are a useful tool for diagnosing borehole stability in real-time. If the cavings are angular or splintery, the mud weight only needs to be raised slightly (~0.2-0.5 ppg). If the cavings are tabular or blocky, on the other hand, the mud weight must be raised immediately (between 0.5-1.0 ppg) to avoid breakout. Reprinted with permission from Fred Dupriest (2017).

Additionally, the rock can fail when the pumps are shut off, allowing the hoop stress to increase. Shutting the pumps off is similar to a violent volcanic eruption which leaves a caldera where a volcanic cone used to be. The magmatic pressure pushes out on the surrounding rock, keeping volcano from collapsing in on itself. If the pressure gets too high, the volcano may erupt so violently that there is no longer enough pressure to prevent this. The volcano collapses in on itself, forming a caldera (Fig. 64), which elongates in the direction of least principal stress. Similarly, when the pumps are shutoff, mud is no longer circulating and the pressure inside the borehole becomes inadequate to prevent borehole collapse.

Figure 64: Satellite image of the caldera around the shield volcano on Fernandina, an island of Galapagos. As magma exited the chamber, the conditions went underbalanced when the internal pressure was insufficient to keep the hole from collapsing.

Stress functions provide appropriate descriptions of the stresses developing in the elastic rock near the wellbore. Stress functions are useful for application to elastic materials if it can be assumed that the stress field is time-independent until the moment of incipient failure. Rheological studies have revealed that rocks at shallow crustal depths fail brittle after the elastic deformation limit is reached, while ductile creep is favored at deeper crustal levels (Byerlee, 1978). Modern laboratory data on rock mechanics suggest that the criterion for frictional slip is largely independent of the rock type (Byerlee, 1978; Brace and Kohlstedt, 1980). The brittle ductile transition occurs at 5 to 8 km depth dependent of the local geothermal gradient. Consequently, most boreholes do not enter the brittle ductile transition and ductile flow can be ruled out, except when rock salt is penetrated, which flows ductile with a low yield stress and at very shallow depths (Weijermars et al., 1993). For rocks deforming at depths that allow ductile creep, the stress

field is continually changing dynamically, and stream functions provide a more appropriate description (Weijermars and Poliakov, 1993) – but there a strong analogy between stress functions and stream functions links these analytical solutions.

The envelopes that represent rock failure as a function of confining stress are linearized with the Mohr failure criterion given in Eq. (24). Suppose that the rock has a preexisting plane of weakness whose outward unit normal vector makes an angle θ_b with the direction of the maximum principal stress, τ_1 (Fig. 14). The criterion for slippage to occur along this plane is (Zoback, 2007):

$$|\sigma_s| = S_0 + \mu\sigma_N \tag{24}$$

where σ_s is shear stress, σ_N is the normal stress. Failure will not occur on any plane for which $|\sigma_s| < \mu\sigma_N + S_o$. The sign of the shear stress only effects the direction of sliding after failure, so the absolute value of σ_N appears in the failure criterion, although it is often convenient to ignore the absolute value sign in mathematical manipulations. An example of the shear failure criterion based on cohesion sensitivity analysis is shown in Figure 65.

The angle of internal friction is fairly consistent within a particular rock type, if the rock is consolidated. Tables can be used (Senseny and Pfiefle, 1984; Atkinson and Meredith, 1987; Plumb, 1994) to provide initial estimates of values. The friction angle can also be estimated using correlations with physical properties such as porosity (Plumb, 1994) but with less success. The decrease in accuracy comes from the fact that lithology, not a particular physical property, is the primary determining factor for friction angle (Economides, 2000).

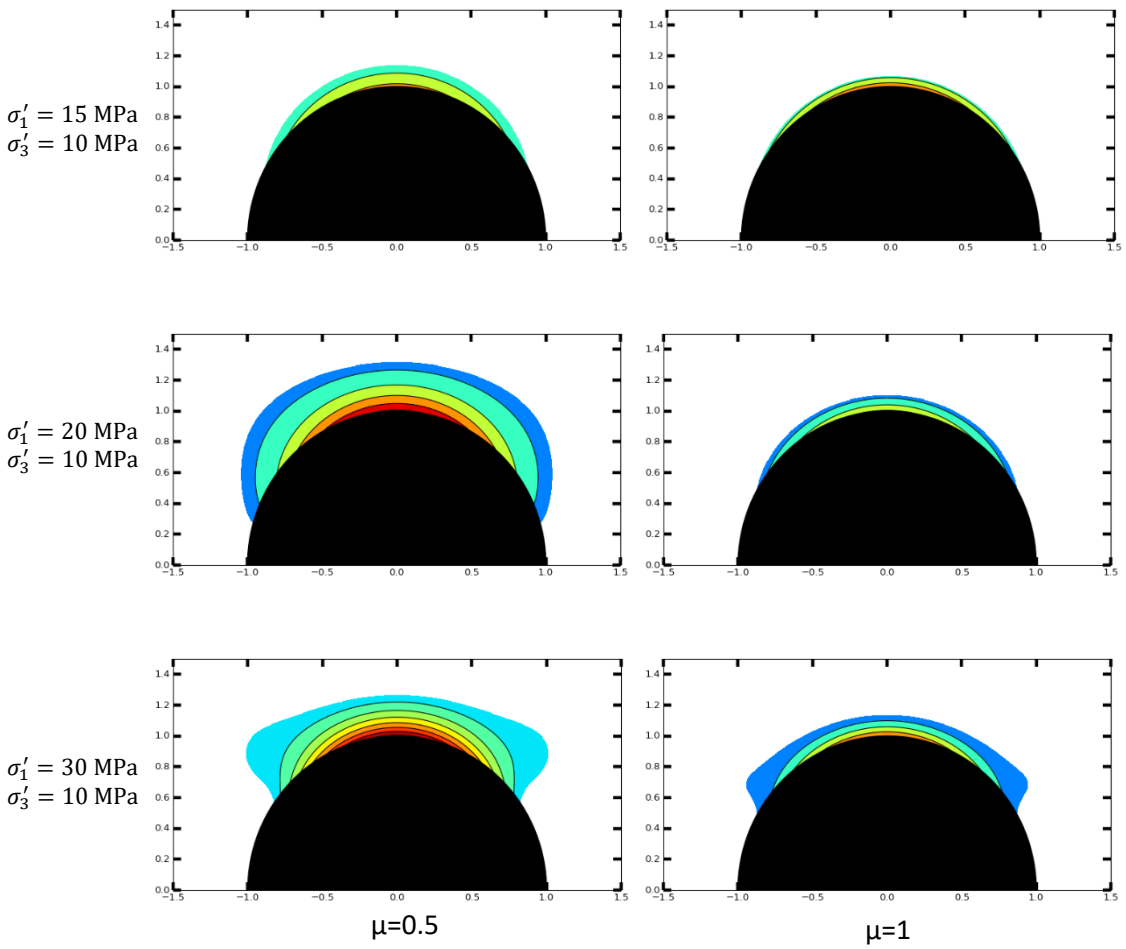

Figure 65: Contour lines mark the region susceptible for compressive failure for different cohesion values. The images in the ***Left column*** use an angle of internal friction μ=0.5, while those in the ***Right column*** use μ=1. The ***Top row*** is for effective stresses $\sigma_1' = 15\ MPa,\ \sigma_3' = 10\ MPa$; the ***Middle row*** shows $\sigma_1' = 20\ MPa,\ \sigma_3' = 10\ MPa$; and the ***Bottom row*** displays $\sigma_1' = 30\ MPa,\ \sigma_3' = 10\ MPa$. Adapted from Zoback et al. (1985).

The Mohr-Coulomb failure criterion can be rewritten in terms of the effective principal stresses to give σ_1 at failure in terms of σ_3:

$$\sigma_1' = \sigma_c + N_{\phi_b} * \sigma_3' \tag{25}$$

where the coefficient of passive stress N_{ϕ_b} is

$$N_{\phi_b} = \tan^2\left(\frac{\pi}{4} + \frac{\phi_b}{2}\right) \tag{26}$$

and the uniaxial compressive strength is then given as

$$\sigma_c = 2S_o\sqrt{N_{\phi_b}} \tag{27}$$

The strength of a rock is the stress at which the rock fails (i.e., the rock loses its integrity). This strength obtained with a uniaxial test is called the uniaxial compressive strength σ_c (UCS). The overall strength of rocks is a relationship between the principal effective stress components. This relationship is called the failure criterion, and its graphical representation is called the failure envelope (Fig. 4). For sandstones, the UCS can additionally be estimated from correlations using sonic data (e.g., Kowalski, 1975; Economides, 2000).

For any plane with a strike-slip parallel to σ_2, the shear and normal stresses are defined as

$$\sigma_s = \frac{1}{2}(\sigma_1 - \sigma_3)\sin 2\theta_b \tag{28a}$$

$$\sigma_N = \frac{1}{2}(\sigma_1 + \sigma_3) + \frac{1}{2}(\sigma_1 - \sigma_3)\cos 2\theta_b \tag{28b}$$

where θ_b is the angle between the plane and σ_1. Shear joints form close to the direction of maximum shear stress, which is in two conjugate planes at 45º to σ_1 and σ_3 (Fig. 4). However, the angle of internal friction of most rock is actually closer to 30º to 40º, rather than 45º. The Mohr-Coulomb failure agrees with this and predicts that the planes of shear failure will occur at acute angles to the σ_1 plane (Fig. 66). If we know the value of μ, we can find the angle θ_b in the following way:

$$\theta_b = 90° - \frac{1}{2}\phi_b \quad \text{and} \quad \phi_b = \tan^{-1}\mu \tag{29}$$

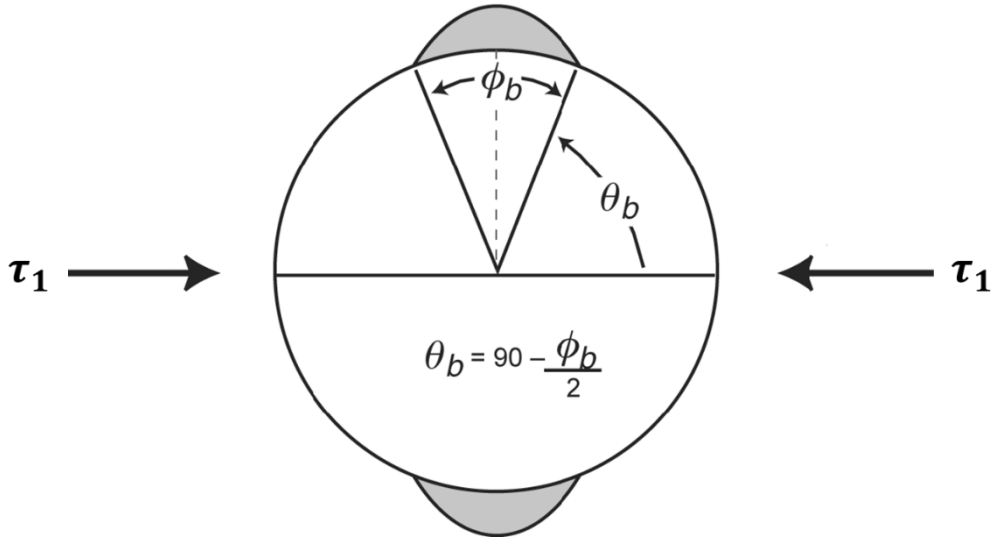

Figure 66: The relationship between the failure angle and its rotation from the maximum principal stress direction is illustrated. Adapted from Moos (Fig. 1.43, 2006).

The ***slip line*** orientations can be resolved by adding θ_b to the principal stress orientations, β (see Eq. 16), and plotting this direction everywhere in the plane of view around a borehole. The angle at which the slip lines intersect along the σ_3-plane correspond to the angle observed on the cavings after shear failure. A drilling engineer can use this additional tool to back-calculate the in-situ stresses, pore and formation pressures, and rock properties. Slip lines can be calibrated with the Mohr-Coulomb failure criterion to show the slip lines only in the region that is predicted to fail (Fig. 62a, b) and can be compared with contour plots showing the extent of failure for varying properties (Fig. 62c, d) illustrates this property with various cohesion values.

Assuming that a Mohr-Coulomb failure criterion is appropriate for relatively brittle rocks, Fig. 67 shows the potential shear failure surfaces for the indicated stress field (a,b), and the zone of initial failure for a given cohesive strength, S_o (c,d). Comparison of the wellbore cross sections with the failure trajectories suggests that the surface of some breakouts is defined by a single shear fracture. It also has been demonstrated that wider and deeper breakouts will form as the maximum horizontal stress increases or as rock strength or mud weight decreases. While there is an increase in the stress concentration at the back of the breakout once it forms, any additional failure caused by that new stress concentration will result in an increase in breakout depth but will not change the width.

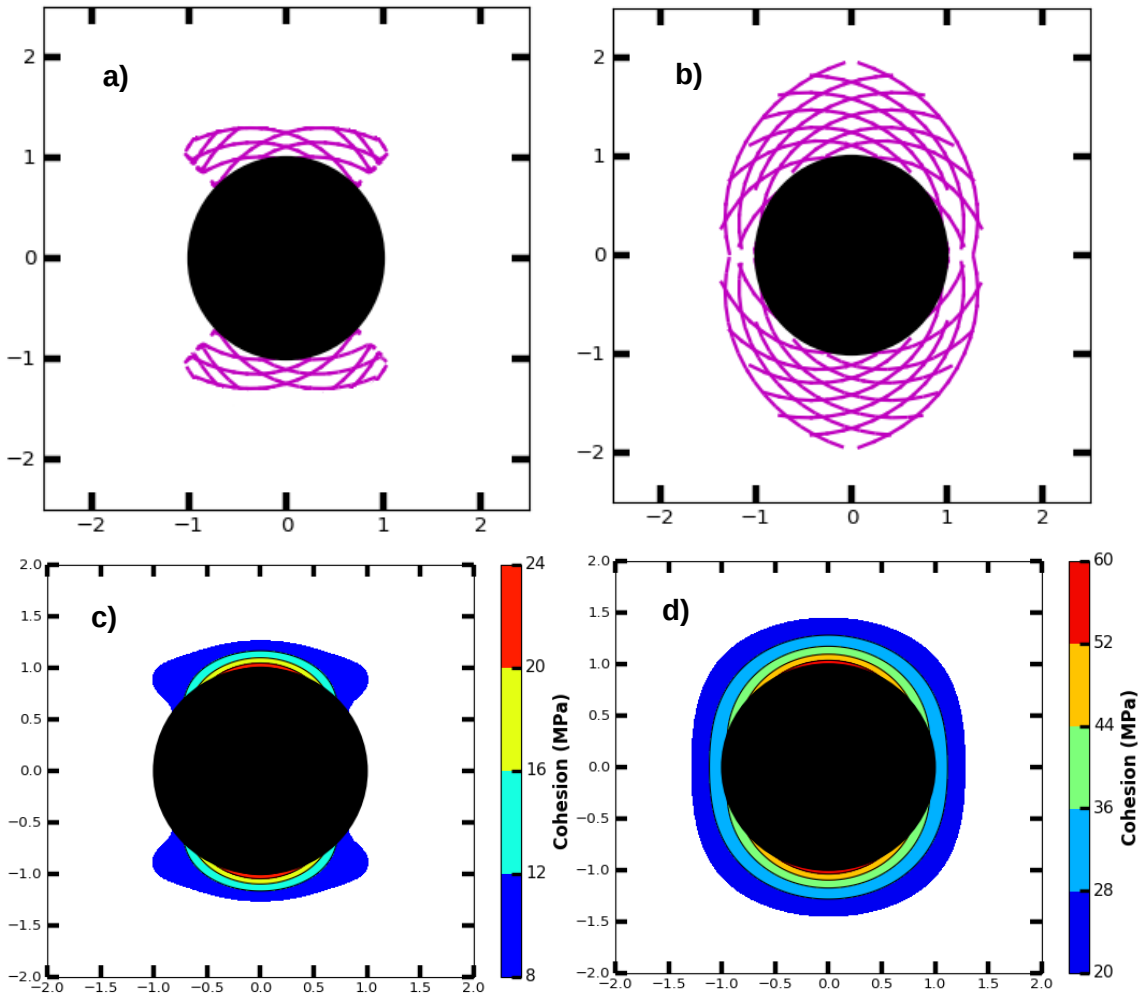

Figure 67: Slip lines illustrating preferential shear failure planes and the corresponding extent of failure region contoured by cohesion (MPa) values are shown. **(a)** and **(c)** Are for total stresses $\sigma_1 = 30\ MPa, \sigma_3 = 10\ MPa, P_{NET} = 0$. A minimum cohesion of 8 Mpa is asserted because if any smaller the failure nearly encompasses 360º. **(b)** and **(d)** show results for $\sigma_1 = 30\ MPa, \sigma_3 = 10\ MPa, P_{NET} = -30\ MPa$. By including the underbalanced borehole pressure, we see that the extent of failure increases substantially, with Cohesion = 30 MPa needed to keep the entire hole from collapsing at 360º.

Breakouts help establish the direction of the minimum principal stress. Additionally, the maximum and minimum principal stress magnitudes relative to the strength of the host rock can be established by measuring the size and shape of the

breakouts, which are recorded by dipmeters, and more precisely by televiewers. As the in-situ strength of rock and its state of stress are difficult to determine at great depth, observations of the size and shape of the breakouts and conditions under which they form could lead to estimation of these parameters, provided that a thorough understanding of the mechanisms involved in breakout formation become clear (Exadaktylos, 2003).

Hottman et al. (1979) were perhaps the first to attempt to quantify magnitudes of horizontal principal stresses from borehole breakouts (Guisiat and Haimson, 1992). Strong agreement of their estimations with other stress indicators led both Gough and Bell (1981, 1982) and Zoback et al. (1985) to further investigate the mechanisms of borehole breakouts from field and laboratory experiments. They concluded that size, shape and depth could be predicted by using Kirsch's (1898) elasticity solution and a linear Mohr–Coulomb failure criterion, which has been adapted and applied in this current study. Their work has been corroborated experimentally in two granitic rocks and also several limestones (Haimson and Herrick, 1985; Haimson and Song, 1993; Lee and Haimson, 1993; Herrick and Haimson, 1994). The laboratory studies confirmed that breakouts had a 'dog-ear' or 'V' shape and developed in the direction of the far-field least horizontal principal stress. This shape was found to be the result of dilatant multi-cracking tangential to the hole and subparallel to the maximum far-field horizontal stress (σ_H), followed by progressive buckling and shearing of detached rock flakes created by the cracks (Haimson and Kovacich, 2003). In a more complex model, Zheng et al. (1988; 1989) compared the stresses around the borehole to those required to cause failure according to a spalling

criterion for the immediate zone around the borehole wall, and the Mohr–Coulomb criterion for the remaining rock.

In addition to rock strength, porosity influences the final shape of borehole breakouts. In high porosity (ϕ > 20%) sandstones where fluids are circulating during drilling, long and extremely narrow slot-shaped "wormhole" breakouts (Fjaer et al., 2008; Zang and Stephansson, 2009) may form. Slot-shaped breakouts may involve compaction bands forming in the direction of the minimum stress springline (Haimson, 2007; Haimson and Kovacich, 2003).

9. WELLBORE STABILITY MODEL

The state of stress in the earth is one of the major factors influencing the stability of a well being drilled and the geometry of a hydraulic fracture. The state of stress can be described by three principal stresses that are perpendicular to each other: maximum principal stress, σ_1, intermediate principal stress, σ_2, and minimum principal stress, σ_3. Because the principal stress directions are orthogonal, the direction of two principal stresses automatically describes the direction of all of them. However, the description is complete only when the order is known (Fig. 68). The overburden stress, σ_v, is usually one of the principal stresses. The two other principal stresses are therefore horizontal. The azimuth of the minimum horizontal stress, σ_h, completes the description of the orientation of the stresses, because the maximum horizontal stress, σ_H, is horizontal and orthogonal to σ_h. What is missing is the order of the stresses. Is σ_v the maximum principal stress, σ_1, in which case σ_h is the minimum principal stress, σ_3, and σ_H is the intermediate principal stress, σ_2? Or perhaps σ_v is the minimum principal stress, or even the intermediate principal stress. Each of these cases corresponds to a different stress regime. A complete description of the state of stress is of particular importance because hydraulic fractures propagate perpendicular to the minimum principal stress. If σ_3 is horizontal, a vertical fracture will be created; if σ_3 is vertical, a horizontal fracture will be created; if σ_3 is inclined, an inclined fracture normal to it will be created.

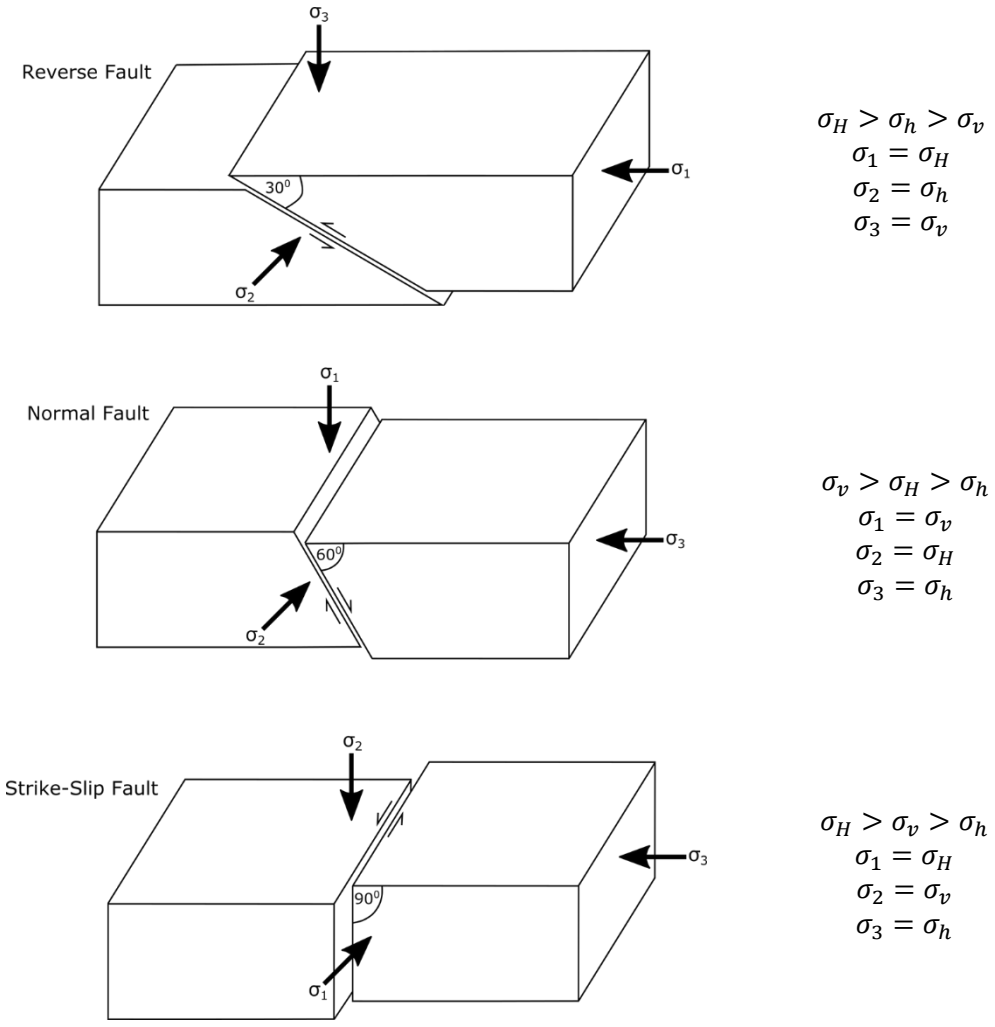

Figure 68: Simplified diagram of the three main tectonic environments and their associated faults. Adapted from Anderson (1905).

Borehole stability studies benefit from an integrated approach, as discussed in Section 2.1. The perfect wellbore is realized when breakout, ballooning, and bridging are avoided at all times and at every depth in the wellbore. Fig. 69(a-c) give wellbore images rendered based on caliper logs. Circulation complications occur when excessive variations in wellbore diameter cause large pressure drops during drilling (Fig. 69 b,c), which is why

the wellbore should remain smooth and perfectly cylindrical (Fig. 69a) at all times. Drilling the perfect wellbore comes closer to reality when:

- Physical properties and responses to elastic deformation are tested in the laboratory.
- Mathematical descriptions capture the physical state and responses to changes in boundary conditions for any particular initial state. Such descriptions can be analytical, semi-analytical or discrete-element based requiring numerical solutions.
- Input parameters (intrinsic rock properties, drilling fluid density, formation pressure, far-field stresses, boundary conditions) are known at all depths in the wellbore.

Obviously, the third requirement is the most challenging, which is why a flexible formulation is required. Starting with the non-dimensional Kirsch equations, as advocated in our study, is a useful first step for achieving the perfect wellbore.

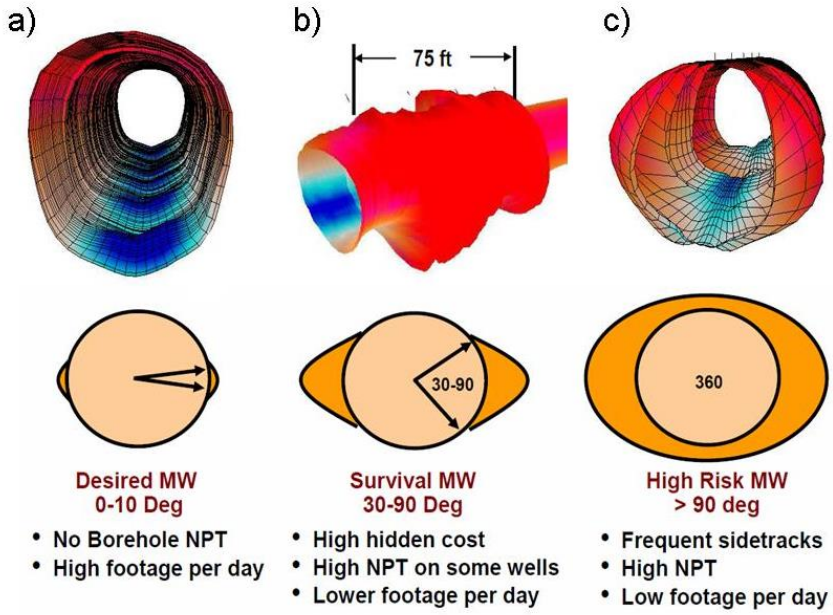

Figure 69: Examples of field measurements of wellbore shapes. **(a)** Smooth, nearly perfect wellbore, with almost no non-productive time (NPT) with correct mud weight during drilling; zero to only minor breakout resulting in high footage drilled per day. **(b)** Wellbore image with large variations in wellbore diameter leading to local pressure changes for drilling fluid moving up and down the wellbore. Such pressure drops frequently lead to caving obstructions, causing higher breakout angles and increased NPT, resulting in lower footage drilled per day. **(c)** Enlarged borehole due to spalling and massive breakout may need sidetracks to prevent borehole collapse. Obviously, NPT increases and footage drilled per day decreases accordingly. Reprinted from Dupriest et al. (2010).

Regardless of the borehole stability model used (e.g., Linear elastic, nonlinear, elastoplastic, purely mechanical, physicochemical), the following data are required:

- Rock properties (Poisson ratio, strength, modulus of elasticity)
- In-situ stresses (overburden, horizontal)
- Pore-fluid pressure and chemistry
- Mud properties and chemistry

Other than the mud data, the data are often compounded with problems of availability and/or uncertainties. However, sensitivity analysis can be conducted by assuming data for the many variables to establish safety windows for mud selection and design. The above data can be determined as follows:

1. Determine principle stresses over the interval [mechanical earth model (MEM)]
    a. Overburden - offset density log or regional correlations (Peška and Zoback, 1995)
    b. Minimum Horizontal - offset leakoff tests, observed integrity following lost returns events, or regional integrity correlations (Zhou, 1997)

The orientation of the minimum horizontal stress could be a consideration in planning the drainage pattern of the reservoir. But more importantly, the orientation of the principal stresses can vary significantly from one layer to the next and thereby enhance hydraulic fracture containment.

    c. Maximum Horizontal - reverse engineered from borehole ovality (Zoback et al., 1985)
    d. Pore pressure – offset data or seismic velocity correlation

2. Determine rock strength over the interval
    a. Offset dipole sonic correlation (most common)
    b. Shale “surface area” (m^2/gm) correlation (must develop correlation)
    c. Lab triaxial tests of cores (rarely available in shales)
    d. Analysis of wellbore failure, including cuttings analysis (Fig. 63)

A more detailed discussion of the methods used for determining the required above data is provided in the Appendix.

9.1 Modeling limitations

"All models are wrong, but some are useful" (Box, 1976) is a common aphorism in statistics. In all borehole stability models, the predicted stability mud weight is almost always wrong because there are significant uncertainties in many of the model inputs. Additionally, the assumptions made so that models can be solved mathematically introduce more error modeling challenges.

Some of the uncertainties can be summarized as follows. In reality, round holes and impermeable formations, which are fundamental assumptions in the Kirsch model, do not exist. Models do not accurately predict pore pressure changes in the near-wellbore, and so the effective stress and strength have errors. Most models assume elastic, or elasto-plastic behavior, but we do not have stress strain data for every foot of hole to fully define the stress strain relationship. We do not know the initial rock strength. We do not know strength anisotropy in every foot of hole. We do not know the principal stresses in every foot of hole. We cannot model time-dependent changes in rock strength. Overall, models tend to be overly conservative and predict higher mud weight than required. As a result, operations people lose faith in them and run lower mud weight. When the predicted mud weight is used and failure occurs, it is usually due to unexpectedly weak rock, not surprisingly high stress (Dupriest et al., 2010).

Some uncertainties will always remain in laboratory-determined parameters used analogously to the field situation, either because of the disturbance a core sample suffers during the coring and handling process or because of scale effects. There are also limitations on the use of simple constitutive laws to predict rock behavior for heterogeneous, discontinuous, time-dependent and/or weak formations.

Potential breakout mechanisms can be analyzed with these considerations in mind. First, if there is localization of failure along shear bands, it is likely that the initial breakout would have the appearance of the "pointed dog ears" speculated by Gough and Bell (1982). However, this initial breakout would trigger a process of additional degradation due to stress redistribution. This progressive failure mechanism cannot be accounted for when using the elastic stress distribution proposed by Zoback et al. (1985). Second, kinematic considerations could provide an explanation of why the breakouts do not appear to widen with depth, although they deepen. Third, if the mode of failure is ductile, and the material remains in place, elastoplastic analysis (Detournay and Fairhurst, 1982; Detournay, 1983) indicates that the direction of maximum closure can become parallel to the direction of the minimum horizontal in situ stress (i.e., 90º from the direction predicted by an elastic analysis). In this case, however, the elongated diameter of the borehole would be less than the nominal drilled diameter. Finally, it is unlikely that all the failed material will "disappear." Indeed, the borehole cross section would then evolve into a shape characterized by progressively higher stress concentration near the tips of the elongated axes (however, the size of the overstressed region would decrease). Hence some failed material needs to remain in place so as to provide a buildup of the radial stress. Therefore,

the only conclusion which could generally be derived from the elastic model proposed by Zoback et al. (1985) is the link between the location of the breakouts and the principal in situ stress directions. Attempts to relate size and shape of the breakouts to other characteristics of the stress field--as is done in the paper where a relation is proposed between the horizontal stress ratio, the angular width and maximum depth of the breakouts, and the friction angle of the rock--would require not only considerations of the geometrical effects and the failure mechanisms of the material but also considerations of such processes as borehole wall erosion by the drilling fluids.

10. CASE STUDY

The Midland basin hosts the 2nd most prolific oil reserve of the US (Keller et al., 1980; Gaswirth et al., 2016). Determining the far-field stress state in the Midland Basin is useful, because knowing and understanding the stresses around drill holes is crucial for optimizing three major stages in field development:

1. **Drilling:** Determining the optimal well trajectory, which reduces nonproductive time and helps constrain the mud weight window, requires knowing the present-day stress directions. The upper limit of the mud weight window is guided by the minimum horizontal stress. The lower limit of the mud weight needs to avoid underbalance to mitigate shear failure.

2. **Completion:** The propagation direction of hydraulic fractures is always normal to the minimum stress. Effective fracture stimulation for production optimization requires estimations of the regional stress orientations and magnitudes. A single tensional fracture running parallel to the maximum principal compressive stress can be induced by pumping fluid into the borehole to increase the fluid pressure. The hydraulic fractures form when the fluid pressure causes the least principal stress in the borehole wall to reach the tensile strength. As fluid continues to be pumped into the hole, the fracture extends farther into the host rock until the injection pressure becomes equal to the least principal stress.

3. **Production:** To ensure we have the longest possible field life, especially in enhanced oil recovery fields, we need to know the upper limit for the injection pressures to prevent reservoir damage and preserve cap-rock integrity.

Establishing Far-field stress orientation and magnitude. University Lands well 3-31-4H (API 42-461-37722) is situated in the Wolfcamp formation, Spraberry Trend Field, Midland Basin (Upton County, Texas). Total vertical depth (TVD) of the well is 8,365 ft and total measured depth (MD), including the horizontal section, is 14,725 ft. The total fractured length of the horizontal wellbore is about 6,000 ft. Within each stage, the designed stimulation stage interval is comprised of 3 perforation clusters, each about 60 ft apart. The wellbore itself is partitioned into 33 stages, each 60 ft apart. Consequently, the total wellbore section has 99 evenly spaced perforations, 60 ft apart.

Microseismic monitoring during multistage hydraulic fracturing can provide clear clues of the failure plane orientation in each frac stage (Fig. 70a). Recordings of the seismic activity monitored during the hydraulic fracturing of each of stages 21 to 33 (three perf clusters, each 60 ft apart, per stage) were processed to provide filtered, color-coded seismic event images for each of the frac stages (Fig. 70a, b). The minimum principal stress direction (both deviatoric τ_3 and total σ_3) is thus well constrained by the micro-seismic recording. The micro-seismic map shows a clear trend with the minimal principal stress oriented in NE-SW direction. Previous studies in the Midland Basin have established the occurrence of Late Paleozoic left-lateral strike-slip faults (Tai and Dorobek, 2000; Blumentritt et al., 2003, 2006), and the existing strike-slip faults may still facilitate regional strike slip tectonics at present (Bolden, 1984; Hoak et al., 1998). We therefore use the principle sketches of Fig. 71a,b to fixate the orientation of the intermediate principal stress normal to the ground surface. A wide range of near-wellbore stress trajectory patterns may occur depending on the far-field boundary stress conditions and

internal net-pressure contributions from the wellbore (Weijermars, 2011, 2013; Weijermars and Schultz-Ela, 2012, Weijermars et al., 2012, 2013, 2016).

The stress magnitudes can also be obtained from the leak-off test during hydraulic fracture stimulation. Treatment profiles for pressure, slurry rate, and proppant load are given in Fig. 72. The plot records a 3,000-psi leak-off pressure at the moment of hydraulic fracture initiation, which at moment of failure should equal the total minimum stress, $\sigma_3 \sim 20$ MPa. With σ_3 estimated from the leak-off test we can obtain τ_3 from the relationship $\tau_3 = \sigma_3 - P$, which requires a knowledge of P. Because $\tau_2 = 0$ (Fig. 71b), the pressure at depth is given by $P = \sigma_2$, with σ_2 determined only by the overburden load $P_{OVERBURDEN} = \rho g z v/(1-v)$. The vertical depth (TVD) of our wellbore is z = 8,365 ft (2,550 m), and adopting a Poisson ratio, $v = 0.4$, density, ρ = 3,000 kgm^{-3}, and g = 9.8 ms^{-2}, gives $P = P_{OVERBURDEN} = 50$ MPa. Substituting $\sigma_3 = 20$ MPa and $P = 50$ MPa into $\tau_3 = \sigma_3 - P$ gives $\tau_3 = -30$ MPa. The plane stress condition in the horizontal section (Fig. 71a) implies $\tau_1 = -\tau_3 = +30$ MPa. We can now estimate the principal stresses in the subhorizontal plane, with deviatoric stresses $\tau_1 = +30$ MPa and $\tau_3 = -30$ MPa, and the corresponding total stresses $\sigma_1 = \tau_1 + P = 80$ MPa and $\sigma_3 = \tau_3 + P = 20$ MPa. The vertical total stress $\sigma_2 = 50$ MPa and vertical deviatoric stress $\tau_2 = 0$ MPa.

Further support for finding the minimum and maximum stress magnitudes may come from mini-frac tests, which give the direction of tensile failure that is always in the plane normal to τ_3. Although the magnitude of the total stress σ_3 can be estimated from the pressure applied to reach failure, pressure leak-off tests applied in oil and gas boreholes show that such tests need to be interpreted with some caution, partly because of transient effects and partly due to the impact of equipment used (Rutqvist et al., 2000; Andrews et al., 2016).

The minimum total stress in the horizontal plane can be constrained by the leak-off test, but the maximum stress in that plane cannot be easily constrained apart from applying limiting values of stress difference required or crustal equilibrium (Zoback et al., 2003). However, the method explained above for estimating the largest principal stress in a strike-slip basin is straight forward. Additional clues on principal stress directions can be inferred from calliper logs showing breakout orientation, which is in the direction of the least principal stress (Bell and Gough, 1979). Image logs of wellbores can also reveal televiews of the orientation of drilling induced breakouts and/or tensile fracs (Zang and Stephansson, 2010).

a)

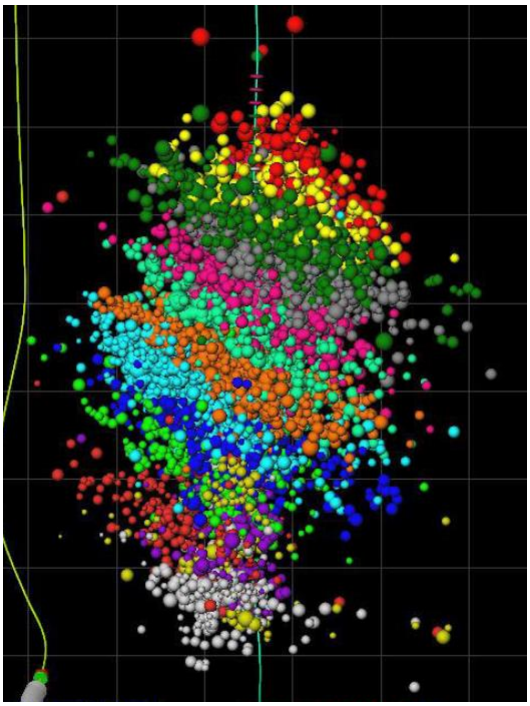

b)

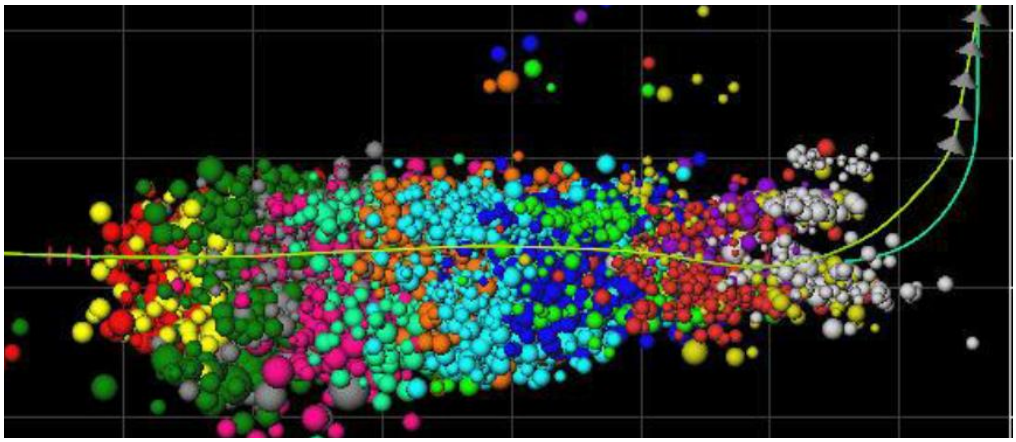

Figure 70 a: Map view of imaged micro-seismic events during hydraulic fracturing of each stage (individual color bands). Scale in feet. A University Lands well situated in the Wolfcamp formation, Spraberry Trend Field, Midland Basin (Upton County, Texas). **b:** Depth view of imaged seismic events during fracking of each stage (individual color bands). Scale in feet. Wellbore trajectories of fracked well (dark green) and adjacent seismic imaging well (olive green) are highlighted.

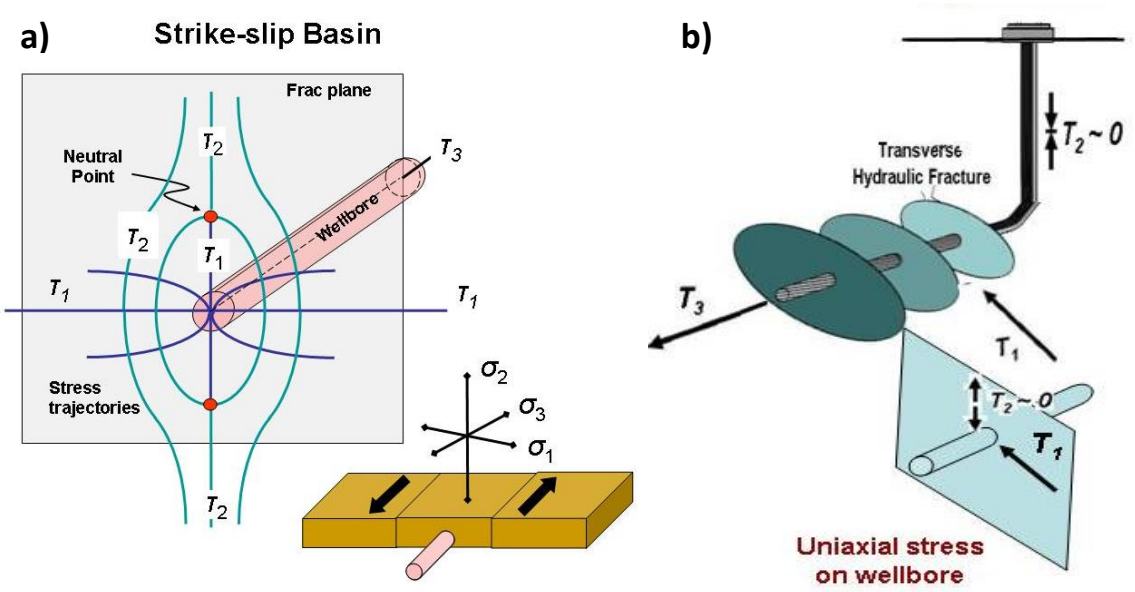

Figure 71 a: Principal (total) stress in left-lateral strike-slip basin with stress trajectory sketch in plane normal to horizontal wellbore aligned with the least principal stress. **b:** Corresponding orientation of transverse fracs, with deviatoric stresses indicated. Reprinted from Thomas and Weijermars (2017; *Submitted to Earth-Science Reviews).

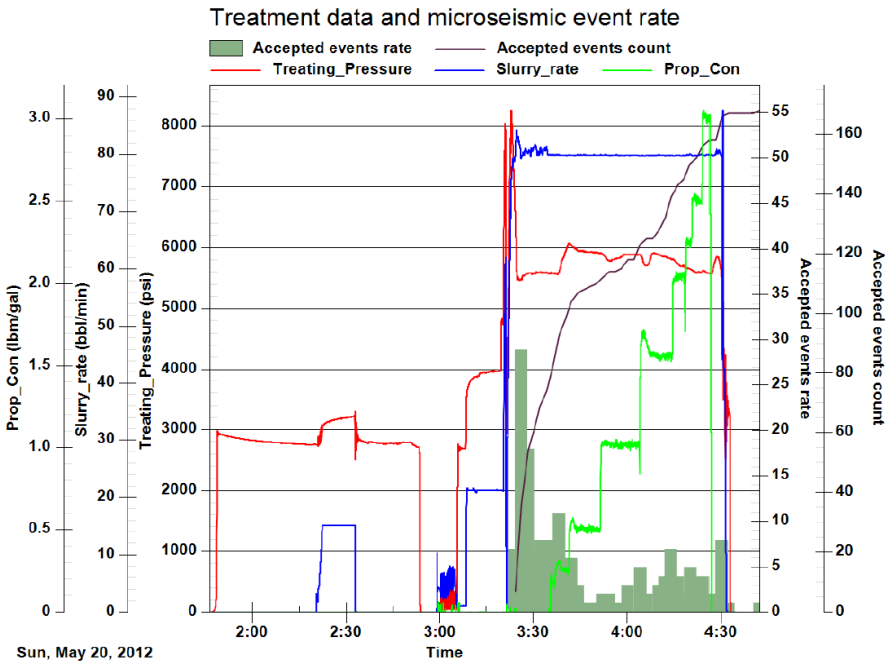

Figure 72: Well stimulation treatment data. Left hand scale shows applied engineering interventions (slurry rate, pumping rate, proppant load, and resulting pressure). Right hand scale shows recorded seismic response with event counts and acceptance rate for seismic events used to generate the images shown in Fig. 70.

With all the far-field stresses accounted for and assuming that in tight rocks P_{NET} = P at the moment of failure, the stress trajectory pattern at the moment of failure follows from (χ, F), which can now be estimated. Because we have τ_1 = -τ_3 = +30 MPa, we have a plane stress state (χ = 1) in the horizontal plane. However, in the vertical plane normal to a horizontal wellbore (Fig. 71b), we have τ_1 = 30 MPa and τ_2 = 0 MPa, which is a uniaxial stress state (χ = 0). We can estimate

$$F = \frac{P_{NET}}{|\tau_1|} = \frac{50\ \text{MPa}}{30\ \text{MPa}} = 1.66$$

The stress trajectory pattern for (χ, F) = (0, 1.66) is given in Fig. 73a. The pertinent magnitudes of the deviatoric principal stresses and the radial and tangential stresses around

the horizontal wellbore are given in Figs. 73(c,d) and 73(e,f), respectively. The radial stress (Fig. 73e) is identical to τ_1 along the far-field τ_1 axis (θ=0º). Moving along the far-field τ_3 axis (θ=90º), the radial stress is equal to τ_1 until the neutral point location, outside of which the radial stress is the least principal stress (Fig. 73d). Conversely, the tangential stress (Fig. 73f) is the intermediate stress along the entire far-field τ_1 axis (θ=0º), but along the far-field τ_3 axis (θ=90º), the tangential stress is the intermediate stress when near the borehole up until the neutral point, beyond which the tangential stress is the maximum principal stress. This stress reversal is key to understanding the near wellbore stress state. Inside the fracture cage region, all radial stress is compressive, even in the direction of the tensile far-filed stress (τ_2). The differential stress of the deviatoric principal stresses ($\tau_1 - \tau_2$) is plotted in Figure 73b. An increased stress concentration is seen in the τ_1 direction, indicating that (tensile) failure is likely in that direction. The neutral points can be observed in Fig. 73d where the magnitude of τ_1-τ_2=0 (shown as a red contour) since neutral points are defined as points where two deviatoric stresses are equal in magnitude. The normalized stress magnitude units in Figs. 73(b-f) can be translated into dimensional stress units by multiplying each non-dimensional unit by τ_1=30 MPa (e.g., if the magnitude of τ_1 is shown at some point to be 3, then in terms of dimensional stress, at that point τ_1=3*30 MPa = 90 MPa).

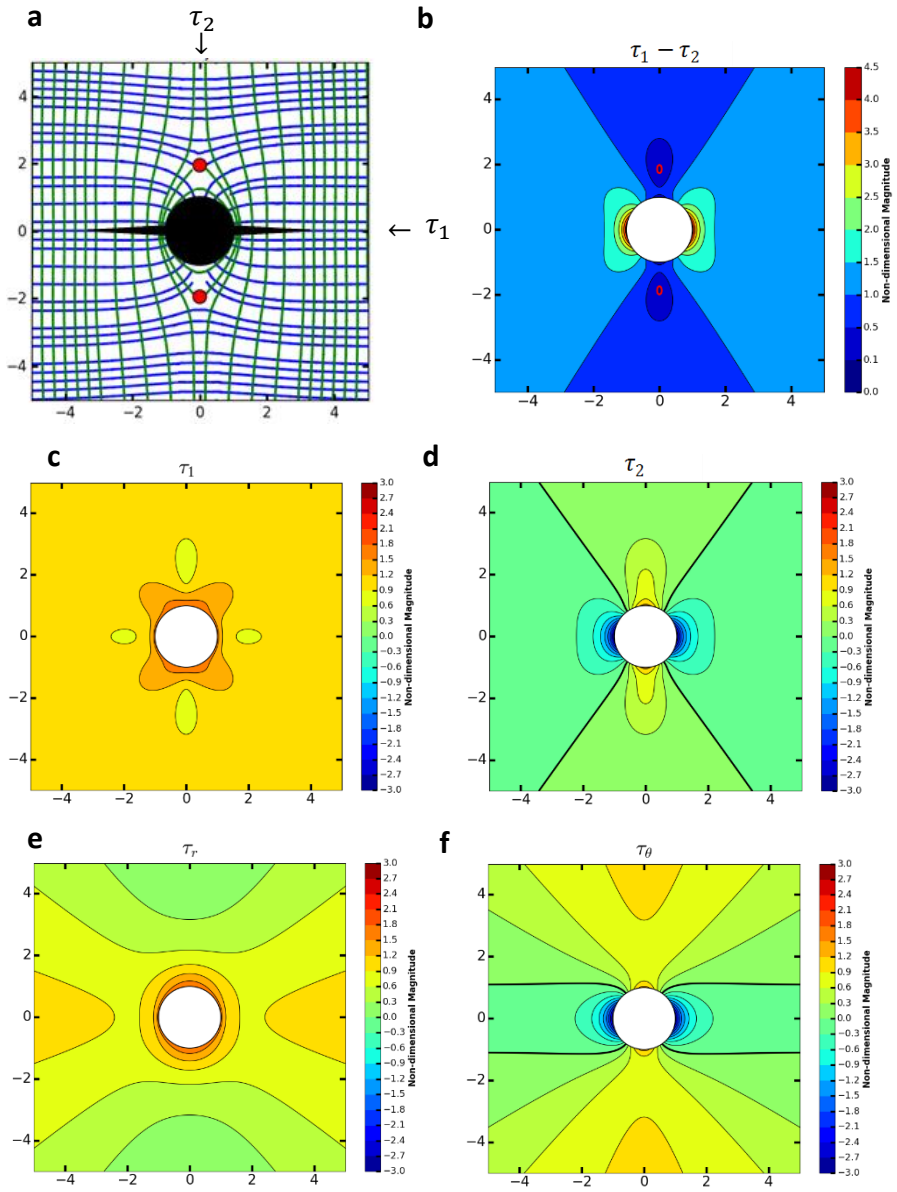

Figure 73: Solutions for a borehole in uniaxial far-field stress (χ=0) and overbalanced net pressure that is 1.66 times the magnitude of the maximum far-field principal stress (F=1.66). Distances are dimensionless, and all stress magnitudes are dimensionless, based on the stress solutions normalized by far-field stress $|\tau_1|$. **a:** Principal stress trajectory patterns Likely fracture propagation based on tensile failure criterion is indicated by black spikes protruding in the τ_1 direction. **b:** $(\tau_1 - \tau_2)$. The neutral point regions (where τ_1=τ_3) marked by red contour lines. **c:** τ_1. **d:** τ_2. The heavier black line indicates where τ_2=0. **e:** Radial stress. **f:** Tangential stress.

11. CONCLUSION

When a borehole is drilled in stressed rock, the stresses are redistributed as the rock formation attempts to push the hole closed. Balancing this redistribution can be complicated. Not only do increased stress concentrations arise at the borehole wall, the stress orientations can also be perturbed. This creates instability hazards while drilling and potential difficulties during stimulation. For hydraulic fracturing, the full stress state around borehole must be understood. Hydraulic fractures always propagate normal to the minimum stress; however, depending on the borehole net fluid pressure and far-field boundary stress conditions, the stress orientations near the wellbore, and their associated magnitudes, can vary significantly. The redirection of the principal stress trajectories is intrinsically coupled with the neutral points, at which the deviatoric principal stress magnitudes are equal. The neutral points form the boundaries for the stress cages in overbalanced boreholes and the complementary fracture cages in underbalanced boreholes. Within the stress cage, the radial stress is the maximum principal stress in all directions. Whereas, in the fracture cage, the tangential stress is the maximum principal stress in all orientations. An effective hydraulic fracture program should account for the complex stress state in the near-wellbore region, including stress orientation reversal. Understanding the neutral point stress reversal leads to more effective completions designs. Additionally, the stress cage and fracture cage must be considered when mitigating tortuosity effects during fracturing.

Even if a wellbore is planned to be drilled overbalanced, local overpressure can render a borehole underbalanced, causing fracture caging effects. Stress trajectories are an

ideal tool to improve our understanding of shear failure. Stress trajectories are related to slip lines, which identify the likely surfaces of shear failure. A comprehensive understanding of the near-wellbore stress state, including the reversal of stress orientations, enables us to better plan/execute a drilling operation because we have more tools at hand to identify optimal wellbore trajectory during planning stages and to continuously determine stress magnitudes and orientations while drilling. The full potential of the analytical Kirsch equations has still not been realized. This thesis provides a groundwork.

REFERENCES

Alberty, M.W., and McClean, M.R., 2004. A physical model for stress cages. SPE 90493.

Aleksandrowksi, P., Inderhaug, O.H., and Knapstad, B., 1992. Tectonic Structures and Wellbore Breakout Orientation. Proc., 33rd U.S. Symposium on Rock Mechanics, Santa Fe, New Mexico, USA (June 3–5, 1992).

Anderson, E.M., 1905. The dynamics of faulting, Trans. Edinburgh Geol. Soc., 8 (3), 387-402.

Anderson, E.M., 1951. The Dynamics of Faulting and Dyke Formation with Applications to Britain. Edinburgh, UK: Oliver and Boyd.

Anderson, E.M., 1936. The dynamics of the formation of cone-sheets, ring dykes and cauldron subsidence. Proc. Roy. Soc. Edin. 56, 128–157.

Andrews, J.S., Fintland, T.G., Helstrup, O.A., Horsrud, P., and Raaen, A.M., 2016. Use of unique database of good quality stress data to investigate theories of fracture initiation, fracture propagation and the stress state in the subsurface. ARMA 16-887.

Atkinson, B.K., and Meredith, P.G., 1987. "Experimental Fracture Mechanics Data for Rocks and Minerals," B.K. Atkinson (ed.): Fracture Mechanics of Rock, London, UK, Academic Press (1987), 477–525.

Barton, C. and Zoback, M., 1994. Stress Pertubations Associated with Active Faults Penetrated by Boreholes: Evidence for Near Complete Stress Drop and a New Technique for Stress Magnitude Measurement. Journal of Geophysical Research (1994) 99, 9373– 9390.

Bach. C., 1898. Elastizität und Festigkeit. Die für die Technik wichtigsten Sätze und deren erfahrungsmäßige Grundlage. Berlin, Springer.

Bay, D., 2017. "Big Bang Bullet Holes." *LensCulture*. N.p., n.d. Web. 25 July 2017. <https://www.lensculture.com/articles/deborah-bay-big-bang-bullet-holes>.

Bell, J.S., and Gough D.I., 1979. Northeast-southwest compressive stress in Alberta: Evidence from oil wells. Earth Planet. Sci. Lett., 45, 475-482.

Biot, M. A., 1941. General theory of three-dimensional consolidation, J. Appl. Phys., 12, 155-64.

Blumentritt, C. H., Sullivan, E. C., Marfurt, K. J., & Murphy, M. (2003, January 1). 3-D Seismic Attribute Illumination of Paleozoic Tectonics, Central Basin Platform, West Texas. Society of Exploration Geophysicists.

Blumentritt, C. H., Marfurt, K.J., Sullivan, E.C., 2006. Volume-based curvature computations illuminate fracture orientations — Early to mid-Paleozoic, Central Basin Platform, west Texas. Geophysics 71(5), B159–B166. DOI 10.1190/1.2335581.

Bolden, G.P., 1984, Wrench Faulting in Selected Areas of the Permian Basin, in Moore, G. and Wilde, G., eds., Transactions of the Southwest Section of the AAPG, Southwest Section Publication 84-78, 131-140.

Boley, B.A., and Weiner, J.H., 1960. Theory of Thermal Stresses, John Wiley & Sons. New York.

Box, G.E.P., 1976. Science and Statistics. (PDF), Journal of the American Statistical Association, 71: 791–799, doi:10.1080/01621459.1976.10480949.

Brace, W.F., and Kohlstedt, D.L.,1980. Limits on lithospheric stress imposed by laboratory experiments: J. Geophys. Res. 85: 6248-6252.

Bradley, W.B., 1979. “Failure of Inclined Boreholes,” Journal of Energy Research Technology (December 1979) 101, 232–239.

Bratton, T., Bornemann, T., Li, Q., Plumb, R., and Rasmus, J., 1999. Logging-While-Drilling Images for Geomechanical, Geological and Petrophysical Interpretations. Transactions of the SPWLA 40th Annual Logging Symposium, Olso, Norway (June 8–10, 1999).

Byerlee, J.D., 1978. Friction of rocks: Pure and Applied Geophysics 116: 615-626.

Carruthers, T. D., 2012, Interaction of polygonal fault systems with salt diapirs: PhD Thesis, University of Cardiff, Cardiff, United Kingdom, 479p.

Cesaro, M., Cheung, P., Etchecopar, A. and Gonfalini, M., 1997. Shaping Up to Stress in the Appenines. Italy 2000: Value Added Reservoir Characterization (Well Evaluation Conference, Italy), Schlumberger.

Cheng, A. H-D., Abousleiman, Y., and Roegiers, J.-C., 1993, "Review of Some Poroelastic Effects in Rock Mechanics," Int. J. Rock Mech. Min. Sci. & Geomech. Abstr., Vol. 30, pp. 1119-1126.

Cleary, M. P., Johnson, D. E., Kogsbøll, H.-H., Owens, K. A., Perry, K. F., de Pater, C. J., … Mauro, T. (1993, January 1). Field Implementation of Proppant Slugs To Avoid Premature Screen-Out of Hydraulic Fractures With Adequate Proppant Concentration. Society of Petroleum Engineers. doi:10.2118/25892-MS

Coussy, O., 2004. Poromechanics, Wiley, Chichester.

Couzens-Schultz, B. A., Axon, A., Azbel, K., Hansen, K. S., Haugland, M., Sarker, R., … Zhang, Z. (2013, March 26). Pore Pressure Prediction in Unconventional Resources. International Petroleum Technology Conference. doi:10.2523/IPTC-16849-MS.

De Boer, R., 2000. Theory of Porous Media, Springer, Berlin.

Delale, F., 1984. Stress analysis of multilayered plates around circular holes. Int. J. Eng. Sci. vol. 22 (1), p. 57-75.

Denney, D., (2012, June 1). Phosphonic/Hydrofluoric Acid: Tortuosity Remediation for Fracturing Treatments. Society of Petroleum Engineers. doi:10.2118/0612-0100-JPT

Detournay, E., 1983. Two-dimensional elastoplastic analysis of a deep cylindrical tunnel under non-hydrostatic loading, Ph.D. dissertation, Univ. of Minn., Minneapolis.

Detournay, E., and Carbonell, R., 1994. Fracture Mechanics Analysis of the Breakdown Process in Minifrac or Leak-Off Tests. paper SPE 28076, presented at the SPE/ISRM Rock Mechanics in Petroleum Engineering Conference, Delft, Netherlands (August 29–31, 1994).

Detournay, E. and Cheng, A.-D, 1988. Poroelastic response of a borehole in a non-hydrostatic stress field, Int. J. Rock Mech., 25, 171-82.

Detournay, E. and Cheng, A.-D, 1993. Fundamentals of poroelasticity, in Comprehensive Rock Engineering, J. A. Hudson, ed., Pergamon, Oxford, pp. 113-71.

Detournay, E., and Fairhurst, C., 1982. Generalization of the ground reaction curve concept, paper presented at 23rd U.S. Symposium on Rock Mechanics, Am. Inst. of Min. and Eng., Berkeley, Calif.

Detournay, E., Cheng, A.-D, Roegiers, J. C., and McLennan, J. D., 1989. Poroelasticity considerations in in situ stress determination by hydraulic fracturing, Int. J. Rock Mech., 26, 507-13.

Devine, P. E. (2014, August 25). Toward Understanding Overpressure in a Basin with Burial and Uplift: Preliminary Results of a Study Measuring Undercompaction with DT Logs. Unconventional Resources Technology Conference. doi:10.15530/URTEC-2014-1922841

Donald, A., Wielemaker, E., Karpfinger, F., Gomez, F., Liang, X., and Tingay, M., 2015. Qualifying Stress Direction from Borehole, Shear Sonic Anisotropy, Proceeding 49th ARMA Conference, June, 15-364, 1-10.

Dupriest, F.E., Elks, W.C., Ottesen, S., Pastusek, P.E., Zook, J.R., and Aphale, C. (2010, January 1). Borehole Quality Design and Practices to Maximize Drill Rate Performance. Society of Petroleum Engineers. doi:10.2118/134580-MS

Economides M.J., Nolte, K.G., Ahmed, U., Schlumberger, D., 2000. Reservoir Stimulation, Vol. 18, Wiley.

Endo, T., Brie, A., and Badri, M., 1996. Fracture Evaluation from Dipole Shear Anisotropy and Borehole Stoneley Waves. Transactions of the SPWLA 2nd Annual Logging Symposium of Japan (1996), paper U.

Engelder, T., 1993. Stress Regimes in the Lithosphere. Princeton, New Jersey, USA, Princeton University Press.

Exadaktylos, G.E., Lilies, P.A., Stavropoulou, M.C., 2003. A semi-analytical elastic stressdisplacement solution for notched circular openings in rocks, Inter. J. of solids and structures 40. 1165-1167.

Fahrenthold, E.P., and Cheatham, J.B., 1986. An approximate rock stress-field for steady flow into production casing, J. Energy Resour. Tech., 108, 116-9.

Fairhurst, C., 2013. Fractures and Fracturing - Hydraulic fracturing in Jointed Rock, Effective and Sustainable Hydraulic Fracturing, Dr. Rob Jeffrey (Ed.), InTech, DOI: 10.5772/56366. Available from: https://www.intechopen.com/books/effective-and-sustainable-hydraulic-fracturing/fractures-and-fracturing-hydraulic-fracturing-in-jointed-rock

Fjær, E., Holt, R.M., Horsrud, P., Raaen, A.M., Risnes, R., 2008, Petroleum Related Rock Mechanics (2nd Edition). Developments in Petroleum Science, vol. 53, p. 1-491.

Föppl, A., 1897. Festigkeitslehre. Leipzig.

Frigg, R., and Hartmann, S., 2009. "Models in Science", *The Stanford Encyclopedia of Philosophy*, Edward N. Zalta ed.

Gambolati, G., Teatini, P., and Ferronato, M., 2006. Anthropogenic Land Subsidence, Encyclopedia of Hydrological Sciences, Wiley, Chichester, UK, DOI 10.1002/0470848944.hsa164b.

Gaswirth, S.B., Marra, K.R., Lillis, P.G., Mercier, T.J., Leathers-Miller, H.M., Schenk, C.J., Klett, T.R., Le, P.A., Tennyson, M.E., Hawkins, S.J., Brownfield, M.E., Pitman, J.K., and Finn, T.M., 2016, Assessment of undiscovered continuous oil resources in the Wolfcamp shale of the Midland Basin, Permian Basin Province, Texas, 2016: U.S. Geological Survey Fact Sheet 2016–3092, 4 p., https://doi.org/10.3133/fs20163092.

Gnirk, P.F., 1972. "The Mechanical Behavior of Uncased Wellbores Situated in Elastic/Plastic Media Under Hydrostatic Stress," paper SPE 3224, SPE Journal (February 1972) 12, No. 1, 49–59.

Gough, D.I., and Bell, J.S., 1981. Stress orientations from oil-well fractures in Alberta and Texas. Can. J. Earth Sci. 18, 638 – 645.

Gough, D.I., and Bell, J.S., 1982. Stress orientations from borehole wall fractures with examples from Colorado, east Texas, and nothern Canada. Can. J. Earth Sci. 19, 1358–1370.

Gross, D., and Seelig, T., 2006. Fracture Mechanics. Springer-Verlag, Berlin.

Gudmundsson, A., 2006. How local stresses control magma-chamber ruptures, dyke injections, and eruptions in composite volcanoes. Earth Sci. Rev. 79, 1–31.

Guenot, A., 1989. "Instability Problems at Great Depth Drilling Boreholes and Wells," Proc., Rock at Great Depth, International Symposium of Rock Mechanics, Pau, France (1989), 1199–1208.

Guisiat, F.D., and Haimson, B.C., 1992. Scale effects in rock mass stress measurements. Int. J. Rock Mech. Min. Sci. Geomech. Abstr. 29 (2), 99–117.

Guo, F., Morgenstern, N.R., and Scott, J.D., 1993. Interpretation of Hydraulic Fracturing Breakdown Pressure. International Journal of Rock Mechanics and Mining Sciences & Geomechanics Abstracts (1993) 30, No. 6, 617–626.

Haimson, B.C., 2007. Micromechanisms of borehole instability leading to breakouts in rocks, Int. J. Rock. Mech. Min. Sci., Vol. 44, pp. 157-17.

Haimson, B.C., and Herrick, C.G., 1985. In situ stress evaluation from borehole breakouts—experimental studies. Research and Engineering Applications in Rock Mechanics. Proc. 26th U.S. Symposium on Rock Mech. Rapid City. Balkema, Rotterdam, pp. 1207 – 1218.

Haimson, B.C., and Fairhurst, C., 1967. Initiation and extension of hydraulic fractures in rock, Soc. Petr. Eng. J. 7: 310-318.

Haimson, B.C. and Huang, X., 1989. Hydraulic Fracturing Breakdown Pressure and In-Situ Stress at Great Depth. Rock at Great Depth, V. Fourmaintraux and D. Maury (eds.), Rotterdam, Netherlands, Balkema (1989), 939–946.

Haimson, B.C., and Kovachich, J., 2003. Borehole instability in high-porosity Berea sandstone and factors affecting dimensions and shape of fracture-like breakouts. Eng Geol 69:219–231

Haimson, B.C., and Song, I., 1993. Laboratory study of borehole breakouts in Cordova Cream: a case of shear failure. Int. J. Rock Mech. Min. Sci. Geomech. Abstr. 30, 1047 – 1056.

Haimson, B.C., Song, I., and Kovacich, J.R., 1999. Borehole breakouts in poorly consolidated sandstones. EOS-Trans. Am. Geophys. Union 80, S335.

Handin, J., 1966. *Strength and ductility,* in Handbook of Physical Constants (ed. S. P. Clark) (The Geol. Soc. of America, New York 1966), 223 290.

Herrick, C.G., and Haimson, B.C., 1994. Modeling of episodic failure leading to borehole breakouts in Alabama limestone. Rock Mechanics and Measurements. Balkema, Rotterdam, pp. 217 – 224.

Hoak, T., Sundberg, K., Ortoleva, P., 1998. Overview of the structural geology and tectonics of the Central Basin Platform, Delaware Basin, and Midland Basin, West Texas and New Mexico. DOE/PC/91008--23-Pt.8. https://www.osti.gov/scitech/biblio/307858

Hoek E., Brown E., 1980. Underground excavations in rock. The Institution of Mining and Metallurgy, London.

Hornung, M.R., 1990. Kick Prevention, Detection, and Control: Planning and Training Guidelines for Drilling Deep High-Pressure Gas Wells. SPE/IADC Drilling Conference, 27 February-2 March 1990, Houston, Texas. SPE-19990-MS.

Hottman, C.E., Smith, J.H., Purcell, W.R., 1979. Relationship among earth stresses, pore pressure and drilling problems offshore Gulf of Alaska. J. Petrol. Technol. 31, 1477–1484.

Hubbert, M.K., and Willis, D.G., 1957. Mechanics of Hydraulic Fracturing. paper 686-G, presented at the SPE Annual Meeting, Los Angeles, California, USA (October 14–17, 1956); also in Journal of Petroleum Technology (September 1957) 9, No. 6, 153–168 and Trans., AIME (1957) 210.

Ito, T., and Hayashi, K., 1991. Physical Background to the Breakdown Pressure in Hydraulic Fracturing Tectonic Stress Measurements. International Journal of Rock Mechanics and Mining Sciences & Geomechanics Abstracts (1991) 28, No. 4, 285–293.

Jaeger, J.C., and Cook, N.G.W., 1979. Fundamentals of Rock Mechanics (3rd ed.). Chapman and Hall, London. 593 pp.

Jaeger, J., Cook, N.G.W., Zimmerman, R., 2007. Fundamentals of Rock Mechanics. Chapman and Hall, London.

Jeffrey, R.G., and Zhang, X., 2010. Mechanics of hydraulic fracture growth from a borehole, SPE 137393, in *Proceedings of the Canadian UnconventionalResources and International Petroleum Conference,* Calgary, Alberta, Canada, 2010 October 19–21.

Kaeng, G. C., Sausan, S., & Satria, A. (2014, December 10). Geopressure Centroid as Pore Pressure Prediction Challenge in Deepwater South East Asia. International Petroleum Technology Conference. doi:10.2523/IPTC-18239-MS

Kaeng, G. C., Sausan, S., Natadafani, B. A., & Natepracha, J. (2015, January 1). Overpressure in Deepwater Thrust-Fold Belt of Sundaland Continental Margin, South East Asia. Society of Petrophysicists and Well-Log Analysts.

Keller, G.R., Hills, J.M., and Djeddi, R., 1980. A regional geological and geophysical study of the Delaware Basin, New Mexico and West Texas. New Mexico Geological Society Guidebook, 31st Field Conference, Trans-Pecos Region, 1980, p. 105-111.

Koenig, E., and D.D. Pollard, 1998. Mapping and modeling of radial fracture patterns. J. Geophys. Res., 103, 15, 183 – 15, 202.

Kogsbøll, H.H., Pitts, M. J., and Owens, K.A., (1993, January 1). Effects of Tortuosity in Fracture Stimulation of Horizontal Wells - A Case Study of the Dan Field. Society of Petroleum Engineers. doi:10.2118/26796-MS.

Kowalski, J., 1975. Formation Strength Parameter from Well Logs. Transactions of the SPWLA 16th Annual Logging Symposium (June 4–7, 1975), paper N.

Last, N., Plumb, R., Harkness, R., Charlez, P., Alsen, J., and McLean, M., 1995. An Integrated Approach to Evaluating and Managing Wellbore Instability in the Cusiana Field, Colombia, South America. paper SPE 30464, presented at the SPE Annual Technical Conference and Exhibition, Dallas, Texas, USA (October 22–25, 1995).

Lee, M.Y., and Haimson, B.C., 1993. Laboratory study of borehole breakouts in Lac du Bonnet granite: a case of extensile failure mechanism. Int. J. Rock Mech. Min. Sci. Geomech. Abstr. 30, 1839 – 1845.

Li, S., George, J., and Pudy, C., 2012. Pore-pressure and wellbore stability prediction to increase drilling efficiency. JPT, vol. 63, no. 2, p. 98-101 (SPE 144717).

Kirsch, G., 1898. Die Theorie der Elastizität und die Bedürfnisse der Festigkeitslehre. Z. Ver. dtsch. Ing. 42: p. 797-807.

Ma, X., and Zoback, M.D., (2016, June 26). Laboratory Investigation on Effective Stress in Middle Bakken: Implications on Poroelastic Stress Changes due to Depletion and Injection. American Rock Mechanics Association.

Malvern, L.E., 1969. Introduction to the Mechanics of a Continuous Medium, Prentice-Hall.

Maury, V., 1994. Rock Failure Mechanisms Identification: A Key for Wellbore Stability and Reservoir Behaviour Problems. Proc., Eurock ’94, Rock Mechanics in Petroleum Engineering, Delft, Netherlands (1994), 175–182.

Moore, D. E., Summers, R., & Byerlee, J. D. (1983, January 1). Strengths Of Clay And Non-Clay Fault Gouges At Elevated Temperatures And Pressures. American Rock Mechanics Association.

Moos, D., 2006. "PEH: Geomechanics Applied to Drilling Engineering." Ed. Robert F. Mitchell. *Drilling Engineering*. Ed. Larry W. Lake. Vol. 2. N.p.: Society of Petroleum Engineers, n.d. 1-87. Print.

Moos, D., Peška, P., Finkbeiner, T., and Zoback, M., 2003. Comprehensive wellbore stability analysis utilizing quantitative risk assessment: Journal Petroleum Science and Engineering, v. 38, p. 97-109.

Muller, O., 1986. Changing stress during the emplacement of the radial dikes at Spanish Peaks, Colorado. Geology 14: 157-159.

Muller, O.H., and Pollard, D.D., 1977. Stress state near Spanish Peaks, Pure Appl. Geophys., 115, 69 – 86.

Muskhelishvili, N.I., 1954. Some Basic Problems of the Mathematical Theory of Elasticity, Noordhof Ltd., Groningen, The Netherlands.

Norris, A., 1992. On the correspondence between poroelasticity and thermoelasticity, J. Appl. Phys., 71, 1138-41.

Ong, S.H. and Roegiers, J.-C., 1993. “Influence of Anisotropies in Borehole Stability,” International Journal of Rock Mechanics and Mining Sciences & Geomechanics Abstracts (June 1993) 30, No. 7, 1069–1075.

Oyarhossein, M., & Dusseault, M. B. (2015, November 13). Wellbore Stress Changes and Microannulus Development Because of Cement Shrinkage. American Rock Mechanics Association.

Perras, M.A., and Diederichs, M.S., 2014. A review of the tensile strength of rock: concepts and testing. Geotech Geol Eng., 32, 525–546.

Peška, P., and Zoback, M.D., 1995. Compressive and tensile failure of inclined well bores and determination of in situ stress and rock strength. J. Geophys. Res. V. 100, (B7), p. 12,891-12,811.

Pistre, V., Yan, G.R., Sinha, B., Prioul, R., and Vidal-Gilbert, S., 2009. Determining Stress Regime and Q Factor from Sonic Data. Society of Petrophysicists and Well-Log Analysts.

Plumb, R.A., 1994. Influence of Composition and Texture on the Failure Properties of Clastic Rocks. SPE 28022, presented at the SPE/ISRM Rock Mechanics in Petroleum Engineering Conference, Delft, Netherlands (August 29–31, 1994).

Plumb, R.A., and Cox, J.W., 1987. Stress Directions in Eastern North American Determined to 4.5 Km from Borehole Elongation Measurements. Journal of Geophysical Research (1987) 92, No. B6, 4805– 4816.

Rice, J.R., and Cleary, M.P., 1976. Some basic stress diffusion solutions for fluid saturated elastic porous media with compressible constituents, Rev. Geophys. Space Phys., 14, 227-41.

Roest, J.P.A., Kamp, W., Zhongjie, H., and Cockram, M.J., 1989. Basic research for the de-stressing of the rock ring surrounding a gallery under severe stress, in *Proceeding of the International Society for Rock MechanicsInternational Symposium,* 1989 August 30–September 2, A.A. Balkema, Dordrecht, Pau, France.

Rudnicki, J.W., 2001. Linear poroelasticity, Handbook of Material Behavior Models, (J. Lemaitre, editor), Academic Press, 1118-1125.

Rudnicki, J.W., and Hsu, T.-C., 1988. Pore pressure changes included by slip on permeable and impermeable faults, J. Geophys. Res., 93, 3275-85.

Rutqvist, J., Tsang, C.-F., and Stephansson, O., 2000. Uncertainty in the maximum principal stress estimated from hydraulic fracturing measurements due to the presence of the induced fracture. Int. J. Rock Mech. and Mining Sci., 37, 107-120.

Santarelli, F.J., Dahen, D., Baroudi, H., and Sliman, K.B., 1992. “Mechanisms of Borehole Instability in Heavily Fractured Rock Media,” International Journal of Rock Mechanics and Mining Sciences & Geomechanics Abstracts (October 1992) 29, No. 5, 457–467.

Savin, G.N., 1961. Stress concentrations around holes. Pergamon Press, New York, 430 pp.

Sayers, C. M., den Boer, L. D., Nagy, Z. R., Hooyman, P. J., & Ward, V. (2005, January 1). Regional Trends In Undercompaction And Overpressure In the Gulf of Mexico. Society of Exploration Geophysicists.

Schutjens, P.M.T.M., Snippe, J.R., Mahani, H., Turner, J., Ita, J., and Mossop, A.P., March 1, 2012. Production-Induced Stress Change in and Above a Reservoir Pierced by Two Salt Domes: A Geomechanical Model and Its Applications. Society of Petroleum Engineers. doi:10.2118/131590-PASeymour, K.P., Rae, G., Peden, J.M., Ormston, K., 1993. Drilling close to salt diapirs in the North Sea. In: Offshore Europe, 09/07/1993, Aberdeen, U.K.

Senseny, T.W., and Pfiefle, T.W., 1984. “Fracture Toughness of Sandstones and Shales,” Proc., 25th U.S. Symposium on Rock Mechanics (1984), 390–397.

Skempton, A. W., 1954, "The Pore Pressure Coefficients A and B," Geotechnique, Vol. 4, pp. 143-147.

Stewart, S.A., 2006. Implications of passive salt diapir kinematics for reservoir segmentation by radial and concentric faults. Marine and Petroleum Geology 23(8), 843-853.

Tai, P.C. and Dorobek, S.L., 2000. Tectonic Model for Late Paleozoic Deformation of the Central Basin Platform, Permian Basin Region, West Texas. The Permian Basin: Proving Ground for Tomorrow's Technologies, W. D. DeMis, M. K. Nelis, and R. C. Trentham, eds. West Texas Geological Society, October 19-20, 2000, Publ. #00-109, p. 157-176.

Teklu, T.W., Akinboyewa, J., Alameri, W., Kazemi, H., Graves, R.M., and AlSumaiti, A.M., (2014, August 18). Stress Change Investigation During Polymer-Augmented Waterflooding in Channeled Reservoirs. American Rock Mechanics Association.

Terzaghi, K., 1923. Die Berechnung der Durchl¨assigkeitsziffer des Tones aus dem Verlauf der hydrodynamische Spannungserscheinungen, Sitzber. Akad. Wiss. Wien, Abt. IIa, 132, 125-138.

Terzaghi, K., 1925. Erdbaumechanik auf bodenphysikalischer Grundlage, Deuticke, Wien.

Thiercelin, M., and Plumb, R.A., 1991. A Core-Based Prediction of Lithologic Stress Contrasts in East Texas Formations. paper SPE 21847, presented at the SPE Rocky Mountain Regional Meeting/Low Permeability Reservoirs Symposium, Denver, Colorado, USA (April 15–17, 1991); also in SPE Formation Evaluation (December 1994) 4, No. 4, 251–258.

Timoshenko, S.P., and Goodier, J.N., 1970. Theory of Elasticity (3rd ed.). McGraw-Hill, New York, 567 pp.

Tovar, J., and Bhat, S., 2011. Characterization of stress caging effect for resolving wellbore integrity problems in fractured formations—experimental results, VII INGEPET 2011 (EXPL-2-JT-02).

Vardoukalis, I., Sulem, J., and Guenot, A., 1988. Borehole instabilities as bifurcation phenomena, *Int. J. Rock Mech. Min. Sci. Geomech., Abstr.*,25(3), 159–170.

Verruijt, A., 1969. Elastic storage in aquifers, in Flow Through Porous Media, R. J. M. De Wiest, ed., Academic Press, New York, pp. 331-76.

Von Goten, W.D., and Choudhary, B.K., (1969, January 1). The Effect of Pressure and Temperature on Pore Volume Compressibility. Society of Petroleum Engineers. doi:10.2118/2526-MS

Wang, H.F., 2000. Theory of Linear Poroelasticity, Princeton University Press, Princeton.

Wang, M.H., Soliman, M.Y., and Towler, B.F., 2008. Investigation of Factors for Strengthening a Welllbore by Propping. 2008 IADC/SPE Drilling Conference, Orlando, Florida, USA, 2008 March 4–6. IADC/SPE112629.

Wang, X., Chalaturnyk, R., Huang, H., and Leung, J., (2015, June 9). Experimental Study on Geomechanical Dilation during Injection. Society of Petroleum Engineers. doi:10.2118/174453-MS

Warpinski, N.R., 1994. Interpretation of Hydraulic Fracture Mapping Experiments. paper SPE 27985, presented at the University of Tulsa Centennial Petroleum Engineering Symposium, Tulsa, Oklahoma, USA (August 29–31, 1994).

Weijermars, R., 1998. Principles of Rock Mechanics. Alboran Science Publishing. 360 http://ocw.tudelft.nl/courses/applied-earth-sciences/principles-of-rock-mechanics/course-home/

Weijermars, R., 2011. Analytical Stress Functions applied to Hydraulic Fracturing: Scaling the Interaction of Tectonic Stress and Unbalanced Borehole Pressures. American

Rock Mechanics Association paper ARMA 11-598, Proceedings of the 45th US Rock Mechanics/Geomechanics Symposium held in San Francisco, CA, June 26–29, 2011.

Weijermars, R., 2013, Mapping stress trajectories and the width of stress perturbation-zones near a cylindrical wellbore. International Journal of Rock Mechanics and Mining Sciences, vol. 64, p. 148–159.

Weijermars, R., 2016. Stress Cages and Fracture Cages in Stress Trajectory Models of Wellbores: Implications for Pressure Management during Drilling and Hydraulic Fracturing. Journal of Natural Gas Science and Engineering (JNGSE), vol. 3, p. 986-1003.

Weijermars, R., and Poliakov, A., 1993. Stream functions and complex potentials: Implications for the development of rock fabric and continuum assumption. Tectonophysics 220: 33-50.

Weijermars, R., and Schmeling, H., 1986, Scaling of Newtonian and non-Newtonian fluid dynamics without inertia for quantitative modelling of rock flow due to gravity (including the concept of rheological similarity), *Phys. of the Earth and Planet. Int.*, *43*, 316–330.

Weijermars, R., and Schultz-Ela, D., 2012. Visualizing stress trajectories around pressurized wellbores. SPE Paper 152559. SPE/ EAGE European Unconventional Resources Conference and Exhibition, held in Vienna, Austria, 20-22, March 2012, p.1-10.

Weijermars, R., Jackson, M.P.A., and Vendeville, B., 1993. Rheological and tectonic modelling of salt provinces. Tectonophysics 217: 143-174.

Weijermars, R., Zhang, X. and Schultz-Ela, D., 2012. Unrecognized 'fracture caging' could make shale gas drilling safer and more profitable. First Break, Vol. 30, No. 1 (February Issue), p. 35-36.

Weijermars, R., Zhang, X, and Schultz-Ela, D., 2013a. Geomechanics of Fracture Caging in Wellbores. Geophysical Journal International (GJIRAS), vol. 193, issue 3, p. 1119-1132.

Weijermars, R., Jackson, M.P.A., and Van Harmelen, A., 2013b. Closure of open wellbores in creeping salt sheets, Geophysical Journal International (GJIRAS),vol. 196, issue 1, p. 279 -290

Weijermars, R., Jackson, M.P.A., and Dooley, T. P., 2014. Quantifying drag on wellbore casings in moving salt sheets, Geophysical Journal International (GJIRAS), vol. 198, issue 2, p. 965-977.

Whitehead, W.S., Hunt, E.R., and Holditch, S.A., 1987. The Effects of Lithology and Reservoir Pressure on the In-Situ Stresses in the Waskom (Travis Peak) Field. paper SPE 16403, presented at the SPE/DOE Low Permeability Reservoirs Symposium, Denver, Colorado, USA (May 18–19, 1987).

Winsberg, E., 2001. "Simulations, Models and Theories: Complex Physical Systems and their Representations". In: *Philosophy of Science* 68 (Proceedings): 442-454.

Wiprut, D.J. and Zoback, M.D., 1998. High Horizontal Stress in the Visund Field, Norwegian North Sea: Consequences for Borehole Stability and Sand Production. paper SPE 47244, presented at the SPE/ISRM Eurock '98, Trondheim, Norway (July 8–10, 1998).

Zang, A., and Stephansson, O., 2010. Stress field of the Earth's crust, Springer, London.

Zhang, C.-L., (2015, January 1). Deformation of Clay Rock under THM Conditions. International Society for Rock Mechanics.

Zhang L. and Zhu H., 2007. Three-dimensional Hoek–Brown strength criterion for rocks. J Geotech Geoenvir Eng. ASCE 2007; 133 (9):1128–35.

Zhang, X., Jeffrey, R.G., and Thiercelin, M., 2009. Mechanics of fluid-driven fracture growth in naturally fractured reservoirs with simple network geometries, *J. geophys. Res.-Solid Earth*, 114, B12406.

Zhang, X., Jeffrey, R.G., and Bunger, A.P., 2011a. Hydraulic fracture growth from a non-circular wellbore. American Rock Mechanics Association, ARMA 11–333, in *Proceedings of the 45th US Rock Mechanics/Geomechanics Symposium,* San Francisco, CA, 2011 June 26–29.

Zhang, X., Jeffrey, R.G., Bunger, A.P., and Thiercelin, M., 2011b. Initiation and growth of a hydraulic fracture from a circular wellbore, *Int. J. RockMech. Min. Sci.*, 48, 984–995.

Zheng, Z., Cook, N.G.W., Myer, L.R., 1988. Borehole breakout and stress measurements. In: Proceedings of the 29th US Symposium on Rock Mechanics. A.A. Balkema, Rotterdam, pp. 471–478.

Zheng, Z., Kemeny, J., Cook, N.G.W., 1989. Analysis of borehole breakouts. J. Geophys. Res. 94, 7171 – 7182.

Zhou, S., 1997. A method of estimating horizontal principal stress magnitudes from stress-induced wellbore breakout and leak-off tests and ts application to petroleum engineering. Petroleum Geoscience, 3, 57-64.

Zimmerman, R.W., 2000. Coupling in poroelasticity and thermoelasticity, Int. J. Rock Mech., 37, 79-87.

Zoback, M.D., 2007. Reservoir Geomechanics. 1st ed., Cambridge: Cambridge University Press. 449.

Zoback, M.D., Moos, D., Mastin, L., Anderson, R.N., 1985. Well bore breakouts and in situ stress. J. Geophys. Res. 90, 5523 – 5538.

Zoback, M.D., Barton, C.A., Brudy, M., Castillo, D.A., Finkbeiner, T., Grollimund, B.R., Moos, D.B., Peška, P., Ward, C.D., and Wiprut, D.J., 2003. Determination of stress orientation and magnitude in deep wells. Int. J. Rock Mech. and Mining Sci., 40, 1049-1076.

APPENDIX A – THE GEOMECHANICAL MODEL

A) Overburden

The overburden can be quantified from an offset density log or approximated by regional correlations. Although it is not measured directly, it can be easily computed as the integral over depth of the bulk density:

$$\sigma_v = \int_0^z \rho_b dz \tag{A1}$$

However, ρ_b (bulk density) is rarely measured up to the surface more than once in the lifetime of a field (i.e., for seismic profiling). Research may be necessary to obtain an estimate of ρ_b between the top of the log and the surface. Furthermore, for deepwater projects, the significant effect of the water column on σ_v must be included.

To get the effective stresses, the variation of pore pressure with depth is needed, which can be estimated from the sonic porosity (Donald et al., 2015), the resistivity data, or even seismic data. The vertical principal stress, σ_v, is computed by integrating the density log (Eq. A1) and the effective vertical stress, σ_v', is then obtained by subtracting out the pore pressure.

B) Stress orientation

The principal stress orientations can be determined by a number of methods. The most common methods for determining stress orientations are described below:

- Wellbore breakouts

The presence of a wellbore in the formation generates a local change in the stresses (Economides, 2010). When the pressure in the wellbore falls below the fluid pressure in the surrounding rock, the formation may fail in compression or shear, and wellbore breakouts can form (Zoback et al., 1985; Plumb and Cox, 1987). The breakout is symmetrical and bi-wing. In a vertical well, interpretation of the breakout is straightforward because the azimuth of the breakout corresponds to the azimuth of σ_h, if σ_h is a principal stress direction. In deviated or horizontal wells, the location of breakouts is a function of the ratio of stresses $(\sigma_2 - \sigma_3)/(\sigma_1 - \sigma_3)$ and the orientation of the wellbore with respect to the stresses. Processing is required (Cesaro et al., 1997), and in some cases, it can identify both the orientation of the stresses and the ratio between them. The most basic way breakouts are detected is by examining the log track recorded by a four-arm caliper (Plumb and Hickman, 1985). Significant focus should be allotted to not misidentify features, such as key seating and overreaming, as breakouts. Numerous studies have been performed regarding the identification of breakouts (Zoback et al., 1985; Bratton et al., 1999; Maury et al., 1999). Simple interpretation assumptions are used to infer stress magnitudes from breakouts (Cesaro et al., 1997). However, currently no technique reliably infers the stress magnitudes from the presence of breakouts alone.

- Drilling-induced fractures

Because of the stress concentration resulting from the presence of the wellbore, tensile stresses may be generated at the borehole wall when the pressure in the wellbore rises above a certain level. If the tensile strength of the rock is reached, drilling-induced

fractures will be created. These easily identifiable fractures occur perpendicular to the least principal stress, 180° apart.

Drilling-induced fractures are shallow and conductive, which makes them obvious on electrical imaging logs, such as that recorded by the Fullbore Formation Micro-Imager (FFM). In a vertical well, drilling-induced subvertical fractures occur in the direction of the maximum horizontal stress. In deviated and horizontal wells, en echelon fractures (discontinuous fractures) are observed. An analysis similar to that conducted for breakouts can yield stress ratios and stress directions (Wiprut and Zoback, 1998). A final check on stress orientation should also verify that any breakouts occur 90° from drilling-induced fractures.

- Hydraulic fracture diagnostics

Microseismicity or tiltmeters (e.g., Warpinski, 1994) can establish an estimate of the azimuth of a hydraulic fracture. Because a hydraulic fracture propagates perpendicular to the minimum principal stress, its diagnostics provide information about the direction of the minimum principal stress.

- World stress map

In the case that no information is available for the well or field, one may refer to the World Stress Map, which contains the compilation of stress orientations around the world (e.g., http://www.wsm.physik.uni-karlsruhe.de/). However, most of the data are from the analysis of deep seismicity, which occurs at much greater depths than typical oilfield wells (Economides, 2010).

- Geologic maps

Also, a geologic map of the field should be examined to see if major faults have been identified. In the vicinity of the faults, the principal stresses have most likely rotated to align themselves parallel to the fault surface (e.g., Barton and Zoback, 1994).

- Shear anisotropy

Because shear waves are polarized waves, they can detect variances in the elastic properties of material in the direction perpendicular to their travel path. When there are sufficient differences in the elastic properties, shear waves polarized in one direction will travel significantly faster than those polarized in the perpendicular direction (Pistre et al., 2009). If the rock formation contains a number of defects with a uniform distribution of orientation, the defects that are normal to σ_H are under more stress than those normal to σ_h. A shear wave traveling vertically and polarized parallel to σ_H will therefore travel faster than a shear wave polarized perpendicularly to σ_H (Economides, 2010).

A dipole sonic tool, when run through the wellbore, can measure the velocity of shear waves polarized in an orthogonal arrangement. From these data, the azimuth of the fastest shear wave can be extracted. In a near-vertical well, the azimuth corresponds to the direction of σ_H (Endo et al., 1996). An important consideration is whether the anisotropy measured from the slow and fast shear directions is induced by the stress contrast or the intrinsic properties of the medium. In a vertical well, most of the anisotropy is from stress effects and can easily be related to the direction of the far-field stresses (Endo et al., 1996). In horizontal or deviated wells, this is not necessarily true, and therefore the use of shear anisotropy to infer stress directions is not recommended in these situations. Processing

dipole sonic data for anisotropy analysis can come with difficulties; however, the fast shear azimuth computed from good-quality shear anisotropy data provides a robust estimate of the azimuth of the maximum horizontal stress σ_H in a vertical well (Donald et al., 2015).

C) Stress magnitude

- Determining the minimum principal stress

The least principal stress can be measured directly, using either extended leakoff tests or minifrac tests. These tests are similar to casing integrity tests or standard leakoff tests, except that the test procedure is slightly modified. Fluid is pumped into the wellbore to pressurize a short interval of exposed rock until the rock fractures and the fracture is propagated a short distance away from the well by continued pumping. In either case, pumping is carried out at a constant rate, and pressure and the volume of fluid pumped are recorded as a function of time (Gross and Seelig, 2006; Economides, 2010).

In order to minimize the energy required to propagate, a fracture created during the leakoff test will grow away from the well in an orientation that is perpendicular to the far-field least principal stress σ_3. Thus, the pressure required to propagate the fracture will be equal to or higher than the least principal stress. Fracture propagation will stop when leakoff of fluid from the fracture and wellbore into the formation occurs faster than the fluid is replaced by pumping. If pumping stops entirely, fluid leakoff will continue from the walls of the fracture until it closes, severing its connection to the wellbore. The fracture

will close as soon as the pressure drops below the stress acting normal to the fracture, which is the least principal stress.

- Determining the intermediate principal stress

The intermediate principal stress is always inferred from a relation that involves at least the minimum principal stress (Haimson and Huang, 1989; Ito and Hayashi, 1991; Guo et al., 1993). Obtaining a good estimate of the intermediate principal stress is difficult. It is mentioned only because it was once popular to use the breakdown pressure for the calculation (Hubbert and Willis, 1957). However, more recent work on the breakdown process (Detournay and Carbonell, 1994) shows that the breakdown pressure provides unreliable estimates and should not be used in the analysis of stresses.

- Determining the maximum principal stress

Once independent knowledge of σ_v and σ_h is available, σ_H can be determined from the widths of wellbore breakouts in vertical boreholes. Because the stress concentration around the well and the rock strength are equal at the point of the maximum breakout width, it is possible deduce σ_H by rearranging Eqs. 10(a-c) in terms of σ_H (will depend on borehole trajectory). Solving for σ_H, however, also requires a model for rock strength and knowledge of the pore pressure and mud weight. While the equations presented here are technically accurate only for elastic brittle rock, utilizing the results to select the appropriate mud weight for drilling future wells requires only that the same model be applied to predict wellbore stability as was used to determine the stresses.

Once breakouts have formed, they deepen but do not widen. Thus, the original width of the breakout is largely preserved, and calculations of stress magnitudes based on

breakout width do not have to be adjusted for changes in the wellbore shape associated with subsequent failure.

Furthermore, breakout width can be determined very accurately using acoustic or electrical image logs run after the well has been drilled (Moos et al., 2003). With the advent of resistivity, density, and porosity logging while drilling (LWD) tools that produce an image of the borehole wall behind the bit, it is now possible to determine breakout widths while drilling, which then makes it possible to determine σ_H in real time. On the other hand, in the absence of borehole image data, we can only place bounds on the width of presumed breakouts if they can be detected using the electrode pads of a dipmeter tool (pad width is typically about 30° in an 8.5-in. hole). Therefore, using mechanical calipers, it is possible only to place constraints on the magnitude of σ_H (Zoback et al., 2003).

Observations of well bore breakouts with an ultrasonic borehole televiewer show that regions around wellbores fail in a manner which is strongly controlled by the magnitude and orientation of the in-situ stress field. The study of breakouts in existing wells may prove to be an extremely important new source of data on the orientation of the in-situ stress field. A simple elastic failure model seems to confirm the hypothesis that the breakouts form as a compressive failure process, and the theory successfully predicts many of the general characteristics of the observed breakout shapes (Zoback et al., 1985). However, inelastic deformation around the wellbore is also significant in arresting breakout growth, and time-dependent failure processes are important in breakout evaluation. Both of these processes will have to be considered before breakout growth and development are fully understood.

D) Pore pressure

The only accurate way to determine pore pressure is by direct measurement. Such measurements are typically done in reservoirs at the same time fluid samples are taken with a wireline formation-testing tool. Recently, advances in while-drilling measurements make it possible to measure in-situ pore pressure while drilling (Zoback et al., 2003). However, it is difficult (if not impossible) to measure pore pressure in shales because of their very low permeability and small pore volume. In addition, because of their low permeability, pore pressure in shales adjacent to permeable reservoirs may be different from pore pressures in the reservoir. This pressure is often referred to as the "hydrostatic pressure." Several processes can cause the pore pressure to be different from hydrostatic pressure. The processes are identified in Section 2.6.

Pore pressure can be estimated using the Ratio Method, Eaton's Method, or Effective Stress Methods.

E) Stress regimes

An assessment of the stress regime establishes the expected cause for bed-to-bed stress variations through the formation and helps to identify a mathematical model for defining the stress profile. Five states of stress may be defined in terms of the principal stresses (Engelder, 1993). The simplest case consists of all three principal stresses being equal (i.e., lithostatic state of stress). This can occur in materials with little or no shear strength, such as poorly consolidated shales, or in materials that flow, such as salt. It may also be approached in extremely overpressured sediments. This state of stress is not widely

documented because stress is usually not measured in these materials. The second simplest case occurs in regions where the two horizontal stresses are equal and less than the vertical stress of the overburden. This regime may be expected in basins located in quiet, intraplate settings. For the remaining cases, the three principal stress magnitudes differ significantly. In-situ stress measurements and borehole image analysis concur to indicate that this is the most likely situation. Unequal horizontal stresses can be attributed to tectonic forces or effects that result from the presence of a geologic feature (e.g., a fold or fault).

Depending on the ordering of the stresses, three cases are defined: 1) A normal fault regime occurs when σ_v is the maximum principal stress, σ_1; 2) When σ_v is the minimum principal stress, σ_3, a thrust fault (or reverse fault) regime exists; and 3) If σ_v is the intermediate principal stress, σ_2, the fault regime is strike-slip. Stress measurements from around the world also indicate that pore pressure, lithology and the position of the layer within the structure (e.g., Whitehead et al., 1987; Thiercelin and Plumb, 1991; Aleksandrowski et al., 1992) are factors influencing variation of the stresses in sedimentary rocks. Typically, pore pressure changes induce stress changes that are greater than those associated with lithology, tectonic setting and structural or stratigraphic position. The stress regime is extremely important. Depending on the stress regime, identical lithologic structures can induce very different stress contrasts. For example, in a typical sand/shale sequence, the shales maintain higher stresses than the sandstones in a relaxed tectonic setting, whereas the sandstones have higher stresses than the shales in a compressive tectonic setting (Economides, 2010).

APPENDIX B - DATA MANAGEMENT

All work completed including data used, code written, papers published, presentations given, and sources used throughout the course of this study and any other studies during my master's program at Texas A&M University have been preserved using a data management plan (DMP) with the hopes and intention that other researchers may reproduce and expand on the work that I have started. The final versions of this thesis document are also located in this data repository. All the work was saved under their respective subfolders in the DM repository of Dr. Weijermars's research group, and a manual is provided therein with instruction on how to use the tools and models developed. The structure of my data management plan is shown below: